TÉCNICO LISBOA

Modeling of Artificial Muscles Made of Nylon Wire

Gabriel Madeira Fernandes da Silva

Thesis to obtain the Master of Science Degree in

Electrical and Computer Engineering

Supervisor: Prof. João Fernando Cardoso Silva Sequeira

Examination Committee

Chairperson: Prof. Pedro Manuel Urbano de Almeida Lima
Supervisor: Prof. João Fernando Cardoso Silva Sequeira
Member of the Committee: Prof. João Carlos Prata dos Reis

November 2020

Declaration

I declare that this document is an original work of my own authorship and that it fulfills all the requirements of the Code of Conduct and Good Practices of the Universidade de Lisboa.

Para os meus pais, Ana e João

To my parents, Ana and João

Acknowledgments

First of all, I would like to thank to my supervisor João Sequeira for showing great interest in the topic addressed in this dissertation since the day I presented it to him, but also for all the support and insightful suggestions. This dissertation would not be possible without all the knowledge and experiences acquired along the 5 years I spent in the University; for that reason I would like to thank to IST (both Taguspark and Alameda campus) and all the Professors who taught me, for playing a big role in my education. I should also thank to my Professors during the High School time, for playing a big part in this journey too, since without their push and valuable advice, I would not have followed the path that I ended up following. Special thanks also to Almodôvar Municipal Council for helping with my studies.

Last but not least, I would like to thank and dedicate this dissertation to my family, but also to my closest group of friends. Starting by my family, particularly my parents, Ana and João, I would like to thank them, for their patience, concern and support throughout the process and for always being available to fulfill my necessities related to this work (and during the last 5 years). Thank you for always wishing the best for me, and believing in me; I promise I will do the same. I must thank to my friends too, for always understanding the struggle that such work required from my side, and for forgiving one or other absence. Special thanks to Nelson for his encouraging words and constant motivation, and to Ana, for her help and advice about specific topics related to Biology, but also for her constant support. Thank you for your genuine concern and for being by my side along this journey (and also for putting up with me when I get grumpy).

Resumo

Músculos artificiais são uma área que pode combinar os campos biomecânico, biomédico e da robótica. Apesar do esforço para criar novas tecnologias ou melhorar as atuais, a maioria das propriedades dos músculos biológicos não são reproduzidas. Como consequência, as próteses não estão optimizadas: não são leves, naturais, nem confiáveis e são caras. Isto é um problema para amputados em países em desenvolvimento, principalmente crianças, às quais as próteses deixam de servir.

Recentemente, um trabalho produziu atuadores de supercoiled polymer com fio de pesca, os quais revelaram propriedades interessantes para fabricar músculos artificiais e aplicar em próteses. O presente trabalho estudou estratégias para melhorar a contração e expansão destes atuadores, e construiu uma associação agonista e antagonista, com a solução encontrada. Modelação em caixa cinzenta, baseada no modelo linear da massa-mola-amortecedor e na lei do arrefecimento de Newton, foi testada para caracterizar a associação, juntamente com um controlador PID para o ângulo.

Os resultados dos atuadores individuais foram semelhantes a outros trabalhos e evidenciaram semelhanças com as propriedades dos músculos biológicos. A validação e verificação do modelo e esquema de controlo foram efetuadas por simulações e testes na associação. Os resultados podem ser melhorados explorando caminhos diferentes, mas no geral foram satisfatórios e de acordo com o esperado. A construção de atuadores foi igualmente sistematizada.

Palavras-chave: músculos artificiais, atuadores de supercoiled polymer, associação agonista e antagonista, modelação em caixa cinzenta, desenho de sistema de controlo, controlo de ângulo.

Abstract

Artificial muscles are an area where the bio-mechanical and bio-medical fields can merge their expertise with robotics. However, despite the effort to create new technologies or improve the existing ones, the majority of biological muscles' properties are hard to duplicate. Therefore, prosthetic devices lack optimization in weight, reliability and do not feel natural and are expensive. This is a problem for amputees in developing countries, notably children, who quickly outgrow their prostheses.

Recently, a work produced supercoiled polymer actuators with fishing line, which revealed attractive properties to manufacture artificial muscles to apply in prostheses. The present work studied strategies to improve the contraction and expansion of these actuators, and built an agonist and antagonist association, with the selected solution. Grey-box modeling, based on the linear mass-spring-damper model and on the Newton's law of cooling, covered the association dynamics, together with a PID controller for the angle.

Single actuators' results were in line with other works findings and revealed some degree of similarity to biological muscles' properties. Simulations and tests upon the association validated and verified the model and control scheme. It is possible to improve the results and explore new paths; still, they were satisfactory and in accordance with the expected behavior. The work also described the actuators' manufacturing process.

Keywords: artificial muscles, supercoiled polymer actuators, agonist and antagonist association, grey-box modeling, control system design, angle control.

Contents

List of Tables

List of Figures

Nomenclature

Greek symbols

α	Temperature coefficient of resistance
β	Damping coefficient
$\Delta t, \Delta T$	Temperature variation
η	Mechanical efficiency
λ	Absolute thermal conductivity
θ, Θ	Angular displacement

Roman symbols

$\ddot{X}$	Acceleration
$\dot{X}$	Velocity
$\mathcal{F}$	Applied force
$\mathcal{T}$	Torque
A_b	Area of the cylinder's base
C	Thermal constant
C_{th}	Thermal mass
CL_{AAA}	AAA closed-loop transfer function
$clamp$	Condition that turns the integral off or not
$Ctrl$	Controller transfer function of the AAA
E	Energy
e, E	Error between the output and reference
I	Electric current
J	Moment of inertia
K	Controller gain
k	Stiffness
m	Mass
N	Filter coefficient
OL_{AAA}	AAA open-loop transfer function
P	Electric power
P_{Lost}	Thermal power generated in the MOSFET
$Plant$	Actuator's plant transfer function
R	Electric resistance
r	Radius
$R_{\theta JA}$	MOSFET thermal resistance
$R_{DS(on)}$	MOSFET static drain-source resistance
s	Frequency domain
T	Tension force
t	Time
T_s	Sampling period
T_{amb}	Ambient temperature
T_{Total}	MOSFET maximum temperature
u	Saturation block output
u_c, U_c	Controller command
v^2, V^2	Squared input voltage
$V_{actuator}$	Volume of the actuator
W	Work
x, X	Linear displacement

Subscripts

0	Reference condition index
$1, 2, p$	Agonist/ antagonist/ pulley indexes
i, n	Computational indexes
in, out	Supplied to, or by the system indexes
p, i, d	proportional/ integral/ derivative indexes

Glossary

AAA Agonist and antagonist association, is the structure built to demonstrate the investigation results, regarding the contraction/expansion problem.

AW Anti-windup, are methods applied to keep the PID's integrated value from increasing past a limit.

DAQ Data acquisition system, are devices that interface between a signal and a computer, usually employed to convert analog signals (from sensors) to digital values for computer processing tasks.

DOF Degree of freedom, are the sum of independent and possible movements (i.e., number of joints).

FD Filtered derivative, corresponds to a first order low pass filter in series with the derivative term of the PID controller that is responsible for attenuating the high frequency noise.

MAE Mean-absolute-error, is an index like RMSE, but does not use the root of average squared errors.

NRMSE Normalized-root-mean-square-error, is a model's performance metric based on the RMSE.

PCB Printed circuit board, is a thin board, made of a non-conductive substrate, that supports and connects different components through conductive tracks etched or printed in the board.

PID Proportional-integral-derivative controller, corresponds to a control feedback method that uses the present, past and the prediction of the future error to compute the appropriate actuator commands.

PWM Pulse width modulation, is a method to control the power delivered by an electrical digital signal, by modulating the pulse width of a rectangular wave.

RMSE Root-mean-square-error, is a model's performance indicator, computed by measuring the difference between the predicted values by the model and the actual values.

SCP Supercoiled Polymer, is the name that usually classifies the actuators produced by polymers (like nylon) that output a linear action, due to their visible coils.

TE Thermoelectric, is the model that describes how voltage potentials relate to temperature changes in the actuator, based on both the Newton's law of cooling and electric power equations.

TM Thermomechanical, is a model that defines how temperature affects the actuator's mechanical properties (displacement), based on the linear mass-spring-damper model, with an extra coefficient.

Chapter 1

Introduction

This chapter describes the motivation and objectives of the present dissertation. It also presents the topics studied along the current dissertation and each chapter's content.

1.1 Motivation

Studying biological muscles is an attractive area, since it is possible to replicate their properties to apply in future projects, like their intermittent displacement, adaptable stiffness and force control, high life cycle enabled by regenerative mechanisms, and their motion-oriented design [1].

Electric motors, pneumatic and hydraulic actuators perform motion-related tasks in a wide range of robotic systems. Artificial muscles' goal is to generate movement too, however, using the previous actuators is not ideal to replicate the natural muscles' behavior. Despite interesting results in different artificial muscles technologies, a widely adopted technology is yet to come, according to the authors of [2]. Nevertheless, the work in [3] presented a promising technology that uses a new method to produce artificial muscles, based on standard fishing line, that displays several attractive properties. This work introduces and produces SCP (Supercoiled Polymer) actuators. Subsequent works also refer to these actuators as Twisted and Coiled Polymer Actuators (TCPA), Coiled Polymer Actuators (CPA) or Twisted and Coiled Actuators (TCA).

The low cost $\approx \$5kg^{-1}$ [4] and weight, strain level, flexibility, silent motion, unbounded action environment and small hysteresis compared with other actuators [5] sustain the SCP actuators' potential. Plus, some studies also tested their self-healing properties: a composite made of fishing line was able to heal damage efficiently [6]. Since there is a degree of resemblance between biological muscles and polymers [7], together with the properties above, it is plausible to assume that these actuators are suitable to produce artificial muscles. Bio-mechanical and bio-medical fields could benefit from this, with the creation of reliable, lighter, more natural and cheaper prostheses. This would increase the access of amputees in developing countries [8] and help children who are still growing, since their prostheses quickly become outdated and impossible to wear [9], demanding a constant replacement, sometimes neglected due to the costs.

1.2 Topic Overview

Artificial muscles need external stimulation, either by voltage, electric current, temperature, light or pressure, to generate movements. The underlying concepts are easy to grasp, but there is no technology that can mimic closely the behavior and main features of natural muscles, yet. Possible reasons for that, as far as the author could understand, might be the lack of known materials with the desired properties, or investigations aimed to the end goal - producing movement - instead of the development and test of new concepts. There are effective ways to generate controllable movement, but if the goal is to develop artificial muscles to integrate, seamlessly, in the human body, new options require investigation, or the ones in use need review. As one will see in chapter 2, there are promising solutions, but investigation is a must to develop more reliable, efficient and practical artificial muscles.

1.3 Objectives

The interest towards SCP actuators has grown gradually; however, there are matters that need more explicit explanations. Thus, one of the goals of the dissertation is to provide detailed explanations along the manufacturing steps, together with all the required parameters, to ease and systematize the production of future SCP actuators. Besides that, trying new configurations - different associations between actuators with different techniques - will also be a must. The goal is to extract new features and explore new applications and feasible motions. The dissertation will also study modeling strategies to characterize the SCP actuators, with respect to different parameters, to better understand their behavior and hence control them with a suitable strategy.

The work will also analyze suitable cooling techniques, to increase the expansion speed, and solutions to achieve quicker expansion/contraction motions, with different actuators' associations. As mentioned, there are benefits from applying these actuators as artificial muscles in prostheses. So, developing a demonstration project able to showcase their applicability and potential in prosthetic devices is also worth trying. Finally, another important goal is the employment of the methods and results obtained as a basis for future works on the same topic.

1.4 Contributions

This dissertation contributes to the current state of the art in artificial muscles research, especially to the muscles produced via nylon fibers (SCP actuators), in the following topics:

- Manufacturing process systematization. Detailed description of each step, and supply of all the parameters to manufacture functional single actuators that are less prone to fail.

- Model to describe an agonist and antagonist behavior. Implementation and adaptation of Yip and Niemeyer's proposed models [2, 10] to describe the AAA's new dynamics.

- Tests to assess the raw material of the actuators. Assessment of single actuators' durability (regarding the heat and weight) and elasticity performance, to study their limiting conditions.
- Display of a method to build an AAA with SCP actuators. The structure works as a pair of biological muscles and can include improvements; still, it is a possible benchmark for future solutions.
- Overview about different references' results. Comparison between the obtained results, whenever it is possible, with the literature's findings, which contributes to better understand and characterize different SCP actuators behaviors, based on their specifications.

1.5 Thesis Outline

The present dissertation has five chapters, being the first, the current introduction. The structure of the remaining chapters is as follows: literature review, methods, results and discussion, and conclusion.

The second chapter reviews the state of the art about artificial muscles. It introduces biological muscles and four artificial muscles types, but it prioritizes the adopted one. So, it gathers information from other works to cover the following topics about the focused type: manufacturing techniques; modeling and control strategies; methods to improve the contraction/expansion motion; and common applications.

The third chapter discusses the methods adopted along the dissertation, to execute all of its stages. It has four sections: the first describes the manufacturing steps; the second explores the identified solutions to enhance the contraction/expansion motion; the third introduces the proposed modeling strategy and the procedures to identify it; and the fourth deals with the employed control strategy.

The fourth chapter presents and discusses the results obtained for single SCP actuators and for the AAA, through experiments and simulations. It has five sections, and compares the results gathered from other works with this dissertation's own findings. It studies the actuators' material properties (durability and elasticity); tests the selected solutions to the contraction/expansion problem (to identify the best one) and discusses the engineered AAA. The third section validates the model and estimates its parameters; the fourth covers the underlying matters regarding the adopted control strategy, namely the verification and stability; and the fifth section sums up part of the collected data and findings.

The fifth chapter reviews the work done and assesses if the findings along the work fulfilled the objectives set. It contains suggestions for future improvements to include in the developed work, and expresses the author's perspective about the topic.

Chapter 2

State of the art: Artificial muscles

This chapter provides an overview about artificial muscles, focusing on the following: biological muscles, types of actuators used as artificial muscles, SCP actuators' manufacturing process, modeling and control methods, contraction/expansion options - for the SCP actuators - and overall applications.

2.1 Biological muscles

To study artificial muscles one must learn and understand concepts related to human muscles, firstly. This analysis followed the books by Seeley et al. and Muscolino (mainly the chapters about muscles).

The muscles composition is of contractile cells; and they comprise three types: skeletal, smooth and cardiac muscles. Skeletal muscles connect to the bones by tendons and they are responsible for the main movements of the body. They entail voluntary movement, but the nervous system may also induce involuntary contractions. The cardiac muscle is the heart's main tissue; the smooth muscles form the walls of hollow organs (except the heart) and also occur in the skin and eyes. Both of them respond to involuntary control. This work, will attempt to reproduce the main properties of skeletal muscles via SCP actuators. Maintaining the body's posture and breathing are some of the skeletal muscles' tasks. Moreover, they keep the body temperature (by the resulting heat from contractions) and enable social activities (talking, gestures, facial expressions, etc.) [11].

Muscles have four functional characteristics: contractility (capacity of contraction and producing an associated force), excitability (capability of reacting to stimuli from the nervous system), extensibility (capacity of stretching while contracting) and elasticity (ability to resume to the initial shape after stretching). The skeletal muscles can contract voluntarily, but they can only extend passively, through the action of gravity, contraction of an antagonist muscle or pressure of a liquid inside a hollow organ, or vessel. The muscle that creates the action while contracting is the agonist and the muscle that works in the opposite direction is the antagonist [11]. A functional group of agonist muscles only recruits the necessary muscles to execute the action. During the agonist contraction, the antagonist muscle extends and it can store a passive tension force. If the agonist relaxes and the antagonist contracts, the stored force will increase its active contraction force. Besides these two kinds of skeletal muscles, there are others with

associated functions too, such as supporting parts of the body to hold its position [12].

Muscular contraction is the shortening of a muscle as a result of a stimulus that creates an action potential (electrochemical phenomenon) in one or more muscle fibers. It is a force (tension) and it can take one second to occur [11]. A single muscle's contraction force depends on the number of recruited motor units (group of a neuron and all the muscular fibers with which performs synapses). The contraction's strength increases with the increasing number of stimulated motor units. Thus, it is possible to deliver the proper amount of force according to each situation. Muscle contractions follow the all-or-none law: each muscular fiber fully contracts (100 % contraction) whenever the nervous system sends a contraction type message, but if it does not send a message, the fibers relax (0 % contraction) [12]. There are several types of contractions: isometric (muscle's tension changes but its length is constant), isotonic (muscle's length changes during contraction but not its tension), concentric (muscle's tension increases gradually while its length shortens), eccentric (muscle's tension decreases gradually while its length increases), asynchronous (contractions performed by motor units that originate soft and uniform muscular contractions) and muscle tonus (maintenance of a uniform tension for large periods of time) [11]. Concentric contractions relate to agonist muscles and eccentric to antagonist muscles, whereas isometric (associated to the posture muscles) to none of those [12]; isotonic contractions originate upper limb and finger movements (usual body regions to wear prosthetic devices). Finally, it is important to stress that the muscle's shape and length have a strict relation with the ability that they have to contract and generate force [11].

2.2 Actuators review

This section will present some actuators' technologies that are possible to apply to artificial muscles and their working principles. Once there is a considerable number of actuators, the focus was on those the literature revealed as more suitable to apply in artificial muscles.

The prosthetic field can benefit from artificial muscles; the authors in [7] proposed several actuator technologies to implement in orthotic and prosthetic devices to behave closer to biological muscles (in terms of weight, shape, feel and noise), than the traditional electromagnetic motors. In addition, the works [1, 4] provided a review about actuators, their working mechanisms, properties and limitations. Next, a brief description presents the working principles of the considered solutions, taking as references the previous works.

2.2.1 Thermally activated shape-memory alloys (SMAs)

SMAs are materials that can recover its original shape when excited with a stimulus, such as heat. This means that after bending or twisting, a SMA can return to the original form. The most popular alloy that shares this property is the nickel-titanium (NiTi) one (also known as nitinol). Transformations between two phases, martensite and austenite, which exhibit three crystal structures (twinned martensite, detwinned martensite and austenite) are the processes behind the working principle of SMAs. Exciting

the material through heat initiates the transformation from martensite to austenite; whereas during cooling, the transformation occurs from austenite to martensite [4]. In general, the shape memory effect in NiTi alloys occurs when applying an external stress, according to [1]: it is possible to easily deform the twinned martensite structure; so, when heated, it returns to a well-defined form (austenitic phase). Table 2.1 gathers results for the SMAs.

2.2.2 Pneumatic actuators

Pneumatic actuators take advantage of the pressurization of a fluid in an expandable chamber to produce movement. The chamber can be a piston-cylinder device or elastically deformable. There are different solutions for pneumatic artificial muscles that use the second chamber type, but the most common uses braided muscles. Pneumatic artificial muscles (PAMs) that fall in the braided muscles category, also known as McKibben muscles [4], include a hollow elastic cylindrical chamber (bladder) enclosed by a braided sleeve. Fibers of non-stretchable material form this sleeve. When pressurizing the bladder, it expands in volume, as a result of the confinement created by the sleeve, which results in a linear actuation by the muscle [13]. Depending on the initial geometry of the braid fibers, one can achieve different actuation motions. Further on, Table 2.1 lists some properties about pneumatic actuators.

2.2.3 Stimuli-responsive gels

These actuators' main features are due to the smart hydrogels' inner structure properties - they can swell or shrink the water as a consequence of a stimulus (temperature, pH, light, electric field, specific chemicals, etc.) [4].

The principle behind temperature-responsive hydrogels is the interaction between hydrophobic and hydrophilic segments, in the polymer's chain, and water [4]. Hydrogels with a lower critical solution temperature (LCST) form a gel (shrink) upon increasing temperature, and return to solution state (swell) after lowering the temperature below LCST. The hydrogels with an upper critical solution temperature (UCST) work in the opposite way - the gel forms below UCST (shrink) and becomes soluble above it (swell) [14]. In the pH-responsive hydrogels, a variation of pH changes the properties of the gel's structure due to balance fluctuations of hydrophobic/hydrophilic polymer chains. In the light-responsive hydrogels, the light excitation changes the polymeric network properties (elasticity, swelling degree, viscosity, etc.); and in the electro-responsive hydrogels, the excitation with an electric field give rise to migration of mobile ions, which can deform the structure [4]. Table 2.1 lists these actuators main properties.

2.2.4 Highly oriented semi-crystalline polymer fibers

This category of actuators includes the previously introduced SCP actuators, which are the main focus of this dissertation. Therefore, this subsection provides a more detailed review about them.

Classification

The literature mentions at least three ways of classifying this kind of actuators, by means of the produced action: there are the linear, torsional and bending actuators. Among the linear, there are two subcategories: the auto coiled and the mandrel coiled actuators. In the auto coiled type, the filament twists until the moment the fiber coils completely onto itself. Thus, the original polymer fiber becomes a helical-type spring (Figure 2.1 (a)). To prevent the coils from untwisting it is necessary to stabilize them by heat (thermal annealing) as 3.1 will describe [15, 16]. The second type, obtained by means of mandrel coiling, is similar to the first one, but the fiber only twists until the formation of coils. Then, uses a rod (mandrel) of a certain diameter to wrap the resulting fiber around, followed by a thermal annealing process to stabilize the coils. The end result is similar to the auto coiled actuator, but the helical spring has a larger diameter (Figure 2.1 (b)). Besides that, mandrel coiled actuators exhibit larger contractions, but tend to produce less force than the first type [3, 15, 16]. Supercoiled polymer (SCP) actuators is the name of these two actuators due to their visible coils.

Non-coiled twisted fibers can produce torsional actuators. Experiments showed that these actuators were able to contract by rotating, if heated [3]. The actuator has a torsionally active and non-coiled fiber in series with a second fiber (spandex, for example), as depicted in Figure 2.1 (c). The contraction occurs when coils appear in the second fiber due to the rotation induced at the junction, caused by heating the active fiber [17]. The actuators can also show multidirectional action [4]. This is due to a property that some polymer fibers have, where they can shrink in length but expand in diameter. Modifying the cross-section shape and then selectively heating the fiber at one side, can lead to a bending motion (Figure 2.1 (d)) and even to more complex motions, as well. Electric resistance heating, chemical reactions or lasers are among the options for the heating process [18].

It is also possible to classify the actuators according to their chirality, i.e., the fiber's twist direction in relation to the direction of coiling: there are the homochiral and the heterochiral SCP actuators. A homochiral SCP actuator has the same direction in both twist and coiling, whereas the heterochiral actuators have the opposite direction [3]. This leads to different working actions: homochiral actuators will contract if heated (Figure 2.1 (e)) and both auto coiling and mandrel coiling processes can manufacture them; heterochiral actuators will expand if heated (Figure 2.1 (f)), but only a mandrel coiling process can produce them [15].

SCP actuators' filament types

There are two types of filament to produce SCP actuators: mono-filament fibers - standard nylon fibers, for example fishing line - and multi-filament fibers - conductive-coated nylon sewing threads, for example silver-coated nylon. The actuators produced with conductive nylon threads reveal lower performance (lower strain) than the ones produced with mono-filament nylon [2, 15, 16]. Other difference is that multi-filament fibers allow direct Joule heating actuation through an electric current. On the other hand, mono-filament fibers are cheaper and have a bigger lifetime [16], but they need a resistive wire (nichrome or copper, for example) wound around them for the Joule heating process. To prevent the

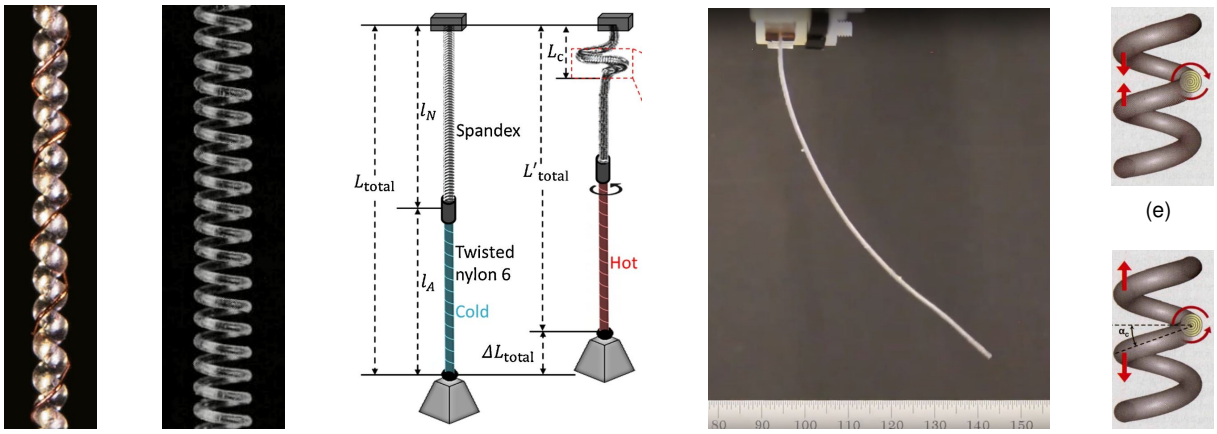

Figure 2.1: Actuators made of polymer fibers. (a) Auto coiled SCP actuator, made with nylon monofilament fiber and enameled copper wire wound around it. (Adapted from [19]), (b) Mandrel coiled SCP actuator. (Adapted from [3]), (c) Torsional actuator. (Adapted from [17]), (d) Bending actuator. (Obtained from a supplementary video in [18]), (e) Homochiral actuator, (f) Heterochiral actuator. (Both adapted from [3]).

resistive wire of affecting the actuator's contraction, one should wrap the wire around with opposite chirality to the coils of the actuator (Figure 2.1 (a)), as done in [19]. Other option is to use a heat gun to heat the actuators, but it is undesirable if the goal is to create artificial muscles.

Working mechanism

The actuators' working mechanism is due to the twisting action during fabrication. The fiber's polymer chains acquire a microscopic helical shape during the twisting process. If heated, thermal expansion will occur and the volume will increase, but the chains will maintain, nearly, their initial length. This means that the helices will have to grow in diameter and, as a result, will untwist. Coiled threads exhibit a second and macroscopic helical shape called supercoil, and contract along the primary coil axis, under thermal heating, because of the expansion (Figures 2.1 (e) and (f)) [2]. This means that untwisted nylon expands in the radial direction and contracts along the axial direction, if heated, according to [20].

2.2.5 Summary

Table 2.1 compares the actuators' technologies studied above and gathers some of their main features. The table shows the most recent data collected from the accessed literature.

There are other promising actuators' technologies mentioned in the consulted literature, besides the ones presented. However, all reveal drawbacks, such as the cost, need for high voltages and electric fields, low efficiency and need of encapsulation, which make them less appropriate to apply in artificial muscles. The authors of [21] divided in five groups different actuators, and evaluated each one's performance with eight categories. The goal was to achieve a systematic approach to choose the actuator that better fitted one application, assuming that all the categories had the same weight. As pointed out by the authors, unsuited criteria and weights can lead to misleading results. Still, it was a fair way to

assess potential applications and conclude about some actuators' limitations. As an alternative, one can include more actuators and focus more on each one, instead of groups.

Table 2.1: Comparison between natural muscles and candidate technologies to produce artificial muscles. (Adapted from [7], [4], and [1]).

Biological muscle/ Actuator	**Typical (Max.) strain (%)**[a]	**Typical (Max.) stress (MPa)**[b]	**Typical (Max.) work density**[c]	**Cycle life (Nr. of cycles)**[d]	**Relative speed (full cycle)**	**Limitations**
Mammalian skeletal muscles	20 (>40) [1, 4]	0.1 (0.35) [1, 4]	8 kJ.m^{-3} (<40 kJ.m^{-3}) [1, 4]	>10^9 [1, 4]	Medium [7]	Narrow temperature range; Difficult to produce; [1]
Thermally activated shape-memory alloys	5 (8) [1]	<700 [4]	1000 kJ.m^{-3} (10 000 kJ.m^{-3}) [1, 4]	300 (@ 5 % strain) 10^7 (@ 0.5 % strain) [1, 4]	Slow [7]	High currents and hysteresis; Low efficiency/cycle of life; [1]
Pneumatic actuators	15 [4]	6 N (3.4 MPa normalized to the diameter) [4]	500 kJ.m^{-3} [4]	30 000 tested 100 000 expected [4]	Depends on the fluid's flow rate	Portability (fluid tanks); Fuel replenishment [4]
Stimuli- -responsive gels	(90) [4]	(4) [4]	(460 kJ.m^{-3}) [4]	"Performance degradation over time" [4]	Slow [4]	Slow response; Chemical stability; [4]
Highly oriented semi-crystalline polymer fibers[e]	4 (33) (@ 15 MPa) [4]	22 (@ 10 %) [4]	2.48 kJ.kg^{-1} (@ 84 MPa) [4]	1.20$\times 10^6$ (@ 10 %) [4]	Slow [4]	Low efficiency; Slow heat transfer rate; Small bandwidth; [4]

[a] Strain: displacement upon excitation normalized to the initial length. [b] Stress: applied force normalized to the initial cross sectional area of the actuator. [c] Work density: output work generated in one actuator cycle normalized to the volume or mass of the actuator. [d] Cycle life: number of cycles that the actuator can undergo before failure. [e] Linear actuator made of Nylon-6,6.

2.3 SCP actuators manufacturing

Subsection 2.2.4 mentioned the fabrication of SCP actuators in order to classify them based on their manufacturing differences. This section discusses, in detail, the manufacturing process of linear SCP actuators (the adopted type).

2.3.1 Twisting and coiling

As mentioned before, the linear actuators include auto coiled and mandrel coiled actuators. Auto coiled actuators entail twisting until the moment the fiber coils completely onto itself, whereas mandrel coiled actuators comprise twisting until the formation of coils and the use of a rod. It is common to use DC motors or drills to twist the fibers. To initiate the twisting process, it is necessary to create tension along the fiber, by hanging a weight in one end, while the other end ties to the rotating device. The weight needs to be appropriate to the fiber's characteristics (diameter): if it is too low, the line will tangle, and if it is too heavy it will break. If the weight is suitable, tightly wound coils will begin to form, since the end of the fiber with the weight does not twist together with the motor. The systematic way to choose the weight is to progressively increase the weight until finding the one that does not tangle the fiber [22].

The resulting coils will contact with each other, which reduces the contraction of the actuator. However, it is possible to slack the contact between them, by untwisting the actuator, or increasing the applied weight, according to [3]. The spring index is the ratio between mean coil diameter and the fiber diameter [3]. This parameter relates inversely with the actuator's stiffness: using a heavier weight during the coiling process will result in a lower spring index (stiffer actuator). This means, as expected, that parameters such as the strain and load-carrying capabilities of the actuator, are possible to modify with

a spring index adjustment [3]. Additionally, the coiling speed also reveals an impact in the final actuator, since studies verified that decreasing the rotational speed, increased the strain and work done for multi-filament fibers [15].

2.3.2 Annealing and training

These two procedures are extremely important to set the actuators' properties that will make them reliable to act as muscles. The main goal of the annealing stage is to set the polymers' structure and prevent the coils from untwisting. From Table 2.2, one can see several options to conduct the annealing process. For example, the work [16] executed the annealing stage via warm air (temperature near the polymer's melting point) using an oven, without any weight hung on the actuator, whereas [15] used a weight and applied a heat treatment based on the Joule heating effect. Still, both cases set the polymers' structure. Plus, it is also common to frame the coiled actuator during the annealing stage to avoid untwisting, by tieing the two fiber's ends [23]. The coiled fiber should also be under a certain amount of tension, with a fixed length, to prevent inter-coil contact during the process, according to [24]. On the other hand, it is also viable to ply an actuator onto itself (Figure 2.2) because it also prevents the coils from untwisting, as explained initially in [3].

(a) (b)

Figure 2.2: Two-ply actuator represented in (b) obtained from (a) (Adapted from [3]).

The training's goal is to achieve convergence, with respect to the actuator's resting length, through a stimulus, i.e. obtaining a fully reversible actuation response [2]. When heating an actuator, while hanging a load, it elongates because of the high temperatures and weight. Therefore, exciting progressively the actuator, alternating with periods of no excitation (multiple heat/cool cycles, known as training cycles), will make it contract/expand between its initial resting length position and a new elongated length position. Performing this repeatedly will eventually result in a convergence point, regarding the length, which will lead to a repeatable and reversible action, whenever the process resumes [2, 10]. Still, it is important to highlight that [25] concluded that the annealing at 200 $^{\circ}$C showed complete reversibility in the first cycle, without requiring any additional training (extra cycles) for torsional actuators. As shown in Table 2.2, there are different methods and specs to train the actuators. It can be a hydrothermal process (immersing the actuators under water) [24], warm air (using a heat gun) [23], but also via an electrothermal process (Joule heating) [2]. In the last approach, using mono-filament or multi-filament fibers, will introduce differences. A mono-filament fiber requires a conductive resistive wire wound around the actuator (silver painting the coils is valid too [15], but it is less common); whereas using a multi-filament fiber enables electric current direct application to the actuator. Table 2.2 gathers some manufacturing parameters of other works.

Table 2.2: Different SCP actuators' manufacturing methods available in the literature, and its parameters.

Fiber type	Fiber diameter (mm)	Resistive wire (diameter - length)	Revolutions per minute	Coiling weight - training weight	Annealing environment	Annealing specs	Training environment	Training specs
Nylon 6 mono-filament [15]	0.77	Nichrome (36 gauge/0.127 mm - 22.0 cm)	200	610 g (5.98 N) - 610 g (5.98 N)[a]	Joule heating (electrothermally)	0.24 A	Joule heating (electrothermally)	60 s heat 60 s cool (10x)
Nylon 6 mono-filament [16]	0.50/ 0.80	Copper (0.14 mm - NA)	NA	Not applicable	Oven (warm air)	$\sim$ 180 °C 30 min	Joule heating (electrothermally)	12 V
Silver-coated nylon 6,6 multi-filament [2]	0.38	Not applicable	"Low RPMs"	50 g (0.49 N) - 100 g (0.98 N)	Two-ply configuration[b]	Not applicable	Joule heating (electrothermally)	1.50 V/cm Square wave 1 s on 9 s off
Nylon 6 mono-filament [23]	0.34	Copper (0.10 mm - 50.0 cm)	NA	139 g (1.36 N) - 280 g (2.74 N)	Heat gun (warm air)	$>$150 °C 30 min	Heat gun (warm air)	$>$150 °C 30 min cooling to room temperature (3x)
Silver-coated nylon 6,6 multi-filament [8]	NA	Not applicable	1200	NA - 150 g (1.47 N) to 350 g (3.43 N)[c]	Two-ply configuration[b]	Not applicable	Joule heating (electrothermally)	0.50 A and cooling (repeated until reach consistent length)
Nylon 6 mono-filament [24]	0.86	Not applicable	NA	900 g (8.82 N) - 200 g (1.96 N)	Oven (warm air)	180 °C 2 h	Water (hydrothermally)	Hot water (99 °C) $\sim$ 5.5 s and cold water (21 °C) $\sim$ 8 s (5x)
Silver-coated nylon 6,6 multi-filament [26]	0.20	Not applicable	800	175 g (1.72 N) - 400 g (3.92 N)	Two-ply configuration[b]	Not applicable	Joule heating (electrothermally)	0,60 A 50 s "voltage varies with length" (8x)

NA stands for "not available", meaning that in the corresponding referenced work the authors did not provide the values. [a] Annealing and training stages performed together, using the same weight. [b] Ply an actuator prevents untwisting. [c] The training process used weights within this range.

2.4 SCP actuators modeling and control

This section will study the modeling techniques that suit the chosen actuators, together with control strategies and their pros and cons. Therefore, it will briefly overview the approaches presented in the literature, so one can turn functional SCP actuators into reliable artificial muscles.

2.4.1 Modeling strategies

The work [27] captured the behavior of an SCP actuator based on a spring model; it determined experimentally the parameters related to the displacement, temperature and velocity and integrated them in the model. The authors of [28] modeled a single SCP muscle (developed to apply in a wrist orthosis) based on a spring and damper model, as well, with an extra linear temperature dependent term. They obtained a transfer function, relating the power input to the force, whose parameters estimation was through applying a variety of voltages to the actuator and measuring the force. Thermomechanical and thermoelectric models to test the controllability in both force and position of the actuators are solutions in [2, 10]. These works, linearized the hysteresis between strain and force with a mass-spring-damper model in the thermomechanical analysis, and measured the temperature indirectly through force in the thermoelectrical model. Direct and indirect measurements, via relations among the acquired data, helped obtaining the models' parameters. Unlike previous works, [20] applied a linear model to predict the performance of three distinct types of bundled SCP actuators. The model derivation was from individual SCP actuators and included both thermoelectrical dynamics and thermomechanical properties in the form of a spring-damper system, once again. A linear least-squares regression identified the models' parameters.

Apart from that, [29] obtained a nonlinear equation that estimated the displacement as a function of electric current and load. The thermoelectrical model accounted the heat transfer and the change in electrical resistance, due to the heat; and the thermomechanical model considered the temperature effect on the displacement and the geometry of the muscle. In [30] a macroscopic nonlinear model that incorporated both temperature and displacement models is in place. This approach divided the inverse dynamics of the temperature model into a nonlinear transformation part and into a linear transfer function, whereas the inverse static model of displacement employed only a nonlinear transformation. The same authors also suggested a general nonlinear dynamics model for SCP actuators in [31]. This model included a nonlinear model of the temperature, based on the energy balance of the actuator, and a nonlinear model of the displacement, based on Lagrange's equation of motion. The last two works identified the model parameters using nonlinear least square methods.

Other techniques included approaches such as grey-box modeling (models combining a partial theoretical structure with data). Although there were not many works describing modeling techniques applied to antagonistic structures, [32] applied system identification to a configuration of actuators of this kind. The authors considered a linear system model and employed grey-box modeling, which comprised two sub-systems in series. One sub-system expressed the dynamics from the input voltage to the force (force model) and the other, from the force to the displacement (mechanical model). In [5, 33], the same authors applied, once again, grey-box modeling based on the LTI model with reference to the work developed in [2], but now for a regular SCP actuator configuration. The authors' following work presented a more robust control system, and comprised a black-box methodology (which assumes no model form) [34]. The work done in [35] also used black-box system identification to find the order of the actuator. It modeled SCP muscles following a discrete-time state space approach, and employed a prediction error method to estimate the parameters of the model. Apart from that, the work in [26] was able to model the angular position of three joints of one finger (of an orthotic hand) using the Euler-Lagrangian approach for robotic manipulators.

2.4.2 Control strategies

In [36] the method to control the position of a SCP actuator measured the temperature through the nickel wire, wound around it, since the electrical resistance varies linearly with temperature. After calibrating the relation between the temperature and the nickel's resistance, the work suggested a simple closed-loop temperature control, and a semi-closed loop position control, both with PID controllers. Later on, the work also proposed a full-closed loop control system with two PID controllers. These strategies relied on transfer functions from electric power to temperature and from temperature to displacement. The work [19] explored a similar method, but used a circuit switching between power supply and resistance measurement. This enabled almost instantaneous resistance readings. Thus, the authors suggested a closed-loop temperature control, feeding the resistance measurements (i.e. temperature) into a simple PID controller, and later, a nested controller, with position and temperature feedback. In contrast, the work presented in [27] used a microthermistor in the SCP actuator to acquire the tempera-

ture. It displayed a closed-loop temperature control, but used a proportional-differential control instead. Again, a closed-loop PID controller was a solution in place, but for the SCP actuator's force, to apply to a wrist orthosis [28].

Other control strategies use feedforward controllers and feedback control laws, simultaneously. Initially, [2, 10] applied open-loop control, using a lead compensator, and a closed-loop control strategy, with a feedforward design, to increase the accuracy and speed of the force tracking control. Later, to execute position control, implemented a closed-loop controller with PD and feedforward controllers. The work developed in [33] employed a method called internal model control, which was based on the identified model and consisted of feedforward and feedback controllers. Also, in [32], the same authors, implemented feedforward and feedback controllers (namely, a PID controller), but the target was an antagonistic structure.

Apart from the aforementioned strategies, there are works that exhibit relatively different approaches. For example, the work done in [37] applied an iterative learning control method to perform trajectory tracking with an 1 DOF manipulator with opposing SCP actuators. Iterative learning control is robust, even without using any accurate dynamic model. Feedback control with a PI controller and an anti-windup compensator, which helped tackling the effects caused by the windup phenomena, like overshoot, slow settling times and instability, is also a viable method [5]. As a follow-up from this work, in [34], the authors investigated a solution involving external disturbances not accounted in [5]. They obtained a more robust control system, using a disturbance observer, as a result. Meanwhile, [30] proposed a feedforward controller with the Hammerstein structure based on a macroscopic nonlinear model; and [35] used a fuzzy controller and compared the results with other strategies. The controller employed the Takagi-Sugeno-Kang fuzzy inference system (TSK FIS), which according to the error's magnitude, associated a voltage. It used a Gaussian function as a membership function to frame the errors (fuzzifier) and a weighted average method, as defuzzifier, to apply the voltages. This approach used maximum voltages, when the error was positive large, the PI controller output, when the error was small, and set the voltage to zero, when the error was negative large.

2.4.3 Hysteresis in SCP actuators

Although SCP actuators have a small hysteresis, especially when compared to other actuators, it still occurs under some conditions. Thus, this nonlinear effect took place, but the analyzed works did not handle it. So, this subsection presents methods applied to tackle this property.

The approach followed in [38] presented three models to characterize the hysteretic relationship between voltage input and contraction length of an SCP actuator, under different loads: the augmented GPI model (generalized Prandtl-Ishlinskii), the augmented Preisach model and the augmented linear model. The work obtained inverse models of the previous ones and canceled the hysteretic behavior through open-loop control. Both the augmented GPI and Preisach models displayed comparable modeling accuracy, but the Preisach's inverse model was computationally more expensive. As expected, the augmented linear model provided just a simple approximation. The authors of [39] adopted the Preisach

model in their work. They estimated the three-dimensional hysteretic relationship manifested by artificial muscles and used, once again, inverse compensation. The work targeted SMA actuators, but the method also confirmed its effectiveness for SCP and pneumatic actuators (of the McKibben type). Additionally, [40] applied a differential hysteresis model that employed the Duhem differential model, which updated the coefficients based on the output feedback. The model described the hysteresis between the displacement and temperature under several loads.

2.4.4 Summary

After reviewing the modeling and control strategies, there are aspects to take into consideration for the work ahead. To develop artificial muscles to apply in prosthetic devices, weight, volume, cost and overall complexity of the final solution, are factors to consider. Self-sensing actuators that provide indirect measurements of temperature are a valid solution. They enabled closed-loop control without external sensors, which helps reducing the volume and allows implementing actuators in small devices. Regular sensors that rely on direct contact with the actuator (thermocouples, thermistors, etc.) usually do not provide accurate results because it is difficult to establish a uniform contact surface between them and the actuator (due to its small diameter), which leads to irregular heat conduction. Even non-contact sensors, as infrared thermometers and cameras, display wrong measurements, due to the actuators' smaller diameter compared to their resolution (and they are too expensive) [19, 36].

Apart from that, control and modeling methodologies of antagonistic-type associations are also something to explore, because these structures can lead to faster expansions. This analysis verified that relationships between force and displacement and between temperature and displacement manifest the most relevant hysteresis, while the hysteresis between temperature and force is smaller [39, 40]. To obtain better tracking results, it might be necessary to combine inverse compensation and feedback control, as suggested in [38–40], which will consequently introduce extra sensing equipment. Also, capturing hysteresis through phenomenological methods is favorable, as it can represent different hysteretic behaviors (from different actuators' types) once their derivation comes from numerical data, instead of material properties as the physics-based models [39].

2.5 SCP actuators contraction and expansion

As shown in the literature, the slow heat transfer rate is a limitation of the SCP actuators - which is clear in the cooling process to restore the initial position, after a contraction. This section explores different cooling options, and other methods to mitigate this problem to possibly integrate with artificial muscles (i.e, the solutions have to be suitable to apply in a demonstration project).

2.5.1 Heat transfer based solutions

Cooling improvements suggested in [28] include increasing the air flow (forced air), immersing the actuator in water and embedding heat sinks in the design. Peltier devices are also an option, as men-

tioned in [2]. The working mechanism is based on the fact that electric current flowing through a junction, connecting two materials, will remove or generate heat at the junction. The work [9] tested the implementation of a Peltier device alongside SCP actuators and tried to prove its effectiveness with respect to the active heating and cooling processes, in order to develop prosthetic limbs. The drawbacks are the need of large and heavy structures and the performance of uniform heating and cooling (the long and thin shape of the actuators is an obstacle [32]). Immersing an actuator in water is also a valid solution, as [2, 10] did to identify its heating and cooling dynamics. Moreover, [16, 24] explored water injection through tubes to cool the actuators, and [24] used a silicone tube, to enable the flow of pumped hot and cold water, to contract and expand the inner SCP actuator. Despite the potential, the size and weight of the structures (pumps and water reservoirs) are a problem if the solution is to integrate with artificial muscles (Figure 2.3 (a)). Forced air via CPU fans is an option to achieve quicker cooling times, as tests in [2, 10, 19] show, plus the work [2] describes it as the best environment to achieve the fastest actuation. This was because of relatively fast cooling and heating times, due to the convective currents, but also because it displayed the best compromise between weight and power.

Apart from the discussed solutions, it is also possible to achieve a better heat transfer rate through better designed solutions. For instance, the orthotic hand presented in [26] embodied different layers, one of them with heat dissipation purposes. The spatial arrangement of the actuators (as in Figure 2.3 (b)) and the fibers' specifications are also important factors, as [19] verified: the thermal cooling time constant increased with the area increase of the fibers, but also with the closer the actuators were from each other.

2.5.2 Actuators' associations based solutions

In addition, there are other methods that do not tackle the heat/cooling transfer rates. It is possible to develop solutions to improve the conditions of the contraction/expansion motions. Human muscles can only actively contract, which means that they cannot expand by themselves. It is necessary an antagonist muscle, as discussed in 2.1. Therefore, it is plausible to implement a strategy based on such mechanisms. Some works suggest, as an option to get around the heat transfer rate problem, implementing pairs of antagonistic SCP actuators [2]. The goal is to achieve faster expansions, due to the improved association. The authors of [32] built an antagonistic actuator (Figure 2.3 (c)) that produced force in both the contraction and expansion directions, which was able to achieve better expansion response times. The work conducted experiments to validate the structure, using as benchmark a standard single SCP actuator. Additionally, [37] built a 1 DOF variable stiffness manipulator that employed multiple antagonist SCP actuators. A simple symmetrical structure developed in [23] (Figure 2.3 (d)) belongs to this discussion too, since whenever one of the actuators contracted, the other one expanded as a result, similarly to what an antagonist and agonist pair of skeletal muscles do. However, these solutions display a negative effect: when one actuator contracts the other one resists to that motion (it expands). The work done in [16] suggested other promising association, geometrically similar to the ones above. It uses heterochiral and homochiral SCP actuators, both produced via mandrel coiling, and

works based on the following principle: the heterochiral actuator expands and the homochiral actuator contracts with the application of electric current.

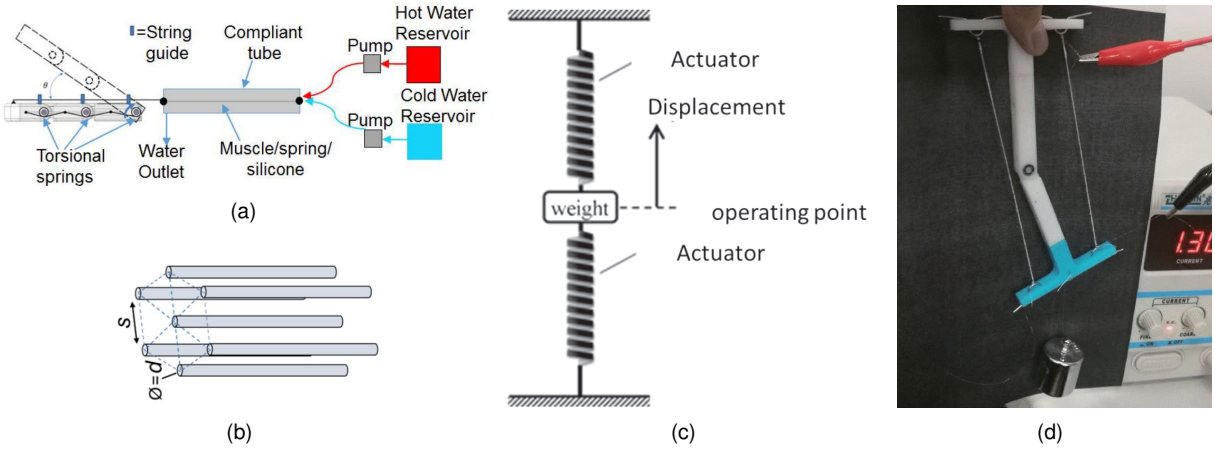

Figure 2.3: Contraction and expansion enhancement solutions with SCP actuators. (a) Schematic diagram of the experimental setup for water injection through tubes. (Adapted from [24]), (b) Hexagonal bundle configuration. (Adapted from [19]), (c) Antagonistic structure. (Obtained from [32]), (d) Symmetrical structure. (Adapted from [23]).

2.5.3 Springs and tendons based solutions

On the other hand, there are alternative approaches that employ springs to ease the overall actuation of the actuators. The work in [41] built a locking mechanism using a spring that enabled both the contraction and extension motions performed by two SCP actuators; [8] implemented springs to allow the SCP muscles to actuate after reaching their maximum contraction, preventing them to break; and [24] applied a spring as an extensor element (to intervene after contraction). Some works also used passive tendons (with no springs) to drive the movement easily [10, 26]. Also, it is possible to implement rubber bands to perform the extension part as well [8, 26].

2.6 Applications

To stress the importance of actuators, this section contains applications (related and non-related with artificial muscles) that take advantage from their properties. Since there are plenty of actuators' technologies, and each one has its own advantages, Table 2.3 gathers some of the recurrent applications of the actuators studied in 2.2. Secondly, a brief review provides concrete examples of application of SCP actuators in the bio-medical and bio-mechanical fields, especially in the orthotic and prosthetic areas, as artificial muscles.

Orthoses and prostheses are some of the most recurrent applications using SCP actuators as artificial muscles. A prosthesis is an artificial body part, such as an arm, that replaces a missing part and helps the disabled to replace the lost function; an orthosis is a device made to support an injured or badly formed part of the body, or to help someone to move it more easily (see Cambridge Dictionary).

Table 2.3: Common applications of the actuators studied in section 2.2.

Actuators	**Thermally activated shape-memory alloys (SMAs)**	**Pneumatic**	**Stimuli--responsive gels**	**Highly oriented semi-crystalline polymer fibers**
Examples of applications	Active catheters, stents, braces, active-compression garments, artificial muscles, airplane components (flaps), car components (headlight actuators), robotics (arms, legs, microgrippers) [4]	Robotics (grippers, arms, legs), soft manipulators, soft-bodied robots [4]	Artificial skins, programmable structures (folding/unfolding structures), adaptive lenses, drug delivery [4]	Smart windows, energy-harvesting systems, actuators for locks, smart fabrics, robotics (exoskeletons, and arms) [4]

As pointed out in [8], the majority of arm amputees live in developing countries and the high cost of suitable prostheses is a huge barrier to acquire them. Other problem is that young amputees quickly outgrow their prostheses, which demands a constant replacement [9]. For those reasons, [8] suggested a cheaper and customizable 3D printed hand prosthesis made of SCP actuators with 15 DOF, which was able to grasp different objects (Figure 2.4 (a)). The works [2, 10] built demonstration applications of a bicep muscle, for a robotic arm, and a dexterous robotic hand (which were able to perform various grasping maneuvers) to sustain the obtained results (Figure 2.4 (b) and (c)). Plus, [41] proposed a locking mechanism with SCP actuators to use in a 3D printable robotic hand, to avoid wasting energy while holding an object for long periods of time.

There are also works using SCP actuators in the orthotic field. Studies demonstrated that Parkinson or stroke patients paralyzed or weakened in one side of the body can regain motor function through continuous rehabilitation and therapy, which due to their repetitive nature, are possible to automate [26, 28, 42]. Thus, [28] designed a portable wearable wrist orthosis with 1 DOF to physiotherapists administer to their patients (Figure 2.4 (d)); [42] developed a wearable orthosis with hand rehabilitation purposes; and [26] built a 3D orthotic hand (Figure 2.4 (e)) - all of them using SCP actuators. The orthotic hand in [26] displayed good performance and potential, highlighted by the ability to grasp different objects, thanks to a well engineered design. Additionally, [22] presented a concept of a hand exoskeleton, made of SCP actuators, for patients with spastic hand syndrome exercise their hands. The work did not achieve the repetitive motion of opening the hand, because the contraction force was not enough to overcome the hand spasticity, however, showed some satisfactory results.

It is also worth noting the work done in [43], whose goal was to replicate the pennate muscle structure (which delivers high forces with small motion). The structure used multiple SCP actuators to induce a change in the overall stiffness by actuating them individually - similarly to the process in the human muscles, where the control is on each muscle fiber to generate the proper amount of force (see 2.1). The works [9, 24] are interesting too, since they explored different cooling methods to integrate in future robotic hands projects.

Other advantages, from introducing SCP actuators in this field to produce these solutions, are their light weight (DC motors and their gear mechanisms are heavy), controllability (small hysteresis), power-to-weight ratio, increased dexterity and more natural shape and feel. Although the final solutions lack the quality that a fully functional prosthesis/orthosis would require, it is worth mentioning that the results

demonstrated the overall applicability of the SCP actuators, and also suggested a promising path to follow. Nevertheless, there are some features that need improvement in the future such as, energetic efficiency, introduction of a real wrist-type mechanism, response time and implementation of a control system according to user intent. As proposed in [21], it is promising to combine different types of actuators in the future, trying to make an overall better solution, where each actuator's strength overcomes the other actuator's weakness.

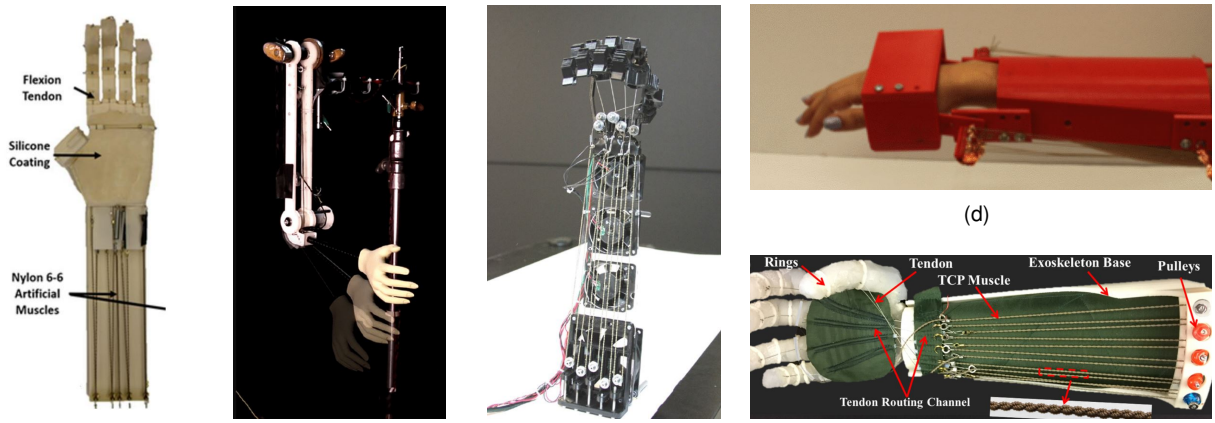

(a) (b) (c) (d) (e)

Figure 2.4: SCP actuators' applications. (a) Prosthetic hand. (Adapted from [8]), (b) Robotic arm, (c) Robotic hand. (Both adapted from [2]), (d) Wrist orthosis. (Adapted from [28]), (e) Orthotic hand. (Adapted from [26]).

Chapter 3

Methods

This chapter presents the guidelines and parameters to perform a clear manufacturing process. It also discusses the steps to derive and acquire the model, and the control scheme.

3.1 Manufacturing

This section will review, in detail, all the phases involved in the manufacturing process of SCP actuators. Appendix D.5 contains videos about the working principle and manufacturing process.

3.1.1 Manufacturing setup

The experimental setup employed along all the manufacturing stages is in Figure 3.1. Note that the work did not use all the components at the same time. The main goal of the presented structure is to twist and coil the nylon fibers, but also, to perform the training stage and some experiments for the modeling and control stages. The framework's material is wood, to create a rigid and steady structure to support heavy weights hung on the fiber. The design considered the production of long SCP actuators - placing the structure at the edge of a table, nylon fibers can be as long as the distance to the ground. Appendix A.1 lists the components and their tasks; Appendix A.2 shows the circuit diagrams. The materials used are not expensive and are lightweight. The work handled PWM values as voltage potentials (255 PWM - 100 % duty cycle - corresponds to 3.7 V), with the exception of Appendix D.1 graphs.

3.1.2 Twisting and coiling

The work selected the linear and auto coiled type of actuators, since the linear motion fitted the end purpose of this work, and because mandrel coiled actuators were more challenging to manufacture (and would require multi-filament fibers). Thus, SCP actuators' manufacturing used mono-filament fibers, which require a resistive wire to actuate the muscle via Joule heating. This choice, as seen in chapter 2, took into account the price of the final solution, the availability of the materials and future performance and lifetime. Table 3.1 lists the employed materials, and Table B.4 the materials used in the literature.

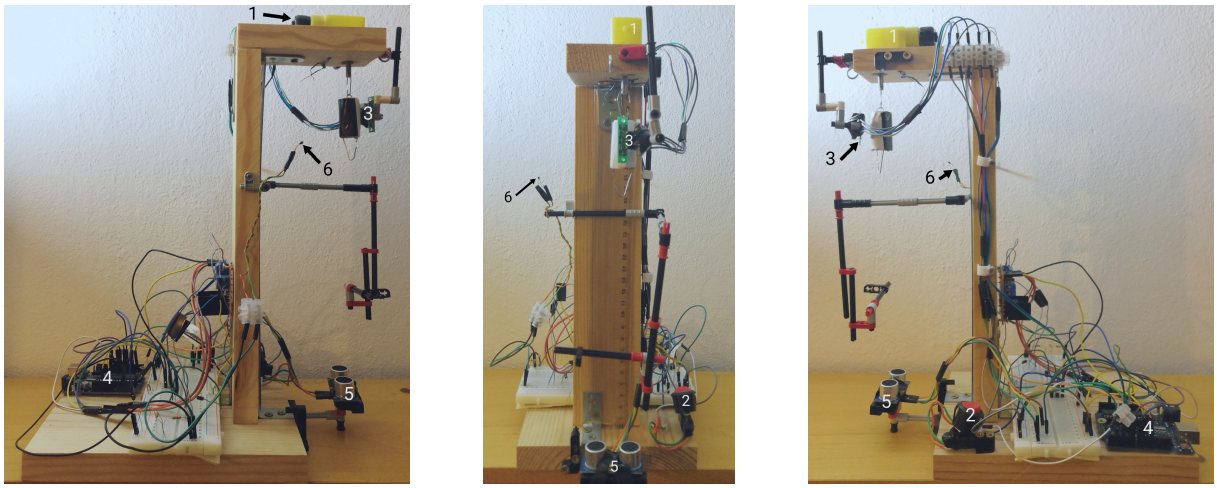

(a) (b) (c)

Figure 3.1: Manufacturing process experimental setup.

Before attaining functional actuators, different methods during the process attempted to twist and coil the nylon fibers. At first, one tried to wind the copper around the nylon, and then twisting and coiling them together, with a suitable weight. After several trials, the actuators were not able to conduct electrical current, possibly because the copper wire broke during the twist and coiling process. The second method attempted to twist the nylon first, up to the moment it starts coiling, so one could start the copper winding process from that point. After the copper winding, the next step was to twist the resulting product, until all the coils formation, this time using an additional weight (the actuator's stiffness rises due to the copper). The actuator was able to conduct electrical current, but the work did not follow this process, since winding copper around such a thin fiber was very challenging. The adopted technique, consisted of twisting the nylon fiber until all the coils formation, using the smallest weight possible that did not tangle the fiber, while preventing it from twisting together with the motor (Figure 3.2 (a)-(c)). The whole manufacturing process operation was under the ambient temperature (≈ 23 °C). Figure 3.2 depicts all the steps involved in the twisting and coiling stages, and Table 3.2 gathers its parameters.

Table 3.1: Manufacturing: materials used to produce SCP actuators.

Materials	**Diameter (mm)**
Standard nylon mono-filament fishing line	0.23 / 0.33 / 0.45
Enameled copper wire	0.10

3.1.3 Annealing and training

The annealing stage's goal was to set the polymer's structure. The dissertation displays two methods to prevent the muscles from untwisting: using an oven and plying them onto themselves. The actuators fabricated with the oven had to sustain a certain elongation using a frame, to avoid untwisting during the annealing process (Figure 3.2 (d), (f)). Elongation values around 112 % worked fine. Nevertheless, [28] employed an elongation of 130 %, whereas other works used the elongation created by the twist

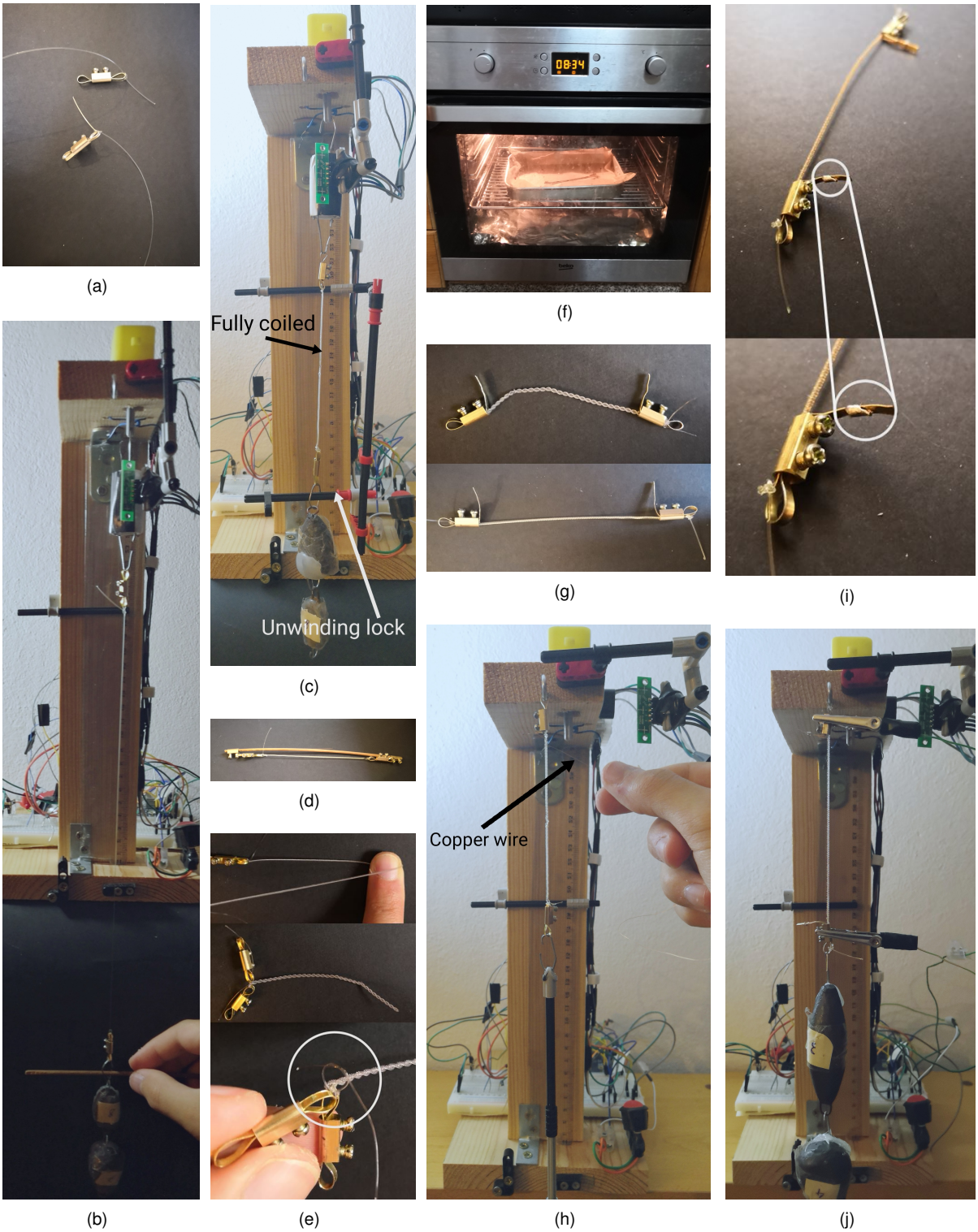

Figure 3.2: Steps to produce both 1 ply and 2 ply actuators. (a) Both ends of the fishing line are tied to the loop locked in each terminal block, (b) Motor spins clock wise with a weight hung, while the fiber's end is prevented from twisting, (c) Motor is turned off when all coils are formed, (d) For the 1 ply configuration: the actuator is stretched and framed in a special structure to prevent untwisting, (e) For the 2 ply configuration: the actuator is folded onto itself, and the ends are tied, (f) The actuator is placed in the oven for the annealing process, (g) The actuator is removed from the frame (1 ply case), and each one of its ends is locked to the terminal block, to be more practical and safe in future occasions, (h) The actuator is fixed with a small tension to avoid being slack, so it can be wound by copper wire, (i) The copper wire is welded in both tips of the terminal blocks, (j) Voltage is applied by alligator clips while a weight, twice as heavy as the twisting and coiling one, is hung, to perform the training stage.

Table 3.2: Manufacturing: twisting and coiling parameters.

Parameter	SCP actuator code								
	1	2	3	4	5	6	7	8	9
Chapter/ section[a]	4.3.2	3.3.3; 4.3; 4.4; 4.1.2; 4.2.1	4.1.2; 4.2.1; 4.3.2	4.1.2; 4.2.1; 4.3.2	4.1.2; 4.2.1; 4.3.2	4.1.2; 4.2.1; 4.3.2	4.1.2	4.1.2 3.3.2	4.1.2
Fishing line diameter (mm)	0.23	0.33	0.45	0.23	0.33	0.45	0.23	0.33	0.45
Fishing line length after tied (cm)	40	40	40	100	100	100	55	55	55
Weight (g)[b]	40.4	82.7	150.9	40.4	82.7	150.9	40.4	82.7	150.9
Stress (MPa)	9.53	9.48	9.30	9.53	9.48	9.30	9.53	9.48	9.30
Nr. of revolutions to start coiling	400	305	220	975	770	555	545	440	315
Nr. of total revolutions	621	500	356	1557	1186	948	856	675	514
Revolutions per minute without any weight hung	145								
Actuator length after twist & coiling w\weight hung (cm)	8.1	8.8	8.6	20.1	21.7	21.9	11.5	11.2	12.0

[a] Chapters/sections that used the SCP actuators of this table. [b] Measured with the KERN EMB 500-1 precision electronic balance.

and coiling weight or even by the training weight. The relation displayed between temperature and time inside the oven (tests in 4.1.1) avoids melting the fiber and prevents the coils to become glued to each other. After several trials and broken actuators, the actuators' structure underwent a rearrangement (in the fiber's attachment to the actuators' tip) to enable the use of heavier weights without breaking the fishing line (Figure 3.2 (g)). The plied actuators (Figure 3.2 (e)), did not use the oven, but their structure incorporated the rearrangement as well (Figure 3.2 (g)). Table 3.3 lists the annealing stage specs.

Table 3.3: Manufacturing: annealing stage parameters.

Parameter	SCP actuator code								
	1	2	3	4	5	6	7	8	9
Length after framing (cm) - elongation (%)	9.5 - 117.3	9.9 - 112.5	9.4 - 109.3	Not applicable			12.7 - 110.4	12.2 - 108.9	13.2 - 110.0
Annealing type	Oven (warm hair)			2 ply configuration			Oven (warm hair)		
Annealing specs	135 °C 12 min (preheat oven for 5 min)			Not applicable			135 °C 12 min (preheat oven for 5 min)		
Length after annealing (cm)[a] **- with new structure (cm)**	9.5 - 7.5	9.9 - 7.5	9.4 - 7.5	8.6 - 7.5	9.3 - 7.5	9.4 - 7.5	12.7 - 10.5	12.2 - 10.5	13.2 - 10.5

[a] Length after removing the actuator from the frame without any weight hung, for the 1 ply case, and length after folding the SCP actuator onto itself for the 2 ply case, also without any weight hung.

The next steps were equal to both actuators' types (1 and 2 ply). To Joule heat them, the process was to wind copper wire around them, covering all the length, followed by the welding of the copper

to each actuator's terminal block tip (Figure 3.2 (h-i)). This was a careful manual process to uniformly distribute, along the actuator's length, all the copper wire, while trying to maintain equally spaced copper turns (Figure 3.3). This step is extremely important, since entails the uniform heating of the actuator, and because tighter turns will cause the actuator to break when heated. The final step is training. To do that, and considering different methods in the literature, the weight was twice as heavy as the one employed during the twisting and coiling stage, for the 1 ply case (Figure 3.2 (j)), and five times heavier, for the 2 ply case. This decision was a result of the visible displacements produced with those weights (more than 10 mm) under the applied voltages, but also because of the elongations magnitude (see Table 3.4) after the training phase. The battery was rechargeable, light weight (21 g) and had small dimensions ($4.4 \times 3.6 \times 0.6$ cm). Plus, the voltage values applied by the battery, enabled relatively fast actuation responses from the muscles ($\approx$ 5 s) during the training phase, without surpassing the melting point. The voltage values and actuation times to perform the training stage were the combination of both that led to the fastest responses/maximum displacements without breaking or excessively elongate the actuators.

Nonetheless, one should use a smaller ON time period in the first cycle of training, because the actuator heats up for the first time, and elongates as a result. Plus, the elongation motion, caused by the weight and heat, made the actuator prone to break or to elongate in a non-reversible way (in a way that would not restore the original position during the OFF phase). So, reducing the ON time period, in the first training cycle, to half the value of the other cycles is a good practice. Figure 3.2 shows the steps about manufacturing SCP actuators (see video in Appendix D.5) and Table 3.4 lists the training stage parameters. Appendix B.1 contains the manufacturing parameters of the remaining actuators.

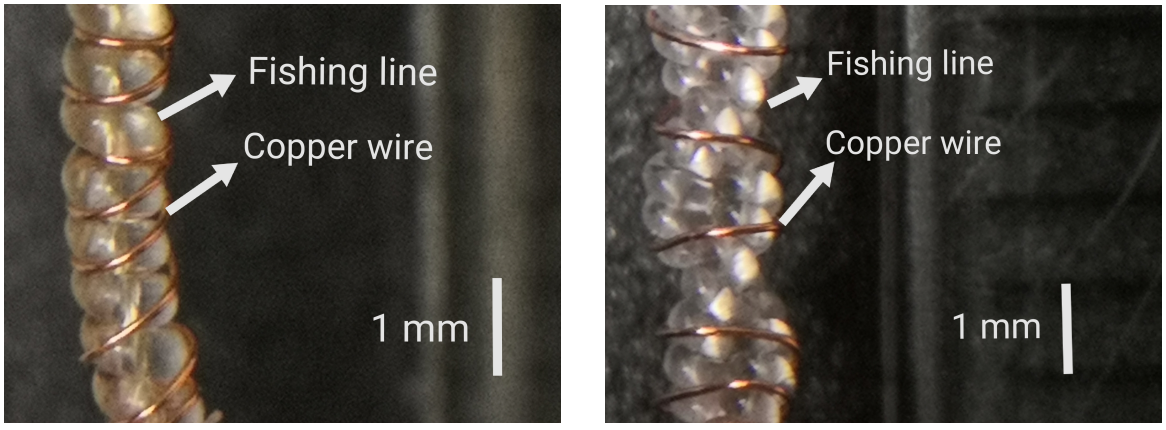

(a) (b)

Figure 3.3: Zoomed pictures showing, in detail, copper wire turns wrapped around different SCP actuators. (a) 1 ply actuator, (b) 2 ply actuator.

It is also important to stress that the task of choosing the best voltage to apply to each actuator, that will maximize its displacement, is difficult. Factors like the possible loss of the battery's efficiency over the time and even unnoticeable glitches on the manufacturing process (namely in the copper winding stage) may lead to inconsistent results, so one should not overlook them. Nevertheless, the work contributed to provide and set suitable ranges of values to apply, according to each situation.

Table 3.4: Manufacturing: training stage parameters.

SCP actuator code	Copper wire length (cm)	Theoretical resistance of the copper wire (Ω)[a]	Nr. of copper wire turns around the SCP actuator[b]	Training type	Training specs	Length after training (cm) - elongation (%)
1	45	0.96	190	Joule heating (electrothermally)	3.26 V (11.10 W) 5 s ON & 20 s OFF w\82.7 g hung (10x)	9.3 –124.0
2	50	1.07	170	Joule heating (electrothermally)	3.41 V (10.87 W) 8 s ON & 25 s OFF w\160.4 g hung (10x)	9.0 –120.0
3	61	1.30	155	Joule heating (electrothermally)	3.55 V (9.72 W) 10 s ON & 30 s OFF w\299.7 g hung (10x)	8.0 –106.7
4	45	0.96	98	Joule heating (electrothermally)	3.26 V (11.10 W) 5 s ON & 20 s OFF w\200.8 g hung (10x)	9.0 –120.0
5	51	1.09	100	Joule heating (electrothermally)	3.41 V (10.67 W) 8 s ON & 25 s OFF w\412.9 g hung (10x)	8.5 –113.3
6	62	1.33	95	Joule heating (electrothermally)	3.55 V (9.50 W) 15 s ON & 40 s OFF w\754.6 g hung (10x)	10.4 –138.7
7	52	1.11	205	Joule heating (electrothermally)	3.26 V (9.60 W) 10 s ON & 30 s OFF w\82.7 g hung (10x)	11.3 –107.6
8	60	1.28	195	Joule heating (electrothermally)	3.41 V (9.08 W) 12 s ON & 35 s OFF w\160.4 g hung (10x)	11.7 –111.4
9	72	1.54	185	Joule heating (electrothermally)	3.55 V (8.21 W) 20 s ON & 40 s OFF w\299.7 g hung (10x)	11.2 –106.7

[a] Considering the copper resistivity equal to $1.68 \times 10^{-8}\Omega \cdot m$ at 20 °C. [b] The actuator is fixed in a structure to create enough tension to wind the copper wire (as shown in Figure 3.2 (h)).

3.2 Contraction and expansion

This section presents the solutions used to enhance the contraction and expansion times of SCP actuators (see the results in 4.2). The work dismissed using Peltier devices, fans, water immersion and injection tubes, since they would lead to large and heavy structures, and higher costs. The solutions considered the human body, since antagonist muscles help the extension task (Figure 3.4). Thus, the work reassessed the associations in 2.5.2. Moreover, isotonic contractions include the upper limb and finger movements, and since they cover the concentric and eccentric contractions (which relate to agonist and antagonist muscles) was obvious to pursue this approach, and reproduce similar structures.

3.2.1 AAA with 2 SCP actuators

The first trial used 2 SCP actuators disposed side by side, at a fair distance from each other to avoid crosstalk. The AAA's body fixes one end of each actuator, while the other links to the pulley (which converts linear motion into an angle). When one actuator contracts, the pulley rotates and generates an

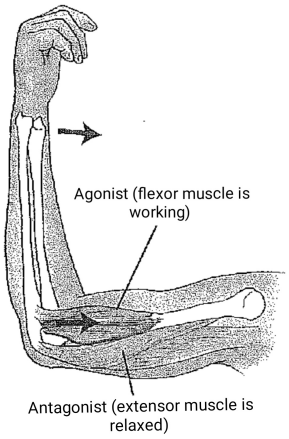

Figure 3.4: Brachialis and triceps brachii agonist/antagonist interaction (Adapted from [12]).

angle between actuators (Figure 3.5 (a)). The principle was to apply voltage to one actuator, inducing its contraction (agonist) and the other actuator's expansion (antagonist), simultaneously. To resume to the rest position, the roles were the inverse (see video in Appendix D.5 about the AAA's working process).

This experiment took into account other works. The 1 DOF manipulator in [37] displayed the same working principle with a different goal. The work in [16] suggested a similar application with the same association between actuators, but used water injection tubes and mandrel coiled homochiral and heterochiral actuators, both actuated by voltage at the same time. Plus, the approach in [23] also shares the same principle, but the structure was geometrically different (see Figure 2.3 (d)).

3.2.2 AAA with a spring and 1 SCP actuator

Now, a new configuration with a spring (with a suitable stiffness) was in place (Figure 3.5 (b)). The structure is the same, apart from the spring instead of an actuator. The goal was equal, but this time the contraction of a spring, previously expanded, induces the expansion. Another goal was to understand which of the solutions extended faster, and to conclude if there was an energetic advantage of using one actuator. Further on, the AAA also tested a rubber band (Figure 3.5 (c)), as justified in 4.2.3.

Again, this work considered similar approaches. The work in [26] used rubber bands for the extension after the actuators' contraction and [24] applied the same idea differently, placing a spring and a muscle inside a flexible silicone tube to restore the initial position faster (see Figure 2.3 (a)).

Some muscles (as the brachialis in Figure 3.4) can work as agonist and as antagonist, depending on the situation [12]. With two actuators it is possible to induce contractions by heat. So, in this case, the SCP actuator is the agonist, and the spring works as the antagonist (only contracts if previously expanded). Together with the results in 4.2, the adopted solution follows the AAA with two SCP actuators.

3.3 Modeling strategy

This section's goal is to derive a model for the AAA's behavior to allow good simulations results. The computation of the coefficients that identify the model is also a priority. Since the literature shows

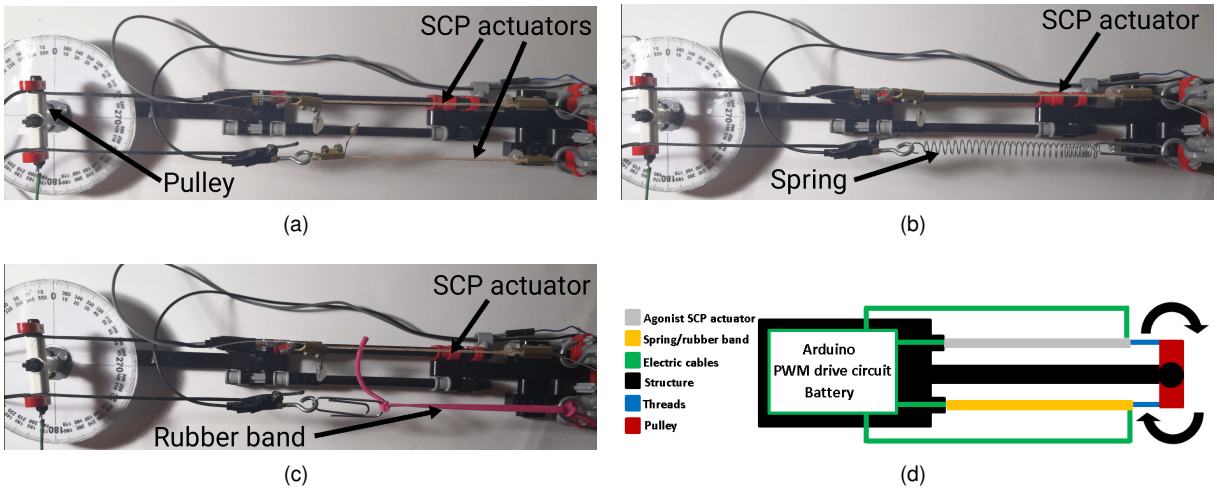

Figure 3.5: Implemented solutions to deal with the contraction/expansion issue. AAA (a) with 2 SCP actuators, (b) with a spring and 1 SCP actuator, (c) with a rubber band and 1 SCP actuator, (d) diagram.

several ways to model SCP actuators (from simple to complex linear and nonlinear models) a choice is essential, considering the equipment available and the system's characteristics.

The work dismissed the black-box methodologies in 2.4.1 since they would relate the output with the input data, which would make the process of estimating the model's parameters nearly impossible. The need to re-identify the model, for different actuators [34], was also a drawback, despite working with simple model forms and solutions, as well as including uncertainty effects. White-box methodologies (purely theoretical models) did not fit the work too, because of the complexity of the mathematical methods, and because they could not model uncertainty. Thus, the work adopted a grey-box methodology, since it combines theoretical information, about the model behavior, with experimental data, and because enables the model parameters' estimation with the results. Although it requires re-identification [32], this strategy reduces the complexity of the model, and tackles the lack of theory (to describe the dynamics) and appropriate experimental data for validation [44].

3.3.1 Grey-box modeling

The work implemented two models to describe the actuator, as in the works of Yip and Niemeyer [2, 10]: the thermoelectric (TE) relates the input power with temperature, and the thermomechanical (TM) computes the displacement, of a single actuator, given the temperature (Figure 3.6 (a)).

The TE model describes the dynamics of applying a voltage potential to the copper wire that heats the actuator by Joule effect. It comprises the electric power and the Newton's law of cooling (which states that the losses of a body by heat are proportional to the temperature difference between the body and the environment). The model formulation is in [2, 10], and is as follows:

$$C_{th}\frac{\mathrm{d}\Delta t(t)}{\mathrm{d}t} = P_{in}(t) - \lambda\Delta t(t), \tag{3.1}$$

which is equivalent to

$$C_{th}\frac{\mathrm{d}\Delta t(t)}{\mathrm{d}t} = \frac{v^2(t)}{R} - \lambda\Delta t(t). \tag{3.2}$$

C_{th} (Ws/°C) is the thermal mass of the actuator, λ (W/°C) is the actuator's absolute thermal conductivity at the ambient temperature; the applied voltage $v^2(t)$ (V) and the copper wire resistance R (Ω) represent the electric power ($P_{in}(t)$), and finally, $\Delta t(t)$ is the temperature variation from the environment to the actuator's temperature (°C). Applying the Laplace transform to (3.2), and considering the initial conditions set to zero, the transfer function of the model is as follows:

$$\frac{\Delta T}{V^2} = \frac{\frac{1}{RC_{th}}}{(s + \frac{\lambda}{C_{th}})}. \tag{3.3}$$

One can interpret (3.1) as the actuator's internal energy, i.e., as the result of the difference between the input energy (voltage potential) and the energy lost by convection to the surroundings (by the resistive wire). Note that the applied voltage, V^2, is squared to maintain the model linear. So, the voltages fed to the model will be squared, regarding its true value. This is true until direct tests on the real system (these tests do not demand squared voltages since they do not use the model for the results).

The TM model describes how the change in temperature influences the displacement of a single SCP actuator (Figure 3.6 (b)). As before, the TM model took into account the works [2, 10]. The model uses the linear mass-spring-damper model, as follows:

$$m\frac{\mathrm{d}x^2(t)}{\mathrm{d}t^2} + \beta\frac{\mathrm{d}x(t)}{\mathrm{d}t} + kx(t) = C\Delta t(t), \tag{3.4}$$

where m (kg) is the mass, k (N/m) is the spring stiffness, β (Ns/m) is the damping coefficient, $\Delta t(t)$ (°C) is the temperature variation, in relation to the environment temperature, C (N/°C) is a proportional coefficient that reflects how temperature changes affect the force, and $x(t)$ (m) is the displacement. Applying the Laplace transform to (3.4), leads to the following transfer function:

$$\frac{X}{\Delta T} = \frac{\frac{C}{m}}{(s^2 + s\frac{\beta}{m} + \frac{k}{m})}. \tag{3.5}$$

Rewriting (3.3) and (3.5) as in Appendix C.1, helps to obtain the model of the actuator that relates the input power with the displacement, by combining the given expressions. Thus, from replacing ΔT in (C.1) by (C.2) comes

$$\frac{X}{V^2} = \frac{\frac{C}{C_{th}mR}}{s^3 + (\frac{\beta}{m} + \frac{\lambda}{C_{th}})s^2 + (\frac{k}{m} + \frac{\lambda\beta}{C_{th}m})s + \frac{\lambda k}{C_{th}m}}. \tag{3.6}$$

Recalling the initial goal of describing the AAA's behavior, the work redesigned the model to embody the system dynamics (2 actuators in a parallel association) to compute the angle variation. This model includes one actuator's contraction and the other actuator's pulling opposing force. The AAA's components are in parallel, since they share the force, and all of them reveal the same displacement (velocity), if actuated. Other features to consider are both actuators' ends attachment to the AAA's body, and the existence of a pulley - which accelerates because of the active SCP actuator's force, and has a moment of inertia equivalent to a solid disk. All of these factors will affect the dynamics of the AAA. Following the design proposed in Figure 3.6 (c) and the constraints above, the work derived a 2^{nd} order linear ordinary differential equation for the AAA's TM model (3.7) - see Appendix C.2 for details about its computation.

$$\left(\frac{1}{2}m_p + m_1 + m_2\right)\frac{\mathrm{d}^2\theta(t)}{\mathrm{d}t^2}r_p + (\beta_1+\beta_2)\frac{\mathrm{d}\theta(t)}{\mathrm{d}t}r_p + (k_1+k_2)\theta(t)r_p = C_1\Delta t(t). \tag{3.7}$$

The index nr.1 represents the terms related with the agonist actuator, and the nr.2 the terms related with the antagonist; m_p and r_p are the pulley's mass and radius, and $\theta(t)$ is the angle (radians). Applying the Laplace transform to (3.7) and then rewriting the outcome in order of the temperature variation leads to

$$\frac{\left(\frac{1}{2}m_p + m_1 + m_2\right)}{C_1}s^2\Theta r_p + \frac{(\beta_1+\beta_2)}{C_1}s\Theta r_p + \frac{(k_1+k_2)}{C_1}\Theta r_p = \Delta T. \tag{3.8}$$

Replacing (3.8) in (C.1), i.e., combining the AAA's TM model with the agonist's (active actuator) TE model, results in

$$C_{th}a\Theta s^3 + C_{th}b\Theta s^2 + C_{th}c\Theta s = \frac{V^2}{R} - \lambda a\Theta s^2 - \lambda b\Theta s - \lambda c\Theta, \tag{3.9}$$

where

$$a = \frac{\left(\frac{1}{2}m_p + m_1 + m_2\right)}{C_1}r_p, \quad b = \frac{(\beta_1+\beta_2)}{C_1}r_p \quad \text{and} \quad c = \frac{(k_1+k_2)}{C_1}r_p. \tag{3.10}$$

Finally, one can rearrange (3.9) to relate the input power with the angle variation of the AAA, as expressed by

$$\frac{\Theta}{V^2} = \frac{b_0}{s^3 + a_2s^2 + a_1s + a_0}, \tag{3.11}$$

where

$$a_2 = \frac{b}{a} + \frac{\lambda}{C_{th}}, \quad a_1 = \frac{c}{a} + \frac{\lambda b}{C_{th}a}, \quad a_0 = \frac{\lambda c}{C_{th}a} \quad \text{and} \quad b_0 = \frac{1}{RC_{th}a}. \tag{3.12}$$

The work did not consider hysteresis (namely between voltage and strain), since the adopted association between actuators overcomes this problem. The action of the antagonist imposes the agonist's expansion motion, thus, this flexible relation between active and non-active actuators performs the angle control. By controlling the heating stage (active actuators) to attain the desired goal, ignoring the cooling dynamics, enables the dismiss of the hysteresis effect, and the use of a less complex model. Although SCP actuators have a nonlinear behavior [30, 31], the work did not adopt such models, despite being more accurate. Complex models would be harder to implement and more demanding computationally, due to the high number of parameters. Also, for this work's goal, models that fit the identified system with $\approx$ 80 % accuracy, are good approximations to conclude about the results. Moreover, previous works showed good results, despite using simpler models [2, 5, 10, 27, 28, 32, 33], as seen in 2.4.1.

3.3.2 Acquisition methods

Temperature acquisition method

It is important to set how to acquire the temperature to study the actuators' operation conditions (tests in 4.1.1 revealed that the nylon melted at $\approx$ 165 °C). The work measured the temperature directly with a thermistor placed closely to the actuator, without any load, as in Figure 3.7 (a). Two experiments assessed the relation between temperature and voltage, and the time associated to the cooling and heating stages. The first, measured the increase of temperature (until the maximum value) via voltage

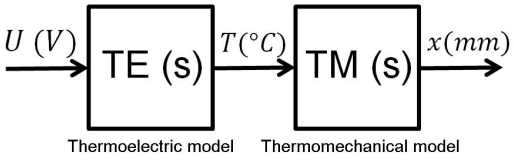

(a)

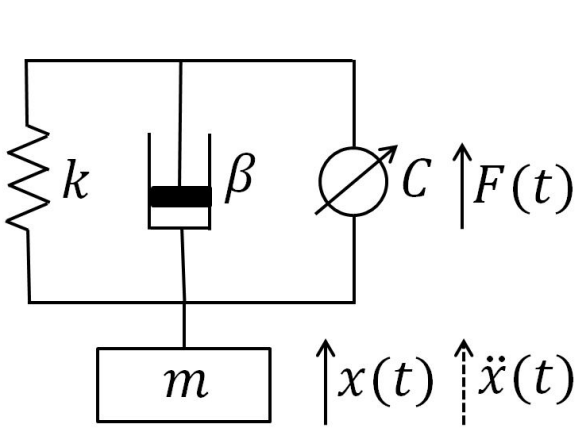

(b)

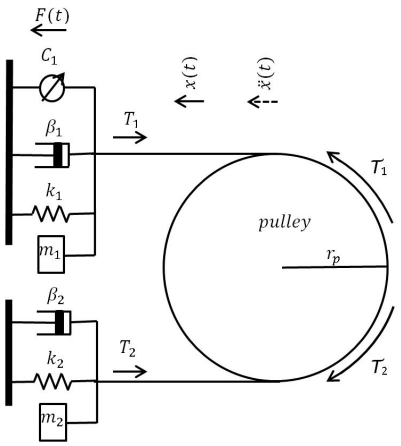

(c)

Figure 3.6: Graphical representation of the adopted models. (a) Block diagram of the SCP actuator's model, (b) TM model of the SCP actuator, (c) TM model of the AAA structure.

increments every 100 s (to meet the steady state) followed by decrements, every 180 s, and the second measured, at a time, the temperature rise from 0, to different voltage values (Figures 3.7 (b) and (c)). Both experiments used actuators equivalent to actuators nr. 1, 16 and 17. The circuit is in Appendix A.3.

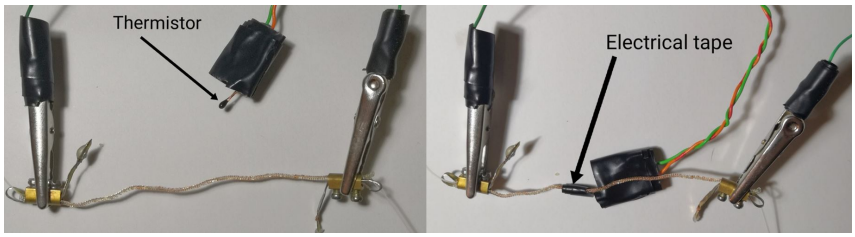

(a)

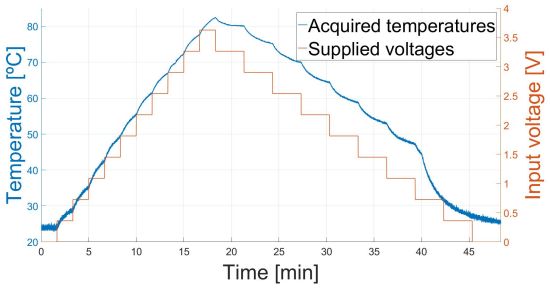

(b)

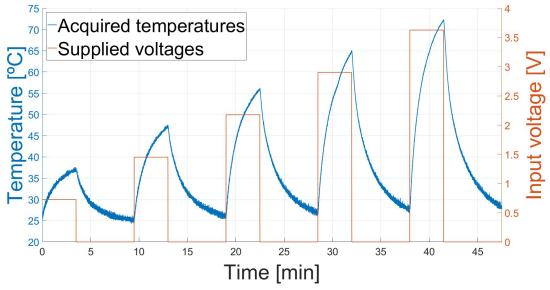

(c)

Figure 3.7: Temperature direct measurement tests. (a) Experimental setup, (b) First experiment results, (c) Second experiment results.

As expected, resuming to cooler temperatures was slower than reaching higher temperatures. Still, both processes were slow (it took minutes for the read temperature to start stabilizing), despite the

typical lag introduced by the thermistor. In addition, the maximum value measured was ≈ 83 °C (Figure 3.7 (b)), but it is fair to conclude that the actuator's real temperature was slightly higher. This is because there was some damage in the actuator's nylon, caused by the contact with the copper, and because some of the coils became glued to each other (which suggests values between 150 and 165 °C - see 4.1.1). Measuring higher temperatures is possible, providing more time between increments, however, it is unlikely to measure values close to 165 °C, since the heat distribution is not uniform, as in the oven, and the actuator would melt before the thermistor register that value. A reason to justify the lower temperatures may be the not maximized contact surface between the sensor and the actuator.

A test also measured the temperature indirectly, through the resistance of the copper wire (circuit in Appendix A.3), since it varies with the temperature, as the works in [19, 20, 29, 30, 34–36] acknowledge. This test adapted the circuit employed in [19] and used the actuator nr. 8. The resistance computation was via the knowledge of the current value (125 mA, due to the constant current circuit) with the value of the acquired voltage. The procedure was to apply directly 3.7 V to the actuator, for a small period of time (≈ 2 s), and measuring, immediately after, the resistance with the resistance measurement circuit. The successive resistance values R conversion to temperature (Figure 3.8) followed

$$R = R_0(1 + \alpha(T - T_0)) \implies T = \frac{R - R_0}{R_0\alpha} + T_0, \tag{3.13}$$

where R_0 is the resistance at the reference temperature, T_0 (22 °C), and α is the temperature coefficient of resistance for copper (α = 0.00404 K^{-1}, at 20 °C). From Figure 3.8 one can see that the resistance value is 2 Ω, immediately after removing the applied voltage, and decreases, smoothly, until 1.4 Ω after 20 s (this test would eventually reach a closer value to the actuator's resistance - 1.28 Ω - if given more time). The maximum temperature value was ≈ 160 °C and the minimum was ≈ 53 °C (again, the test would eventually attain the room temperature if the experiment was longer).

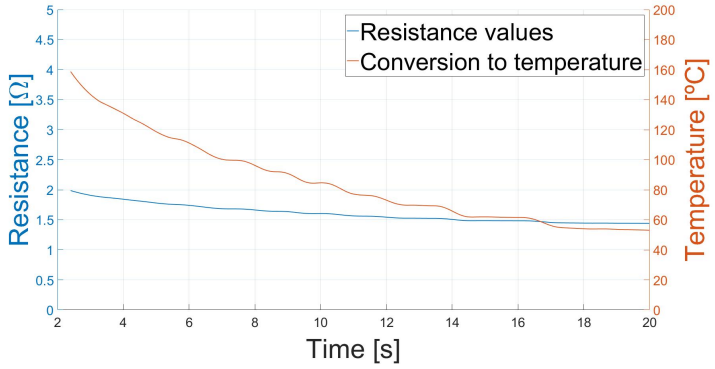

Figure 3.8: Temperature indirect measurement test: resistance and temperature variation of the SCP actuator immediately after heated.

The resistance measuring circuit would bring extra challenges regarding its association and dynamic interaction with the PWM drive circuit, already in place; plus, the temperature obtained would not correspond to the actuator's real temperature too, but to the copper wire temperature, although it would be closer to the real value. In the end, it was more convenient to measure the temperature directly.

Angle acquisition method

The work had to acquire the AAA's angle (output of the TM model). So, one used a potentiometer to measure the angle directly, via the resistance variation induced by its rotation when one of the AAA's actuators contracts (Figure 3.9 (a)). After successive AAA redesigns and trying different kinds of SCP actuators, one could not acquire the angle with this method, since the angle change was barely visible. The potentiometer rotation friction and the antagonist actuator stiffness were greater resistive forces, than the displacement force produced by the agonist. The effort to use a low cost sensor and widely available materials to create an affordable AAA led to the described limitations. This prevented the use of a feedback control strategy and the estimation of the coefficients of the AAA's transfer function (3.11).

Displacement acquisition method

Measuring the displacement was an alternative, since there is a relation between the angular and linear motions. This method used an ultrasonic sensor, however, the displacement measurement was not possible with the actuators placed in the AAA, which led to conduct individual measurements, hanging weights on each actuator (Figure 3.9 (c)). This prevents the direct use of the derived model (3.11) to estimate the parameters, because the collected data would be relative to a single actuator's behavior, instead of the actual agonist/antagonist relation, displayed by the AAA. Thus, the model (3.6) will be the one to employ later on, to estimate the parameters, as it is the only that fits the acquired data.

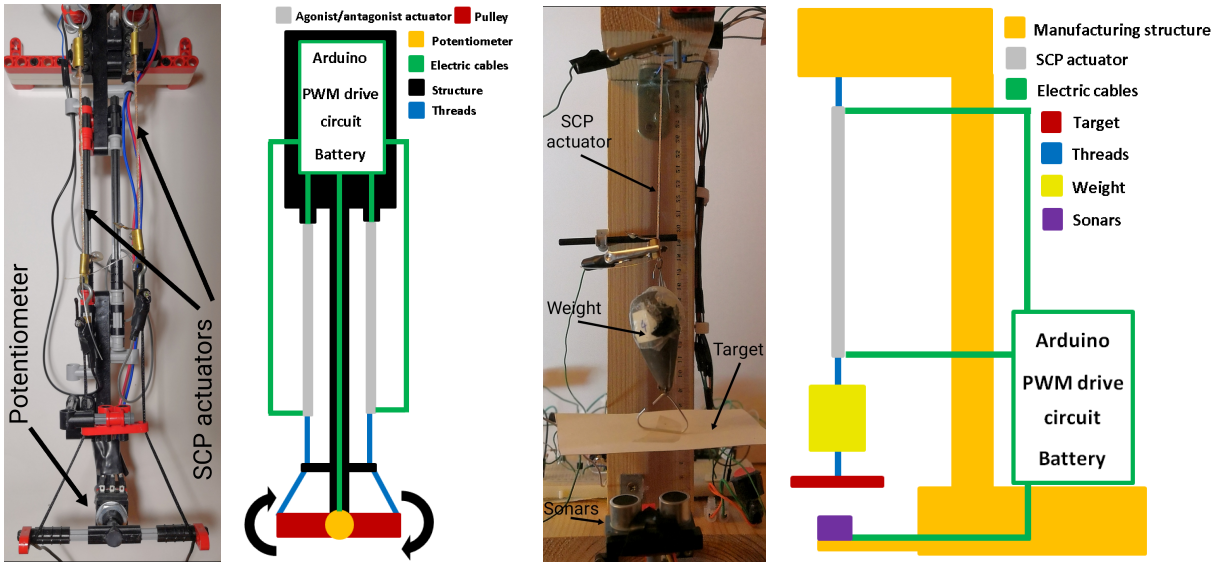

(a) (b) (c) (d)

Figure 3.9: Setup for the TM model output. (a) Angle, (b) Diagram, (c) Displacement, (d) Diagram.

3.3.3 Acquiring and processing data

Good identification results require adjusting and processing the acquired data to remove undesirable features. Sensors and other components usually introduce high frequency noise, so, filtering the data with a low pass filter is a must, as well as working with null mean signals, by removing their off-set trend.

The data-sets used to model a single SCP actuator (code nr. 2) were the applied voltage (input) and the temperature (output) for the TE model; the temperature (input) and the displacement (output) for the TM model; and the applied voltage (input) and the displacement (output) for the plant model, as Figures 3.10 (a) - (c) show. The input signal was a voltage step difference, since it was representative enough to obtain a robust model, i.e., comprises all the actuation modes of interest (the dynamics of the heating phase/contraction). The temperature acquisition was with the setup in Figure 3.7 (a) (but with an 82.7 g weight hung), and the displacement acquisition was as the Figure 3.9 (c) shows, with an 82.7 g load suspended. The temperature and displacement acquisition was not simultaneous, since placing the thermistor in the actuator would affect the displacement amplitude. So, the data-sets shown in Figures 3.10 (b) and 3.10 (e) combined the TE model (after undergone decimation) and the plant data-sets. A MATLAB program, created for this purpose, obtained the processed signals in Figure 3.10 (d) - (f) (using the system identification toolbox with the remove means and filter operations would be a valid option too). Appendix A.3 contains both the employed circuits.

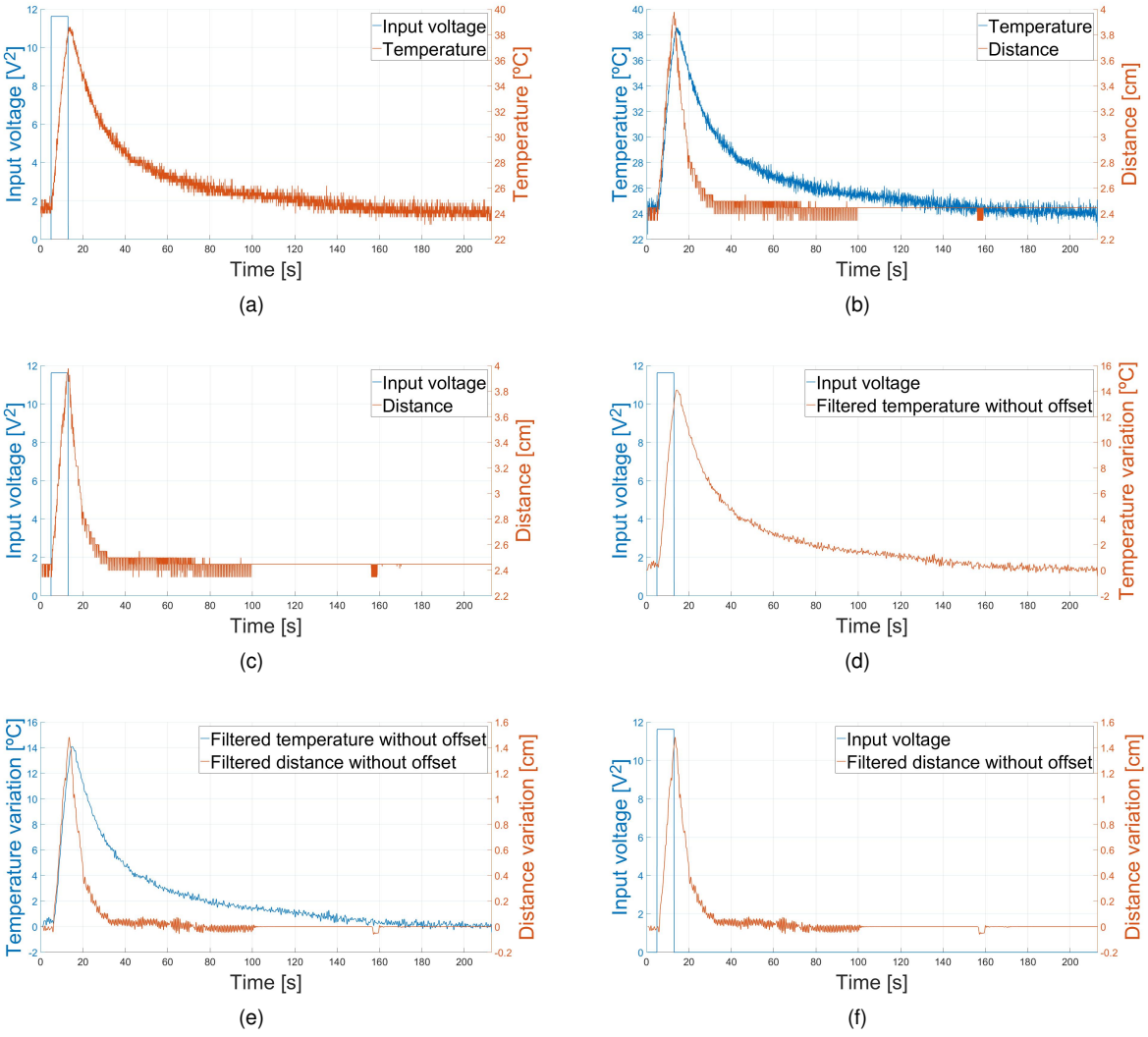

Figure 3.10: Raw data-sets acquired for model identification. (a) TE model (T_s = 0.0521 s), (b) TM model (T_s = 0.0611 s), (c) Plant model (T_s = 0.0611 s). Processed data-sets acquired for model identification. (d) TE model, (e) TM model, (f) Plant model.

3.3.4 System identification

This stage will help characterizing, mathematically, the system (an AAA) through the data of a single SCP actuator (code nr. 2). This is key to perform the simulations (as one will see in 4.3.1).

The identification uses the plant's model, since it displays the relation between voltage and displacement (the control goal). The displacement is a positive value for the actuator's contraction, relative to its initial length. It is possible to rewrite the plant's transfer function (3.6) in a compact version (3.14). Thus, after identification, one can set relations between the identified coefficients and the parameters of the plant model using (3.15).

$$\frac{X}{V^2} = \frac{b_0}{s^3 + a_2 s^2 + a_1 s + a_0}, \tag{3.14}$$

where

$$a_2 = \frac{\beta}{m} + \frac{\lambda}{C_{th}}, \quad a_1 = \frac{k}{m} + \frac{\lambda\beta}{C_{th}m}, \quad a_0 = \frac{\lambda k}{C_{th}m} \quad \text{and} \quad b_0 = \frac{C}{C_{th}mR}. \tag{3.15}$$

MATLAB's system identification toolbox performed the identification. The procedure was to import the plant's model input and output signals (as time domain data), followed by setting the transfer function with no zeros and with 3 poles, as derived in (3.14), while using the continuous-time option and the initialization method set to the instrument variable approach. The results of the identification process are in Table 3.5 and Figure 3.11, and confirm the identified model's accuracy: the NRMSE value was $\approx$ 90 % and the RMSE was close to zero, which are good values to perform simulations, and to conduct future tests upon the real system, i.e., the AAA (see Appendix C.3 for the performance metrics' expressions). The remaining actuators (nrs. 1, 3, 4, 5 and 6) followed equivalent steps and, in average, the NRMSE value was $\approx$ 80 %, which is slightly lower due to the quality of some data-sets (even after processing), in relation to the one obtained for the actuator in question. Table 3.6 displays a comparison with other works' identified models performance, through which one can conclude that the fitness value of this work is reasonable and similar to other works that employed simple and similar linear modeling strategies.

Table 3.5: System identification: plant's model coefficients and goodness of fit.

Model coefficient values				**RMSE**	**NRMSE**
$a_0 = 0.1909$	$a_1 = 1.2661$	$a_2 = 1.5053$	$b_0 = 0.02995$	0.0227	90.3630 %

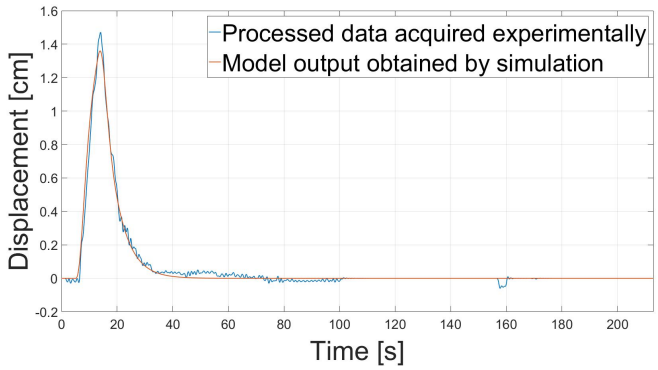

Figure 3.11: Identification results, from the plant's model.

Table 3.6: System identification: goodness of fit, from other works' identified models.

Identified model: output/input[a]	**Performance metric**	**Results**	**Modeling strategy**
Force (N)/power (W) [28]	NA	89.0 %	Linear model
Force(mN)/Voltage(V) [35]	Cross-evaluation	90.0 %	
Displacement (%)/voltage (V) [5]	NRMSE	90.82 %	Linear (grey-box modeling)
Displacement (%)/force (N) [32]		91.33 %	
Displacement (%)/voltage (V) [32]		86.74 %	
Displacement (mm)/voltage (V) [33]		89.25 %	
Displacement (mm)/voltage (V)[34] [b]	NRMSE	85.17 %	Linear (black-box modeling)
Displacement (mm)/voltage (V) [30] [c]	NRMSE	99.07 %	Nonlinear model (based on the energy)
Temperature (°C)/voltage (V) [30] [c]		99.87 %	
Displacement (mm)/voltage (V) [31] [d]	NA	99.05 %	
Temperature (°C)/voltage (V) [31] [d]		99.67 %	
Displacement (mm)/voltage(V) [38] [e]	Maximum error	20.40 %	Linear model (to capture hysteresis)
	RMS	6.90 %	
Displacement (mm)/voltage (V) [39] [f]	Average error	14.10 %	
	Standard deviation	9.90 %	

NA stands for "not available", meaning that the work did not provide the value. [a] Obtained from single actuators. [b] Results for the "standing air" experiment. [c,d] Results for the proposed nonlinear model and "Shieldex thread" (auto coiled). [e] Results for the "augmented linear model". [f] Voltage used as a temperature surrogate. Results for a SMA actuator for the linear model.

3.3.5 Approximations and limitations

The work relied on simplifications about the actuators and the acquired data. Together with the setup and material limitations, drifts between the real behavior and the model's output can arise. This list outlines the main sources of errors (besides the inability to capture directly the AAA's angle).

Source of errors from material limitations:

• The measured temperature is not the real one (one cannot exactly measure the actuator's internal temperature): the actuator loses a percentage of the resistive wire's heat to the air by convection, and just absorbs the remaining by conduction. Therefore, the temperature's direct measurement is not the most accurate method, since a uniform contact between the sensor and the actuator is hard to set.

• The work did not acquire the voltage, to identify the TE and plant models, by sensors - it considered the voltage equal to the desired input signal. The sonars' acquisitions were not the most accurate too.

• The Arduino is not the most suitable board to perform data acquisition tasks (a DAQ system would be better). Nevertheless, it was able to acquire the required data and perform the essential control-based operations; plus, it is light weight and has small dimensions, which is an advantage for this application.

• Only some of the model's parameters were possible to measure directly with instruments. The remaining parameters estimation was indirect, by the acquired data, or by the identified model.

Source of errors from approximations:

• Two actuators with the same specs are not exactly equal, since their fabrication was by hand, and some differences between each other exist, which can introduce slight discrepancies in their parameters.

• The voltage control applied to the SCP actuators was via PWM, however, to simplify some stages, the work handled the PWM values as average voltage potentials.

• The copper's resistance was constant, despite the fact that it varies slightly with temperature. Moreover, the work also ignored the change in resistance due to other factors, since it was not representative ([2] found a weak correlation between resistance and both strain and force changes - for a silver-coated nylon muscle - and [36] found that the change in nickel's resistance caused by temperature was 40 times bigger than the change caused by the deformation of the actuator).

• The TM model followed a simple linear mass-spring-damper model. However, not considering the helical geometry (which affects the displacement) and the inductance (due to the coiled geometry of the resistive wire) but also, individual material properties like the coefficient of thermal expansion and modulus of elasticity, unlike [29], can lead to a less accurate model.

• The work did not consider hysteresis, since the adopted actuators' association overcomes its effect, neither degradation in performance (which may affect the strain and angle variation) after several cycles.

3.4 Control strategy

This section will chose a suitable controller design, according to the system's characteristics. The verification analysis (simulations), regarding the implementation, is in subsection 4.4.3.

The work did not consider open-loop control strategies (inverse compensation) because they would not correct external disturbances and because of 2.4.4 conclusions - it benefited feedback strategies. As mentioned in chapter 2, there are countless ways and variables to control SCP actuators (voltage, temperature, displacement, force, angle), but it was not possible to use the potentiometer to acquire the AAA's angle. Thermistors and sonars were not suitable to employ directly in the AAA to control the angle or the displacement, either. So, the simulations estimated the angle by approximating the AAA's dynamics via each actuator's displacement. However, for the real system, the controller followed an open loop strategy, since one could not get around the problem to implement a feedback strategy.

3.4.1 Controller design

The AAA comprises two SCP actuators in parallel, and its goal is to adjust the pulley's angle according to a reference. Thus, the designed solution employed a parallel association as well, since two controllers would be necessary to control each one of the actuators, depending on the situation. Despite not using the model for the two SCP actuators' association (3.11), an approximation with the model for a single actuator (3.6) was in place. The AAA's angle variation corresponded to the difference between displacements of the actuators. Therefore, after the actuators models, there was a block to convert linear to angular motion, knowing the pulley's radius r_p was 15 mm (Figure 3.12).

The architecture was a PID controller with a filtered derivative (FD) and with a clamping integrator anti-windup (AW) method (Figure 3.12 (a)) implemented as (3.16). This strategy was easy to implement (even on the Arduino) and obtained good tracking results with simulations. The FD (low pass filter in

series with the derivative term) attenuated the high frequency noise and ensured that the derivative was possible to implement with an integral. The clamping method turns the integrator off when the system does not require integration anymore, and its implementation is as a conditional switch - the integrator term shuts down under output saturation and when the error has the same sign of the controller output (3.17). The control scheme also includes a saturation block with lower and upper limits of 0 V and 3.7^2 V (3.18). The upper limit value choice was because the battery supplies it easily (it is the maximum value) and because it was a safe value to prevent the AAA's actuators from melting during the actuation times used (tests in 4). The simulations used a built-in PID block available on Simulink with FD and AW, also considering:

$$u_c(t) = K_p e(t) + K_i \int e(t) clamp(t) dt + K_d \left(\frac{de(t)}{dt} | Lowpass filter \right) \tag{3.16}$$

$$clamp(t) = \begin{cases} 0, & u_c(t) \neq u(t) \wedge e(t)u_c(t) > 0 \\ 1, & otherwise \end{cases} \tag{3.17}$$

and

$$u(t) = \begin{cases} 0, & u_c(t) < 0 \\ u_c(t), & 0 \leq u_c(t) \leq 3.7^2 \\ 3.7^2, & u_c(t) > 3.7^2 \end{cases} \tag{3.18}$$

where $u_c(t)$ is the PID command, $u(t)$ is the saturation block output command (both are voltages) and K_p, K_i and K_d are the proportional, integral and derivative gains, respectively; $e(t)$ is the error between the system's output and the reference angle, and $clamp(t)$ is the condition to turn the integral off or not.

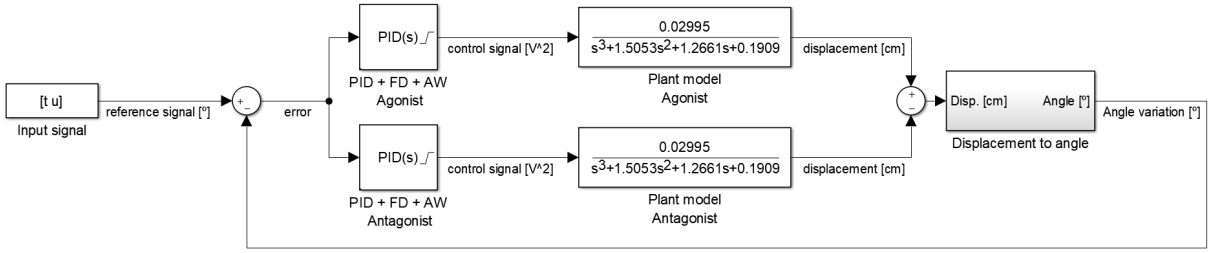

(a)

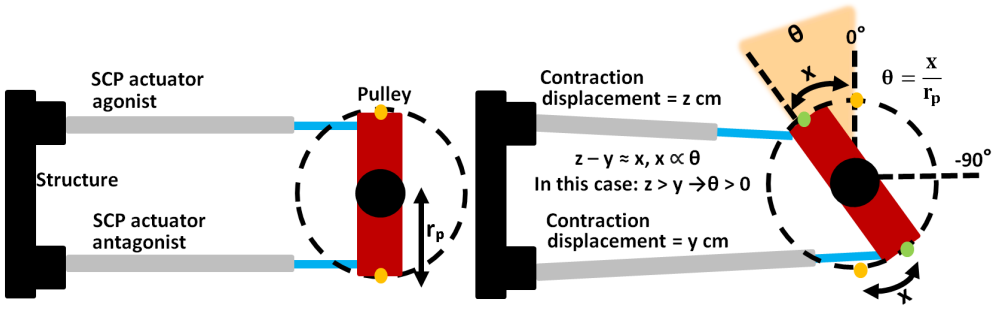

(b)

Figure 3.12: Control architecture. (a) Simulink block diagram, (b) Geometry to estimate the AAA's angle.

The Simulink's PID tuner app tuned the PID controller gains. An arrangement with one controller allowed each controllers' tuning individually. The reference was a sine wave (15 °of amplitude) for the

agonist PID controller, since it was a representative signal with a reasonable amplitude. The procedure was to set the PID output to zero, when the reference derivative was negative (the antagonist covers those cases), otherwise, the output did not change. The gains' tuning ensured the final response covered a rise time of $\approx$ 2 s, a settling time of $\approx$ 13 s and an overshoot of $\approx$ 6 %. The procedure for the antagonist PID controller was equivalent and obtained similar values, after imposing the same requirements; but, the gains adopted opposite values, to complement both controllers' action and avoid the outcome to be zero degrees. Table 3.7 shows the controllers' parameters. The last step was to join the PID controllers with the plant models, as Figure 3.12 (a), and test them with several references.

Table 3.7: Controller design: controller's parameters.

Controller parameters	Proportional gain (K_p)	Integral gain (K_i)	Derivative gain (K_d)	Filter coefficient (N)	Saturation upper limit	Saturation lower limit
Agonist	0.50	0.12	0.47	5.84	3.7^2	0
Antagonist	-0.50	-0.12	-0.47	5.84	3.7^2	0

Final considerations: control architecture

As described in 3.2.1, the AAA's working principle is as follows: when one actuator contracts, the other one expands (and the pulley turns), but also resists to that contraction. As pointed out in previous sections, the model and control employed for the simulations will not describe, accurately, the AAA's real behavior, due to setup limitations. Figure 3.12 (a) describes the AAA's behavior (angular variation) in the simulations. The presented control scheme used the model for two individual SCP actuators, and computed the AAA's angle via the contraction difference between the actuators (the controllers' voltage commands induce the contractions) [1]. The adopted approach is simplified, since it did not account that when voltages act upon one AAA's actuator, to make it contract, there is an opposing force, to this contraction motion, from the other AAA's actuator. This also means that, for the same voltages, the contractions of the AAA's actuators (and hence their contraction difference), should not be as high as the contractions of individual and equivalent SCP actuators. The mentioned inability is what makes the method used in simulations drift from the real system performance, i.e., the AAA.

The control scheme in Figure 3.12 (a) works considering that each controller will actuate according to the direction of the reference signal: for example, to track a sine wave, in the beginning, the controller of the upper segment, will generate voltages and supply them to the actuator (for its contraction); later, when the reference shifts direction, the controller of the lower segment starts supplying the associated actuator. The "agonist" and "antagonist" muscles are deemed equal, but they are actuated in phase opposition (when one expands the other contracts). This behavior will generate a balance between contractions of the two actuators over time, and hence, a corresponding angle variation in the AAA. Note that, when one actuator is being excited the most by the controller, due to the reference direction, does not mean that the other actuator is not being excited by its controller: one verified that the actuator

[1] Note that the input of the actuators' transfer function is always positive, due to the saturation block in the PID.

that does not affect the pulley's motion, can still show low contractions (low voltages), which do not impact, greatly, the tracking (see Figure 4.13 (b)).

It is also important to clarify that the controller and actuator of the upper segment of the block diagram in Figure 3.12 (a), also work as the ”antagonist”; the same is valid for the lower segment, which can display the ”agonist” behavior. It depends on the reference signal shape: in one moment, one of the actuators can be contracting strongly (behaving as an agonist), and later, it can be contracting a little bit, or even display no contraction (antagonist behavior). The classification in Figure 3.12 (a) of ”agonist” and ”antagonist” was mainly to distinguish the controllers' gains to assign to each segment (see Table 3.7). Note that both controllers' gains remain unchanged over time, regardless the reference direction.

3.4.2 Alternative design strategies

The work did not consider state space-based solutions, neither seek optimal control strategies, because they did not suit well the application's architecture, would be harder to implement (on the Arduino) and because such strategies would not be mandatory to conclude about the AAA's performance. In contrast, it tested solutions with transfer function-based models, following the same requirements as before (same output limitation, PID scheme and gains).

An alternative used the reference signal's derivative, as a metric to choose which actuator to activate. Positive derivative values enabled the agonist PID controller output, whereas negative values (i.e., when the angle changes its variation direction) enabled the antagonist PID controller output and set to zero the agonist PID controller output (no voltage fed to the agonist). This is hard to implement because it requires computing the derivative beforehand; plus, the tracking was not as smooth and accurate as the one in the adopted solution. Removing the output saturation limit (and the AW method) led to better results, which is not ideal to do in real systems. As an advantage, only one actuator was active at a time (unlike the adopted strategy), which is good energetically.

The work also tried a simple linear parameter varying (LPV) strategy, which scheduled the PID gains. The goal was to set the agonist PID gains to zero, if the reference derivative was negative, and to use the tuned PID gains, otherwise. The working principle for the antagonist was the opposite. This strategy had similar drawbacks (derivative computation), but slightly worse tracking results emerged. Again, removing the output limitation led to better results, but there was no energetic advantage, since the requested power was constant, holding the last value, when the angle variation changed its direction.

Finally, the work assessed the performance of adding 2 feedforward controllers to the adopted solution. The plant's inverse model computation involved a series arrangement with a low pass filter, since it was a non-proper transfer function. The results, for the tested signals, displayed no visible differences from the adopted strategy.

Chapter 4

Results and discussion

This chapter presents the results about the most conclusive experiments and simulations. MATLAB programs that read and process the data from the serial port (which the Arduino connects to) acquired digitally the data. See Appendix A for the circuits and codes.

4.1 Material properties

This section will showcase all the relevant results and conclusions about the properties of the materials used to manufacture the SCP actuators.

4.1.1 Durability tests

These experiments tried to assess the durability of the actuators' fabrication material, by identifying temperature-time and voltage-weight relations that would melt and break (or extend in a non-reversible way) the actuator. This helps setting limits of operation, regarding voltage (training stage) and temperature (annealing stage). Therefore, all the experiments tried to emulate the harshest conditions.

The first experiment took place after the twisting and coiling stage. The oven heated the resulting actuators (1 ply configuration), which employed the same frame of Figure 3.2 (d), with elongations around 112 %. Then, the actuators experienced several trials to identify the time-temperature relation that would damage them. Table 4.1 presents the results, and sets a basis for the annealing stage specifications. Hence, it is fair to compare them with other works' annealing temperatures (Table 4.2). This analysis only considered the mono-filament fishing line actuators (mandrel and auto coiled).

The results comparison has to be cautious, since the annealing methods have different specs in the literature (the works use different elongations and times, according to the fiber's diameter). Still, for the 0.33 mm diameter fibers, there is a clear difference about the temperature (the time is similar): at 165 °C the actuator melted (Table 4.1) and at 180 °C was able to carry out a successful annealing stage (Table 4.2). Comparing 0.45 mm with 0.50 mm fibers (closest value in Table 4.2), one can conclude that [36] and [16] used more resistant fibers: 165 °C for 12 minutes melted the actuator, while 180 °C for 30 minutes resulted in functional actuators. So, the durability of the fibers' material used in this dissertation

Table 4.1: Durability tests: oven's temperature and time relation to damage the actuators.

Actuator fiber	**Temperature (°C)**[a]				
diameter (mm)	**100**	**115**	**135**	**150**	**165**
0.23	ND	ND	ND	SD	M
0.33	ND	ND	ND	ND	M
0.45	ND	ND	ND	ND	M

[a] All the trials lasted 17 minutes (5 minutes to preheat the oven). ND stands for "not damaged", meaning that the actuators did not display any damage after the experiment. SD stands for "slightly damage", meaning that there was a change in color to brown and the coils became glued to each other. M stands for "melted", meaning that the actuators melted.

Table 4.2: Durability tests: annealing's temperature and time relation comparison from other works.

Actuator fiber diameter (mm)								
NA [42]	**0.33** [37]	**0.34** [23]	**0.50** [36]	**0.50** [16]	**0.533** [6]	**0.80** [16]	**0.86** [24]	**0.91** [30]
170 °C, 40 min	180 °C, 15 min	>150 °C, 30 min	180 °C, 30 min	180 °C, 30 min	<80 °C, >95 min	180 °C, 30 min	180 °C, 2 h	180 °C, 1 h

NA stands for "not available", meaning that in the corresponding referenced work the authors did not provide the value.

was lower in comparison to other mono-filament actuators in Table 4.2. Additionally, it is clear that the 0.23 mm fiber is the less durable, and that, between 150 °C and 165 °C, both 0.33 mm and 0.45 mm fibers, change color to brown and their coils become glued to each other due to an excessive annealing, following the results for the 0.23 mm fiber in Table 4.1.

The second experiment assessed the voltage and weight (force) relation of an actuator, without breaking or creating an irreversible elongation. The method was to heat the actuator progressively via voltage increments. The goal was to set a voltage range to use in the training stage. The test employed two times heavier and five times heavier weights, than the twist and coiling weights, for the 1 ply and 2 ply configurations, respectively. The temperature measurement was with a thermistor (Figure 4.1) and the results (for the actuators with nrs. 10, 11, 12 and 13, 14, 15) are in Figures 4.2 (a) and (b).

The results showed that no actuator broke. In Figures 4.2 (a) and (b), the temperature has a significant drop because of the thermistor position adjustment, due to the elongation. The 1 ply actuators with 0.23 and 0.33 mm diameter experienced non reversible elongations, whereas only the 2 ply actuator with 0.45 mm did not sustain a non-reversible elongation. The results of the 2 ply actuator with 0.23 mm diameter revealed damage - it was visible the unwinding of some coils, due to the weight's tension. Table 4.3 lists the elongations after the experiment. One can conclude that there is no clear relation between the elongation, diameter and weight, over voltage increments, for the two actuators' types. This means that each actuator has different degrees of sensitivity, regarding stiffness (configuration), weight and voltage, i.e., each one has its optimal safe range of operation. However, the largest levels of elongation started when supplying higher voltage values: the actuator nr. 10 with 3.26 V elongated considerably. From this value, it was possible to draw suitable training voltage values, for the remaining actuators without damaging them, that were close to the maximum feasible limit. Again, note that the larger elongations show that the real temperatures were higher and closer to the actuator's melting point.

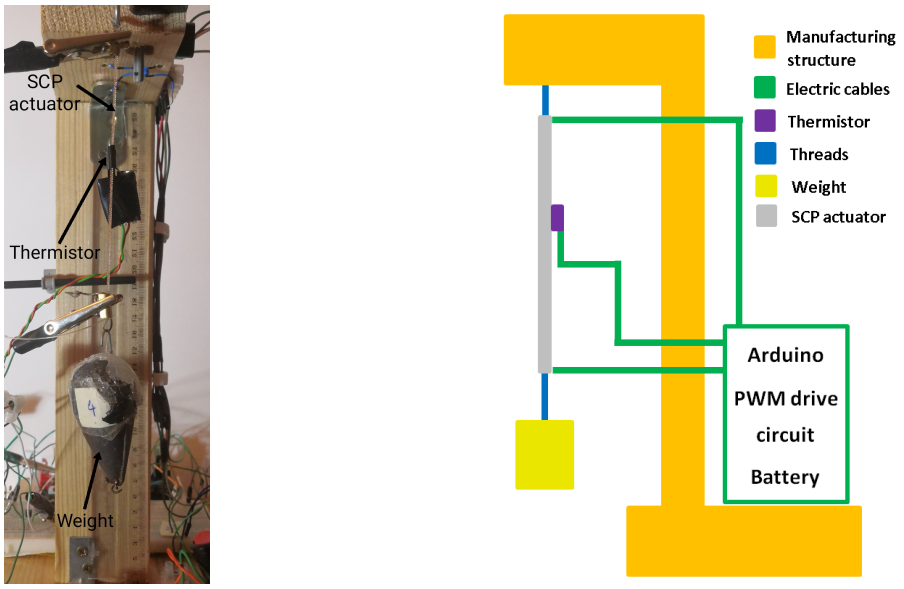

(a) (b)

Figure 4.1: Durability tests: (a) Experimental setup, (b) Diagram.

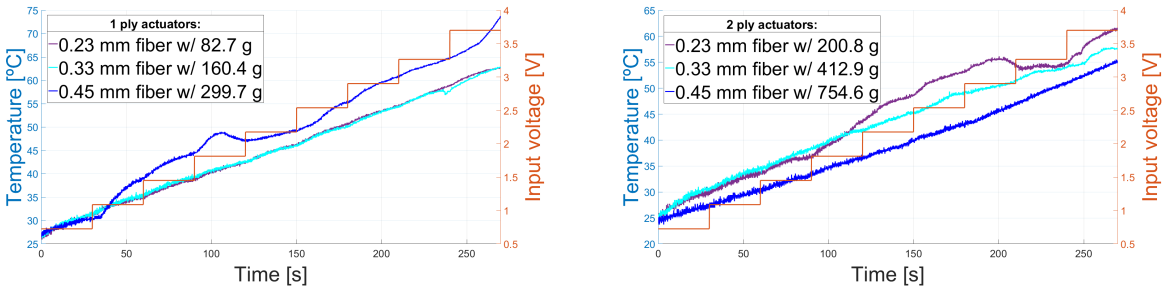

(a) (b)

Figure 4.2: Durability tests: relation between temperature and weight capability with fibers of different diameters (a) for 1 ply actuators, (b) for 2 ply actuators.

Table 4.3: Durability tests: elongations sustained by each actuator.

	1 ply configuration			2 ply configuration		
SCP actuator code	**10**	**11**	**12**	**13**	**14**	**15**
Diameter (mm) - weight (g)	0.23 - 82.7	0.33 - 160.4	0.45 - 299.7	0.23 - 200.8	0.33 - 412.9	0.45 - 754.6
Elongation	173.3 %	133.3 %	113.3 %	134.7 %	166.7 %	122.7 %

4.1.2 Elasticity tests

The following experiments' goals were to assess the actuators' elasticity properties (displacement and strain) and to understand its relation with voltage, weights and diameter of the fiber. The experiments also assessed the contraction time (faster contractions are preferable). Appendix D.1 contains graphical data to validate Tables 4.4 and 4.5. Figure 3.9 (c) shows the experimental setup (same as in section 3.3.3), and the circuit diagram used to acquire the displacement is available in Appendix A.3.

The first experiment (Table 4.4) measured the displacement, while applying successive voltage increments, with the same weight hung. The second (Table 4.5), supplied a fixed voltage value and used

three different weights, for each actuator. The training weight was the maximum value, for the 1 and 2 ply configurations; the twist and coiling weight was the minimum, for the 1 ply case, whereas for the 2 ply case, the minimum weight was three times the twist and coiling one (smaller weights did not produce displacements). The voltage values choice considered the durability tests, so the experiments employed 3.26 V, 3.41 V and 3.55 V, for each diameter; the actuation times choice considered how long the actuators (with the weight hung) could handle those voltages. The sonars are not the most accurate sensors, as the raw data in Appendix D.1 show; however, the maximum displacements matched measurements performed with a ruler. Tables 4.4 and 4.5 summarize the main results. Table 4.6 displays a comparison analysis, with the literature, including only auto coiled actuators (made of mono or multi-filament fibers).

Table 4.4: Elasticity tests: displacements achieved for varying voltages.

Configuration - diameter (mm) -	**PWM value - Voltage**							
length (cm) - weight (g) - SCP actuator code	**100 – 1.45 V**	**125 – 1.81 V**	**150 – 2.18 V**	**175 – 2.54 V**	**200 – 2.90 V**	**225 – 3.26 V**	**235 – 3.41 V**	**245 – 3.55 V**
1 ply - 0.23 - 7.5 - 82.7 - 16	3.7 mm	4.8 mm	5.8 mm	8.2 mm	9.7 mm	11.4 mm	–	–
1 ply - 0.33 - 7.5 - 160.4 - 2	2.7 mm	4.1 mm	4.8 mm	5.6 mm	6.6 mm	8.7 mm	9.7 mm	–
1 ply - 0.45 - 7.5 - 299.7 - 3	3.6 mm	4.6 mm	6.1 mm	6.6 mm	8.2 mm	9.2 mm	–	10.2 mm
1 ply - 0.23 - 10.5 - 82.7 - 7	5.6 mm	8.2 mm	9.4 mm	12.4 mm	12.8 mm	16.5 mm	–	–
1 ply - 0.33 - 10.5 - 160.4 - 8	3.7 mm	5.8 mm	6.6 mm	8.8 mm	11.7 mm	13.3 mm	14.3 mm	–
1 ply - 0.45 - 10.5 - 299.7 - 9	5.3 mm	5.8 mm	8.2 mm	10.4 mm	12.2 mm	13.3 mm	–	15.8 mm
2 ply - 0.23 - 7.5 - 200.8 - 4	4.3 mm	4.8 mm	6.8 mm	8.2 mm	9.7 mm	10.2 mm	–	–
2 ply - 0.33 - 7.5 - 412.9 - 5	2.6 mm	3.6 mm	4.8 mm	5.1 mm	6.6 mm	7.1 mm	7.7 mm	–
2 ply - 0.45 - 7.5 - 754.6 - 6	2.6 mm	4.1 mm	4.6 mm	5.6 mm	6.3 mm	7.7 mm	–	8.7 mm

Table 4.4 shows that the displacement increases gradually with higher voltages; and Table 4.5 shows that there is no clear relation between the weight and maximum displacements, i.e., it is not possible to set a metric to assess which of the three weights leads to the maximum displacement. Note that, in some trials, the values in Table 4.4 did not match the ones in Table 4.5, for equivalent conditions. For example, the actuator nr. 16 with 82.7 g reached 11.4 mm and 12.8 mm for 3.26 V. Apart from the sonar noisy readings, this is possibly due to the longer experiments in Table 4.4, which applied continuously voltage values to the actuator before reaching the value of 3.26 V. This led to small differences in the elongation, and hence, in the displacement. From the comparison analysis in Table 4.6, the only fair conclusion is that this thesis' displacement values are plausible and belong to a range of admissible values. More detailed relations are hard to draw, since there are several variables to account for (weight, fiber diameter and conductivity), and this work's experimental conditions did not fully match the other works' experimental conditions. As seen in 2.2.4, conductive fibers showed, indeed, slightly lower strains.

4.2 Contraction and expansion

This section describes the AAA built, as a test bench, for the contraction/expansion enhancement problem, and presents the results. The solution can use one or two PWM drive circuits, if it requires

Table 4.5: Elasticity tests: displacements achieved for varying weights.

Configuration - diameter (mm) - length (cm) -	Weights								
PWM value/voltage (V) - SCP actuator code	40.4 g	59.8 g	82.7 g	129.4 g	150.9 g	160.4 g	223.8 g	299.7 g	
1 ply - 0.23 - 7.5 - 225/3.26 - 16	11.8 mm	13.3 mm	12.8 mm	–	–	–	–	–	
1 ply - 0.33 - 7.5 - 235/3.41 - 2	–	–	15.3 mm	13.3 mm	–	9.4 mm	–	–	
1 ply - 0.45 - 7.5 - 245/3.55 - 3	–	–	–	–	13.3 mm	–	13.3 mm	12.2 mm	
1 ply - 0.23 - 10.5 - 225/3.26 - 7	17.3 mm	14.8 mm	14.3 mm	–	–	–	–	–	
1 ply - 0.33 - 10.5 - 235/3.41 - 8	–	–	17.3 mm	16.3 mm	–	16.8 mm	–	–	
1 ply - 0.45 - 10.5 - 245/3.55 - 9	–	–	–	–	15.0 mm	–	16.6 mm	15.5 mm	
Configuration - diameter (mm) - length (cm) -	**Weights**								
PWM value/voltage (V) - SCP actuator code	**123.1 g**	**160.4 g**	**200.8 g**	**251.1 g**	**330.7 g**	**412.9 g**	**456.5 g**	**599.0 g**	**754.6 g**
2 ply - 0.23 - 7.5 - 225/3.26 - 4	9.2 mm	11.2 mm	11.2 mm	–	–	–	–	–	–
2 ply - 0.33 - 7.5 - 235/3.41 - 5	–	–	–	6.6 mm	7.7 mm	8.2 mm	–	–	–
2 ply - 0.45 - 7.5 - 245/3.55 - 6	–	–	–	–	–	–	8.8 mm	8.8 mm	8.3 mm

Table 4.6: Elasticity tests: maximum displacement and strain comparison with other works' results.

	Configuration - conductive fiber - diameter (mm) - length (cm) - weight (g)/force (N)	Maximum displacement (mm)	Strain (%)
Thesis results	1 ply - no - 0.23 - 7.5 - 59.8/0.59	13.3	17.7
	1 ply - no - 0.33 - 7.5 - 82.7/0.81	15.3	20.4
	1 ply - no - 0.45 - 7.5 - 150.9/1.48 and 223.8/2.19	13.3	17.7
	1 ply - no - 0.23 - 10.5 - 40.4/0.40	17.3	16.5
	1 ply - no - 0.33 - 10.5 - 82.7/0.81	17.3	16.5
	1 ply - no - 0.45 - 10.5 - 223.8/2.19	16.6	15.8
	2 ply - no - 0.23 - 7.5 - 160.4/1.57 and 200.8/1.97	11.2	14.9
	2 ply - no - 0.33 - 7.5 - 412.9/4.05	8.2	10.9
	2 ply - no - 0.45 - 7.5 - 456.5/4.47 and 599.0/5.87	8.8	11.7
Literature results	1 ply - no - 0.50 - 5.8 - 300.0/2.94 [16]	7.0	12.1
	1 ply - no - 0.50 - 5.8 - 200.0/1.96 [16]	10.0	17.2
	1 ply - no - 0.80 - 5.3 - 300.0/2.94 [16]	10.0	18.9
	1 ply - no - 0.80 - 5.3 - 200.0/1.96 [16]	7.0	13.2
	1 ply - no - 0.175 - 16.0 - 30.0/0.29 [19]	25.0	15.6
	1 ply - no - 0.34 - 13.1 - 200.0/1.96 [23]	13.0	9.9
	1 ply - no - 0.50 - 10.4 - 200.0/1.96 [36]	11.9	11.4
	1 ply - yes - 0.234 - 10.3 - 268.0/2.63 [22]	8.0	7.8
	1 ply - yes - 0.468 - 7.8 - 632.0/6.19 [22]	8.0	10.3
	1 ply - yes - NA - 10.0 - 50.0/0.49 [32, 34]	10.0	10.0
	1 ply - yes - 0.20 - 15.2 - 30.0/0.29 [29]	4.6	3.0
	2 ply - yes - 0.72 - 10.0 - 50.0/0.49 [10]	10.0	10.0
	2 ply - yes - NA - 34.0 - NA [8]	51.0	15.0
	2 ply - yes - 0.20 - 38.0 - 275.51/2.70 [26]	70.0	18.4
	2 ply - yes - 0.38 - 10.0 - 100.0/0.98 [2]	10.0	10.0

NA stands for "not available", meaning that in the corresponding referenced work the authors did not provide the value.

one or two actuators activated (circuit diagrams in Appendix A.3). The work filmed the tests in 4.2.2 and 4.2.3 to validate them and to obtain better readings from the angle and elapsed time (see Appendix D.5).

4.2.1 Engineered AAA solution

As one could not use the potentiometer to acquire the angle variation, a card board with angle marks, fixed to the AAA's structure, executed that task. The AAA's design took into account the final goal, so two PWM drive circuits (to handle each actuator's contraction) and a pulley (able to turn as a result of the contractions) were employed. The structure is adjustable to the actuators' length, which is important to set suitable levels of tension, and has 1 DOF (Figure 4.3).

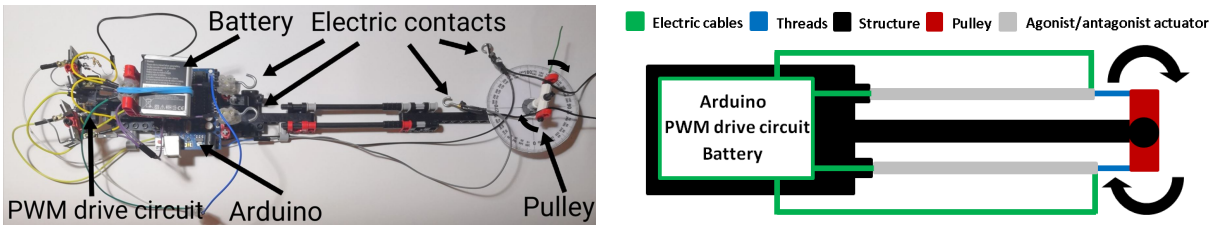

(a) (b)

Figure 4.3: Contraction and expansion: (a) Engineered AAA solution, (b) Diagram.

Moreover, the final design had to fulfill an extra requirement: the circuit components had to handle currents around 4.1 A (considering an actuator resistance of 0.9 Ω and 3.7 V). The choice of the suitable MOSFET assessed if it could dissipate the heat without getting damaged, as follows:

$$P_{Lost} = R_{DS(on)_{|V_{GS}=4.5V}} I^2 = 4.5 \times 10^{-3} \times 4.1^2 = 0.076\ W, \tag{4.1}$$

$$T_{Total} = R_{\theta JA} P_{Lost} + T_{amb} = 62 \times 0.076 + 25 = 29.7\ ^{\circ}C \tag{4.2}$$

where P_{Lost} is the thermal power generated in the MOSFET (W), $R_{DS(on)}$ is the MOSFET's static drain-to-source on resistance (Ω), I is the electric current (A), T_{Total} is the maximum temperature the MOSFET will heat (°C), $R_{\theta JA}$ is the MOSFET's thermal resistance (junction-to-ambient) (°C/W) and T_{amb} is the ambient temperature (°C). Logic-level MOSFETs would be better, but they were expensive, and the employed MOSFET fulfilled the requirements and performed well. The diode had to withstand currents up to 10 A (to ensure a safe margin of operation to deal with less resistive actuators) and it was of the dual common cathode type (the only one suitable available). Table 4.7 lists the AAA's main characteristics.

In addition, Table 4.8 presents an energetic efficiency analysis to set a comparison, between other works and this one, about how long an equivalent battery (to the one used in this work) would last, while supplying a single SCP actuator. The analysis displayed approximations to compute the average theoretical battery duration: it assumed that supplying voltage continuously to reach maximum displacements would not damage the actuators; ignored that some actuators would need higher voltages than 3.7 V - the focus was on the electric current required and on the battery's capacity; and only considered auto coiled actuators - covering different methods and configurations. The findings in Table 4.8 show

Table 4.7: Engineered solution: AAA main specifications.

AAA main specifications	
Single actuator average price (€)[a]	$\approx$ 0.2
Battery specs / price (€)	3.7 Wh (3.7 V, 1000 mAh) / $\approx$ 8.5
Battery duration (minutes)	$\approx$ 15[b] / $\approx$ 20[c]
Arduino Uno R3 price (€)	$\approx$ 20
Mosfet (IRL7833PBF) specs / price (€)	N channel, 30 V, 150 A / 1.78$\times$2
Diode (GP1007) specs / price (€)	10 A, 1 kV / 0.74$\times$2
Pulley radius (mm)	15
Approx. dimensions (cm$\times$cm$\times$cm) / weight (g)	40$\times$7$\times$7 / 203.1

[a] Cost of a 0.1 mm enameled copper wire spool, terminal blocks and nylon mono-filament fiber. [b] Worst case scenario: supplying continuously 4.1 A to a single actuator. [3] Considering that a 1.1 Ω actuator requires 10 W to be properly excited.

Table 4.8: Engineered solution: energetic efficiency comparison.

Conductive fiber - config. - diam. (mm) - resistance (Ω) - wire - SCP actuator code/reference	**Voltage (V) - current (A) - Power (W)**	**Maximum displacement (mm)/ time (s) relation - load (g)**	**Energy to reach maximum displacement (J)**	**Average battery duration (min - s)**	**Nr. of maximum displacement repetitions**
No - 1 ply - 0.23 - 0.96 - copper - 16	3.26 V - 3.40 A - 11.10 W	13.3/5 - 59.8	55.50	18 - 1080	216
No - 1 ply - 0.33 - 1.07 - copper - 2	3.41 V - 3.19 A - 10.87 W	15.3/8 - 82.7	86.96	19 - 1140	142
No - 1 ply - 0.45 - 1.30 - copper - 3	3.55 V - 2.73 A - 9.72 W	13.3/10 - 223.8	97.20	22 - 1320	132
No - 1 ply - 0.50 - 2.02 - copper - [16]	12.0 V - 5.94 A - 71.28 W	10.0/0.625 - 200.0	44.55	10 - 600	960
No - 1 ply - 0.34 - 1.14 - copper - [23]	1.48 V - 1.30 A - 1.93 W	13.0/40 - 200.0	77.20	46 - 2760	69
No - 1 ply - 0.50 - 1.26 - nickel - [36]	0.79 V - 0.63 A - 0.50 W	8.5[a]/65 - 200.0	32.50	95 - 5700	87
No - 1 ply - 0.77 - 19.1 - nichrome[b] - [15]	4.58 V - 0.24 A - 1.1 W	NA/120 - 204.08	132.0	250 - 15000	125
Yes - 1 ply - 0.20 - 14.0 - none - [29]	3.78 V - 0.27 A - 1.02 W	4.6/25 - 30.0	25.50	222 - 13320	532
No - 2 ply - 0.23 - 0.96 - copper - 4	3.26 V - 3.40 A - 11.10 W	11.2/5 - 200.8	55.50	18 - 1080	216
No - 2 ply - 0.33 - 1.09 - copper - 5	3.41 V - 3.13 A - 10.67 W	8.2/8 - 412.9	85.36	19 - 1140	142
No - 2 ply - 0.45 - 1.33 - copper - 6	3.55 V - 2.67 A - 9.50 W	8.8/15 - 599.0	142.50	22 - 1320	88
Yes - 2 ply - NA - 4.0 - none - [8]	5.0 V - 1.25 A - 6.25 W	8.0[c]/10 - 50.0	62.50	48 - 2880	288
Yes - 2 ply - 0.20 - 25.0 - none - [26]	15.0 V - 0.60 A - 9.0 W	40.0[d]/25 - 275.51	225.0	100 - 6000	240
Yes - 2 ply - 0.38 - 25.0 - none - [2]	15.0 V - 0.60 A - 9.0 W	10.0/1 - 100.0	9.0	100 - 6000	6000

NA stands for "not available", meaning that in the corresponding referenced work the authors did not provide the value. [a] Displacement attained by joule heating. [b] Considering the nichrome resistivity equal to $1.1 \times 10^{-6} \Omega \cdot m$ at 20 °C. [c] Displacement attained with the 50 mm long SCP actuator. [d] Displacement obtained for the hand orthosis middle finger's PIP joint value of 25 °.

that, for good energetic efficiency, a trade-off between actuation time, resistance and supplied current is crucial. Longer actuation times will not suit prosthetic-type projects (despite a long-lasting battery), and short times will generally require higher electric currents (or smaller resistances), which can be unsafe. Actuators with smaller electric resistances will heat faster, due to higher currents, whereas actuators with higher resistances (conductive fibers) will need higher voltages to compensate low electric currents. Plus, actuators made of conductive fibers can generally achieve more repetition cycles, probably because of a more efficient heating process, despite the lower electric currents caused by their high resistances. The dissertation's actuators display a fair commitment between time, current and resistance values that make them suitable (they act fast and are safe) to prosthetic-type applications.

4.2.2 AAA with 2 SCP actuators

This test employed equivalent actuators made of 0.23 mm diameter fiber, since these were the fastest actuators to reach the maximum displacement (5 s), and hence, angle variation. Still, the actuation time increased to cover a wider range of angle values, from 5 s (the recommended value at 3.26 V with the tested weights for 1 ply actuators of 0.23 mm diameter fibers) to 10 s, since no damage occurred. The experiments used identical pairs of weights and both actuators' stiffness was 54.49 N/m (computed in subsection 4.3.2). The experiments were also against the gravity to measure angle variations associated to known tensions, i.e. the weights (as Figure 4.4 depicts). The results are in Table 4.9 (see Appendix D.5 for the supporting videos), and Appendix A.3 contains the circuit diagram. Note that, the measured angle does not always achieves the 0 °mark, since the videos correspond to the maximum angle variations, which may have followed a previous trial that did not resume to the initial position.

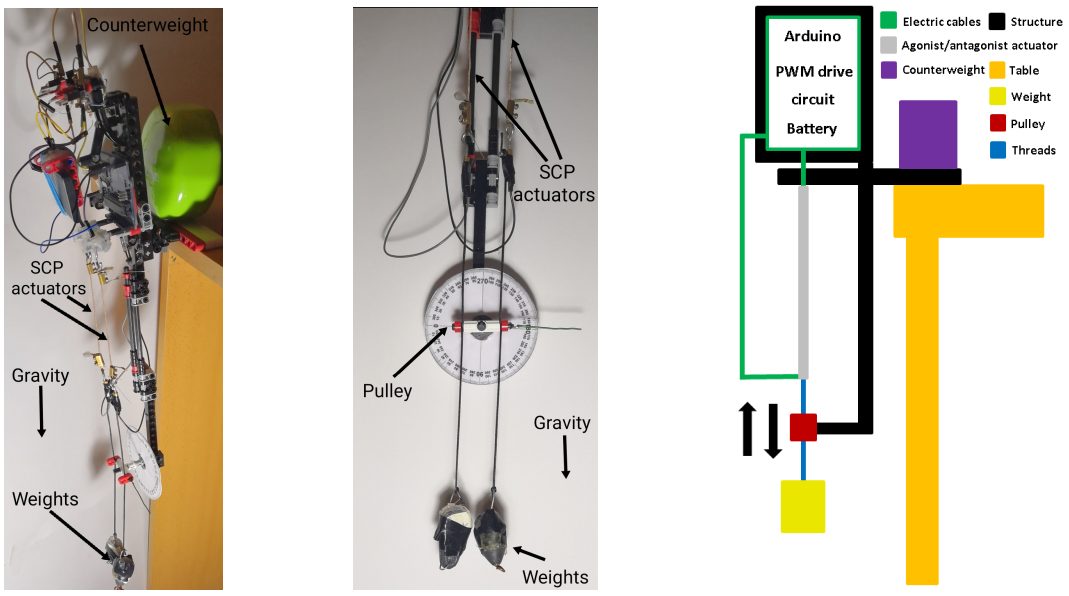

(a) (b) (c)

Figure 4.4: Contraction and expansion: AAA's setup with 2 SCP actuators. (a) Side view, (b) Front view, (c) Diagram.

Table 4.9: AAA with 2 SCP actuators: results.

Agonist nr. - voltage (V) - ON time (s) - weight (g)	Antagonist nr. - voltage (V) - ON time (s) - weight (g)	Max. angle variation (°)	Time to reach max. angle (s)
16 - 3.26 - 5 - 17.8	17 - 3.26 - 5 - 18.3	10	5
16 - 3.26 - 8 - 17.8	17 - 3.26 - 8 - 18.3	17	8
16 - 3.26 - 10 - 17.8	17 - 3.26 - 10 - 18.3	20	10
16 - 3.26 - 5 - 40.0	17 - 3.26 - 5 - 40.4	8	5
16 - 3.26 - 8 - 40.0	17 - 3.26 - 8 - 40.4	13	8
16 - 3.26 - 10 - 40.0	17 - 3.26 - 10 - 40.4	17	10
16 - 3.26 - 5 - 56.4	17 - 3.26 - 5 - 66.3	7	5
16 - 3.26 - 8 - 56.4	17 - 3.26 - 8 - 66.3	12	8
16 - 3.26 - 10 - 56.4	17 - 3.26 - 10 - 66.3	15	10
16 - 3.26 - 5 - 75.9	17 - 3.26 - 5 - 82.7	6	5
16 - 3.26 - 8 - 75.9	17 - 3.26 - 8 - 82.7	9	8
16 - 3.26 - 10 - 75.9	17 - 3.26 - 10 - 82.7	14	10

4.2.3 AAA with a spring and 1 SCP actuator

The setup was similar to the previous experiment (Figure 4.4), but a spring (antagonist) was responsible for the agonist's expansion. The test used different weight pairs to level the angle to 0 °(the stiffness values were different). The angle variations were almost unnoticeable, as Table 4.11 shows. For that reason, the work attempted a new approach: a standard rubber band replaced the spring (Table 4.12). The reasoning was that a less stiff material would not create as much opposing force, as the spring did, during the actuator's contraction, but still, would contract by itself due to the stored force (acquired in the actuator's contraction) after the agonist's contraction. The spring and rubber band specs are in Table 4.10. The circuit is equal to the circuit used along the training stage (see Appendix A.2).

Table 4.10: AAA with 1 SCP actuator: spring and rubber band main specifications.

Spring						Rubber band	
Nr. of coils	Free length	Pitch	Wire diameter	Diameter	Stiffness (k)	Length	Stiffness (k)
31 coils	7.2 cm	$\approx$ 2.3 mm	$\approx$ 0.6 mm	$\approx$ 6.5 mm	165.3 N/m	7.5 cm	38.4 N/m

Table 4.11: AAA with a spring and 1 SCP actuator: results.

Actuator nr. - voltage (V) - ON/OFF time (s) - weight (g)	Spring Stiffness (N/m) - weight (g)	Max. angle variation (°)	Time to reach max. angle (s)	Time to resume to original position (s)
16 - 3.26 - 5/20 - 34.2	165.3 - 40.4	3	5	9
16 - 3.26 - 8/25 - 34.2		8	8	13
16 - 3.26 - 10/30 - 34.2		9	10	14
16 - 3.26 - 5/20 - 40.4	165.3 - 59.8	5	5	9
16 - 3.26 - 8/25 - 40.4		8	8	12
16 - 3.26 - 10/30 - 40.4		10	10	15
16 - 3.26 - 5/20 - 56.2	165.3 - 75.9	2	5	9
16 - 3.26 - 8/25 - 56.2		7	8	14
16 - 3.26 - 10/30 - 56.2		8	10	18

Table 4.12: AAA with a rubber band and 1 SCP actuator: results.

Actuator nr. - voltage (V) - ON/OFF time (s) - weight (g)	Rubber band Stiffness (N/m) - weight (g)	Max. angle variation (°)	Time to reach max. angle (s)	Time to resume to original position (s)
16 - 3.26 - 5/20 - 17.8	38.4 - 9.0	7	5	9
16 - 3.26 - 8/25 - 17.8		10	8	14
16 - 3.26 - 10/30 - 17.8		12	10	14
16 - 3.26 - 5/20 - 40.4	38.4 - 30.5	6	5	9
16 - 3.26 - 8/25 - 40.4		11	8	11
16 - 3.26 - 10/30 - 40.4		12	10	12
16 - 3.26 - 5/20 - 59.8	38.4 - 51.2	5	5	9
16 - 3.26 - 8/25 - 59.8		9	8	14
16 - 3.26 - 10/30 - 59.8		11	10	16
16 - 3.26 - 5/20 - 82.7	38.4 - 75.9	4	5	7
16 - 3.26 - 8/25 - 82.7		8	8	11
16 - 3.26 - 10/30 - 82.7		9	10	13

The collected data was an approximation (obtained with the naked eye), but one can draw valuable conclusions. It is better to work with 2 SCP actuators, since they achieve larger angle variations in shorter periods of time than the spring (which is stiffer than the actuator used as agonist - 165.3 N/m) and rubber band (less stiff - 38.4 N/m). The energetic efficiency is the only drawback of using 2 actuators (the spring and rubber band act passively). However, it is possible to control both the agonist and antagonist actuators, as in the natural muscles, and resume faster to the original position. Apart from this, the rubber band led to slightly higher angle variations, than the spring, as expected, but the time to resume to the initial position did not reveal significant improvements.

4.3 Modeling strategy

This stage will validate the plant's model with different input signals (to assess its performance with the acquired data), and estimate its parameters. The actuator nr. 2 (made of 0.33 mm fiber) will be the one in focus now, because it is less susceptible to break than the ones produced with 0.23 mm fiber and because it is faster (8 s) to attain maximum displacements than the ones made of 0.45 mm fiber (10 s). Plus, its stiffness value is between 38.4 N/m and 165.3 N/m.

4.3.1 Model validation

The process was to test four independent data-sets, in a single actuator, using the plant's transfer function (3.14) to assess its performance: the first was a voltage step, the second a step difference sequence, the third a voltage stair signal (triangle shaped), and the fourth a random signal (Figure 4.5). These data-sets were enough, since they were distinct and included different modes of actuation.

Table 4.13 and Figure 4.5 confirm the validity of the adopted model: NRMSE and RMSE values equal to 100 % and to 0, respectively, describe a perfect fit. The fitness level for the input step suggests high confidence to follow the reference. This is important, since the goal was to model the behavior of the

heating stage, and a voltage step roughly describes it (as seen in 3.3.1). The remaining plant's model outputs also revealed good accuracy to approximate the data with more complex input signals (NRMSE values were higher than 70 %). Therefore, and since the model showed a reasonable performance under more demanding input signals, there is no need to replace it by a more complex model. Although not many of the consulted works provided this kind of data, and despite the different modeling strategies and performance metrics, this dissertation's RMSE values were in the same range of values of other works. The linear model in [39], during verification experiments (for the displacement/voltage hysteresis) with random voltage step inputs, revealed 12.6 % of average error for the displacement tracking of a SMA actuator; and the nonlinear model used in [31], with a sine input, showed RMSE values of $\approx$ 2.7 % and $\approx$ 5.5 %, respectively, for the temperature and displacement tracking of the "Shieldex" actuator.

Table 4.13: Model validation: identified model's goodness of fit with independent data-sets.

Input signals	**RMSE**	**NRMSE**
Step	0.0490	89.2509 %
Step difference sequence	0.0947	71.3209 %
Stair (triangle shaped)	0.0876	71.5860 %
Multilevel random signal	0.0965	71.2103 %

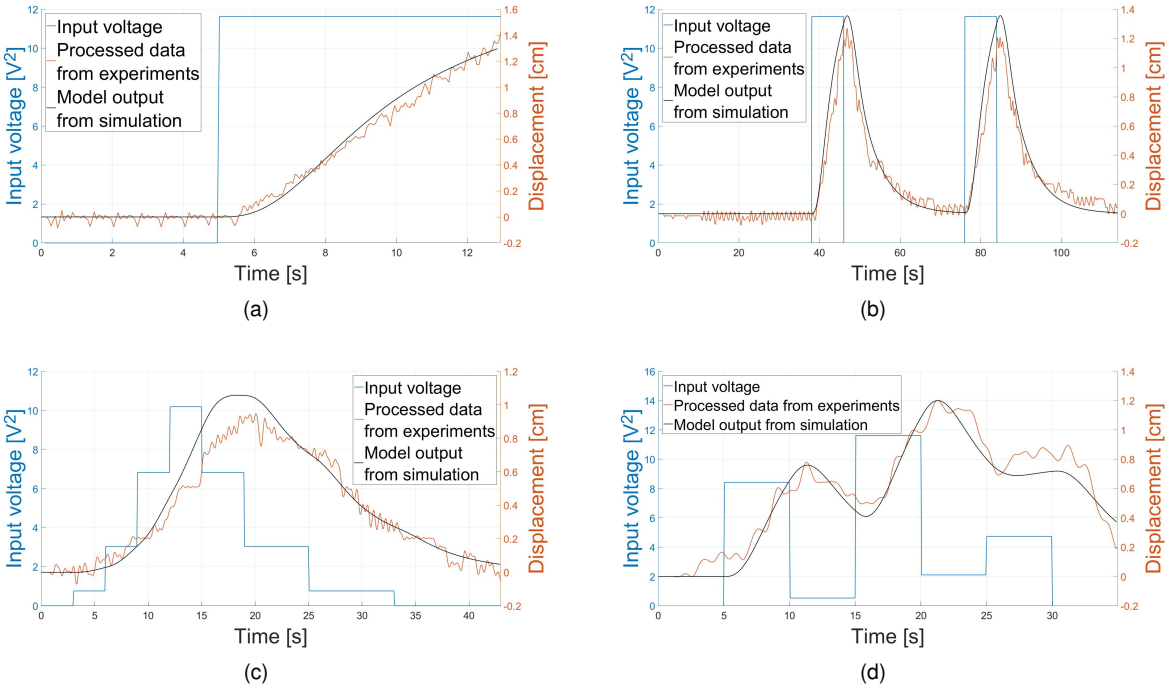

Figure 4.5: Model validation: results. (a) Step, (b) Step difference sequence, (c) Stair (triangle shaped), (d) Multilevel random signal.

4.3.2 Parameters estimation

The TM (k, β, C) and TE parameters (C_{th}, λ, R) estimation was after the identification and validation, and followed two methods. The main experiments comprised the actuator nr. 2, but also computed the

parameters for the other actuators. Appropriate equipment measured some directly, and the acquired data or equation solving (3.15), obtained the remaining, indirectly. The KERN EMB 500-1 precision electronic balance weighed the actuators and pulley, and a ruler measured the radius of the pulley.

The absolute conductivity (λ) and thermal mass (Cth) estimation was with the data acquired for the TE model. Relations between power and temperature, and between energy and temperature (Figures 4.6 (a) and 4.7 (a)) from the collected data (until the step difference resumed to 0 V) computed λ and Cth, respectively (Figures 4.6 (b) and 4.7 (b)). Both parameters estimation considered the temperature to be $\approx$ 38 °C (the highest value across the step difference experiment - see Figure 3.10). The actuator's stiffness (k) computation was through the slope of a linear regression between the displacements caused by the force (weight) applied on the actuator (Figure 4.8). Appendixes D.2, D.3 and D.4 contain the data to compute the absolute thermal conductivity, thermal mass and stiffness for the remaining actuators.

The damping coefficient (β) and proportional temperature to force coefficient (C) were not possible to measure directly, because there was no appropriate equipment. Hence, their derivation was via the identification results - from Table 3.5 and (3.15) - knowing m, R, λ, C_{th} and k, by solving b_0 in order to C; and a_2 and a_1 in order to β, which led to two solutions for β, but one was invalid (it was negative). The estimated parameters were admissible, and consequently, represented good approximations (Table 4.14). Note that, although the initially proposed model (3.11) has the same structure as (3.14) (3 poles and no zeros), one cannot use (3.12) to solve the equations associated to each identification coefficient, since the data-sets manifest different conditions (did not use the AAA with two actuators).

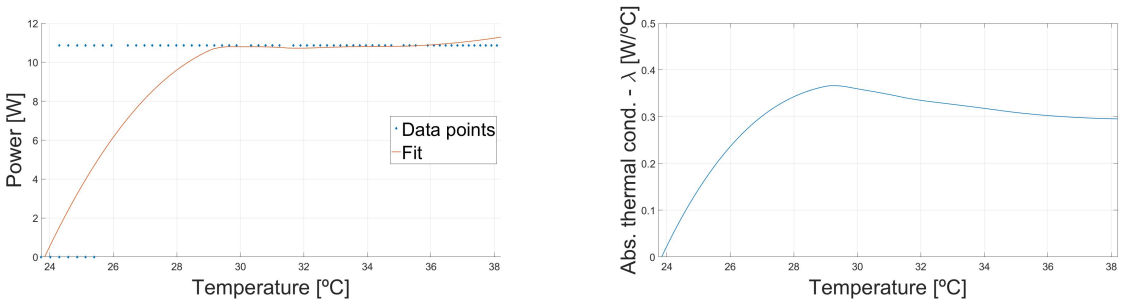

Figure 4.6: Parameters estimation: absolute thermal conductivity computation from actuator nr. 2 data-sets. (a) Power and temperature relation, (b) Absolute thermal conductivity (λ) for different temperatures.

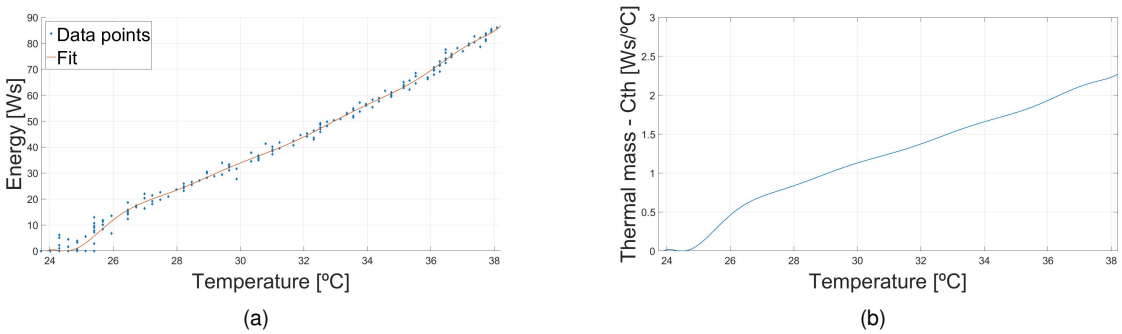

Figure 4.7: Parameters estimation: thermal mass computation from actuator nr. 2 data-sets. (a) Supplied energy and temperature relation, (b) Thermal mass (C_{th}) for different temperatures.

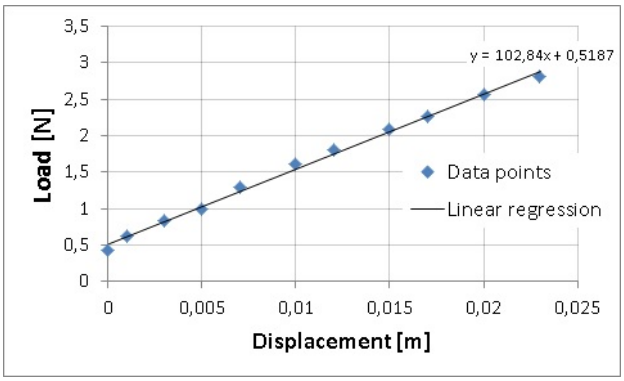

Figure 4.8: Parameters estimation: data acquired to compute the stiffness of the actuator nr. 2.

Table 4.14: Parameters estimation: results from this dissertation and from the literature.

Parameters	**Diameter (mm) - Configuration - conductive fiber - length (cm) - SCP actuator code/reference**					
Dissertation:	0.23 - 1 ply - No - 7.5 - 1	0.33 - 1 ply - No - 7.5 - 2	0.45 - 1 ply - No - 7.5 - 3	0.23 - 2 ply - No - 7.5 - 4	0.33 - 2 ply - No - 7.5 - 5	0.45 - 2 ply - No - 7.5 - 6
m (g)[a]	4.5 + 40.4	4.5 + 82.7	3.4 + 150.9	4.5 + 200.8	4.3 + 412.9	4.5 + 754.6
R (Ω)	0.96	1.07	1.30	0.96	1.09	1.33
C (mN/°C)	1.7	6.4	3.0	10.4	8.9	24.1
β **(Ns/m)**	0.0303	0.1202	0.1044	0.2429	0.2201	0.9322
k (N/m)	54.49	102.84	106.67	61.39	112.2	311.14
λ **(W/°C)**[b]	0.36	0.29	0.32	0.38	0.34	0.29
C_{th} **(Ws/°C)**[b]	1.70	2.25	3.10	1.81	2.72	4.40
Literature:	0.38 - 2 ply - Yes - 10.0 - [2] [c]		0.20 - 1 ply - Yes - 15.0 - [29] [d]		NA - 2 ply - Yes - 11.0 - [40] [e]	
m (g)	100.0		0.10		5.0	
R (Ω)	25.0		14.0		2.5	
C (mN/°C)	2.31 $\pm$ 0.41		NA		NA	
β **(Ns/m)**	0.84$\pm$0.12		NA		NA	
k (N/m)	160$\pm$35		23		NA	
λ **(W/°C)**	0.0094$\pm$0.0017		NA		0.35	
C_{th} **(Ws/°C)**	0.028$\pm$0.0089		0.17		3.92	

NA stands for "not available", meaning that in the referenced work the authors did not provide the value. [a] SCP actuator weight + load weight. [b] Obtained at 31 °C, 38 °C, 30 °C, 29 °C, 30 °C and at 32 °C (from left to right). [c] Obtained experimentally for the "standing air" experiment. [d] Parameters obtained theoretically and employed in the proposed model. C_{th} was obtained indirectly with the provided data, at 23 °C. [e] Parameters obtained experimentally. λ was computed at 25 °C.

The dissertation's results were as expected: the stiffness increases with the fiber's diameter and with 2 ply configurations; the thermal mass increases with the increase in the fiber's diameter and with the copper's resistance - raising the actuator's temperature requires more energy; and the damping coefficient trend is to raise its value with larger loads, but there is no pattern in the associated velocity analysis. Plus, considering the mass-spring-damper system in (3.4) one can conclude with Table 4.14 values that the system is underdamped (0 $\leq$ damping ratio $<$1). The referenced literature lacks works computing the TE and TM parameters, so this work's results comparison focused mainly the parameters obtained in [2], since it was the most detailed work about the topic. The TM parameters (k, β, C)

displayed a good degree of similarity, whereas the TE parameters (C_{th}, λ, R) showed differences: C_{th} and λ were smaller in [2], since the work used less power to raise the actuator's temperature, probably due to a more efficient Joule heating process caused by the higher resistance of conductive fibers (i.e., a resistive wire may be inefficient to heat mono-filament fibers). Different materials, manufacturing techniques (2 ply) and environmental conditions are valid reasons for the disparities too. Overall, the results were satisfactory considering how volatile these parameters are, since every small change or glitch in the experimental conditions, can lead to significant differences.

4.4 Control strategy

This section provides a practical analysis (with closed and open loop control schemes) via simulations and with the AAA, to evaluate the controller. It uses the actuators nr. 18 and 19 (same specs as nr. 2), therefore the model during simulations is the same as in (3.14) with the Table 3.5 coefficients.

4.4.1 Controllability and observability

Firstly, one must verify if the plant's model (3.14) is controllable and observable - how it relates with the actuators and sensors. So, the plant's model transfer function, in the state space representation, is

$$\begin{cases} \dot{x}(t) = Ax(t) + Bu(t) \\ y(t) = Cx(t) + Du(t) \end{cases} \tag{4.3}$$

$$\begin{gathered} x(t) = \begin{bmatrix} \ddot{X}(t) \\ \dot{X}(t) \\ X(t) \end{bmatrix}, \quad u(t) = V^2(t), \\ A = \begin{bmatrix} -1.5053 & -1.2661 & -0.1909 \\ 1.0000 & 0 & 0 \\ 0 & 1.0000 & 0 \end{bmatrix}, \quad B = \begin{bmatrix} 1 \\ 0 \\ 0 \end{bmatrix}, \quad C = \begin{bmatrix} 0 & 0 & 0.0300 \end{bmatrix} \quad \text{and} \quad D = 0. \end{gathered} \tag{4.4}$$

The state variables are the displacement $X(t)$ (spring), velocity $\dot{X}(t)$ (damper) and acceleration $\ddot{X}(t)$ (mass), as in the TM model (3.4); the input variable $u(t)$ is the squared voltage. Since the modeling was relative to the displacement data, just the simulations employed the linear to angular transformation.

The plant is stable since all the eigenvalues of the matrix A have negative real part:

$$eig(A) = \begin{bmatrix} -0.6590 + 0.7649i & -0.6590 - 0.7649i & -0.1873 + 0.0000i \end{bmatrix}^T. \tag{4.5}$$

The continuous state realization

$$\dot{x}(t) = Ax(t) + Bu(t) \tag{4.6}$$

is completely controllable if and only if the controllability matrix

$$C(A,B) = \begin{bmatrix} B| & AB & | & A^2B & | & ... & |A^{n-1}B \end{bmatrix} \tag{4.7}$$

has rank $n = dim\ x$ [45]. Additionally, the continuous system

$$\dot{x}(t) = Ax(t), \quad y(t) = Cx(t) \tag{4.8}$$

is completely observable if and only if the observability matrix

$$O(A,C) = \begin{bmatrix} C \\ CA \\ CA^2 \\ ... \\ CA^{n-1} \end{bmatrix} \tag{4.9}$$

has rank $n = dim\ x$ [45]. Adding the values to (4.7) and (4.9), results in:

$$C_{plant} = \begin{bmatrix} 1.0000 & -1.5053 & 0.9997 \\ 0 & 1.0000 & -1.5053 \\ 0 & 0 & 1.0000 \end{bmatrix}, \quad rank(C_{plant}) = 3 = dim\ x \quad \text{and} \tag{4.10}$$

$$O_{plant} = \begin{bmatrix} 0 & 0 & 0.0300 \\ 0 & 0.0300 & 0 \\ 0.0300 & 0 & 0 \end{bmatrix}, \quad rank(O_{plant}) = 3 = dim\ x, \tag{4.11}$$

which means the space realization is controllable and observable. This is useful because it is possible to design a feedback controller placing the closed-loop eigenvalues anywhere in the complex plane, and because one can know all the states from the system's output using suited sensors in specific locations.

4.4.2 Stability analysis

The work did a simple analysis to verify the stability of the overall control scheme (obtained from (3.16)). Hence, comes:

$$U_c(s) = \left(K_p + K_i \frac{1}{s} + K_d \frac{Ns}{s+N} \right) E(s). \tag{4.12}$$

To simplify, the analysis did not add the AW method, saturation limits and external disturbances. From (4.12) comes,

$$Ctrl_{1,2}(s) = \frac{U_c(s)}{E(s)} = \frac{s^2(K_p + K_dN) + s(K_i + NK_p) + NK_i}{s^2 + sN}, \tag{4.13}$$

which corresponds to both controllers transfer function (agonist and antagonist). Next, the plant's transfer function (3.14), with coefficients from Table 3.5, multiplies a gain to convert displacement (cm) to angle (°) (represented by "$Plant(s)$" in (4.14)) and forms a series association with both controllers' transfer

function, as Figure 3.12 (a) shows. Both products follow a subtraction, since the arrangement is a parallel association, and the result was the system's open loop expression,

$$OL_{AAA}(s) = Ctrl_1(s)Plant(s) - Ctrl_2(s)Plant(s). \tag{4.14}$$

The final step was to close the loop,

$$CL_{AAA}(s) = \frac{OL_{AAA}(s)}{1 + OL_{AAA}(s)}. \tag{4.15}$$

The step response of (4.15) has a settling time of $\approx$ 13 s and 30 % overshoot, due to a fast rise time of 1.17 s. The Bode plot of (4.15) (Figure 4.9 (a)) shows a response close to a low pass filter (0 dB gain at low frequencies) - the system will track signals below the bandwidth frequency (1.76 rad/s or 0.28 Hz); and a sharp drop (60 dB per decade) at high frequencies - which results in a good high frequency noise rejection. The Bode plot of (4.14) helps shaping the closed-loop response, and from Figure 4.9 (b), one can conclude the following: the gain is high ($\approx$ 50 dB) at the lower frequencies - which entails a zero state error; above the crossover frequency, the magnitude drops at a rate of 50 dB per decade - which sets a good noise rejection characteristic. Plus, from the open-loop characteristic in Figure 4.9 (b), one can obtain the gain (10.6 dB) and phase (35.6 °) margins. The latter tells how much lag between the reference and the output the system can withstand, and the former, how much gain the system can use without overcorrecting the angle reference. Good stability margins ensure good performance and protect the results from disturbances and factors that the system's dynamics did not model. The system is marginally stable, since it has a pole at origin, introduced by the controller (4.13) - overall, the closed loop system has 10 poles and 7 zeros. However, the final controller includes saturation limits and an AW method that help preventing indefinite bounded offsets and oscillatory output responses.

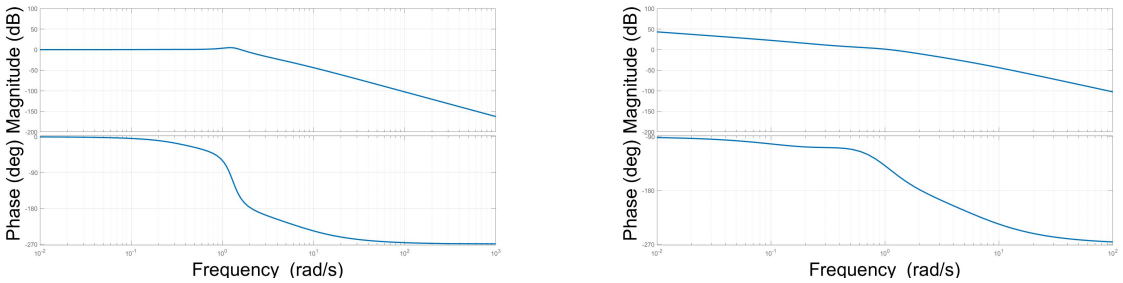

Figure 4.9: Stability analysis: Bode plots. (a) Closed-loop, (b) Open-loop.

As seen in 2.1, muscular contractions can take 1 s to occur. As SCP actuators, muscle contractions reveal lag (latent period) and the relaxation is longer [11]. However, this analysis results did not match the biological muscles action specs: the step response characteristic was not ideal; the bandwidth was small, and, as a result, the system's highest tracking frequency was not fast enough. The work did not focus the optimization of its constraints to obtain faster muscle responses. Nonetheless, it is possible to change the upper limit at which the system's dynamics are controllable. To do that, one added to (4.14)

a 4^{th} order series compensator. The requirement was to follow signals with a period up to 1 s (1 Hz); so, one increased the bandwidth to 5 Hz ($\approx$ 30 rad/s). The compensator tuning was with the Simulink's loop shaping tool of the control system designer app. Figures 4.10 (a) and (b) show the resulting closed-loop bode plot and the angle tracking improvement. However, this analysis did not include saturation limits, hence the improvements were at the expense of extremely high impulse control commands (unfeasible in a real system). Still, the answer for better performance with faster signals to make SCP actuators reliable for prostheses, is to redesign the controller (and eventually use higher, but safe, voltages).

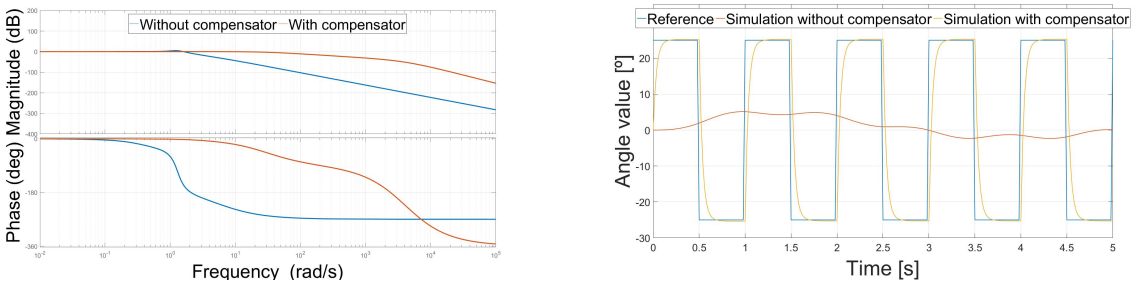

(a) (b)

Figure 4.10: Stability analysis: compensator influence. (a) Closed loop Bode plot, (b) Angle tracking.

4.4.3 Verification: numerical simulations

Several simulations on Simulink tested the control strategy to understand how the AAA would behave with a feedback strategy (scheme in Figure 3.12 (a)). The saturation limit was the maximum value (3.7 V^2), because the method in 4.2.2 displayed no damage when increasing the actuation time, but also because the tested actuators had a bigger diameter (nrs. 18 and 19) - they need higher voltage values to surpass the opposing pulling force of the antagonist to achieve the maximum displacement. The input references had a sampling period of 0.02 s and this stage set the PID controllers to its discrete version.

Operation range

The first series of experiments attempted to find the highest frequency and amplitude that the system could track, without large errors. The procedure was to apply a sinusoidal frequency sweep from 0 to 0.5 Hz with 15 °of amplitude as reference. The results showed that the system could track the reference, with good performance, until 0.10 Hz, which is below the bandwidth frequency (0.28 Hz). So, tests employed sine waves with 0.10 Hz and different amplitudes. Table 4.15 shows the performance associated to each test, and reveals an error rise from values higher than 25 °. Due to the output signal's lag, the RMSE or NRMSE, are not reliable to assess the real performance; therefore, the work used different metrics.

Angle tracking performance

The second set of simulations assessed how the system would track different angle references. The maximum and minimum amplitudes were 25 °and -25 °; the sinusoidal and square waves' frequency

Table 4.15: Verification simulations: performance with 0.10 Hz sinusoidal waves for varying amplitudes.

Amplitude (°)	RMSE	Error between maximum points (°)[a]	Phase difference (°); time difference (s)[b]
15	6.72	-1.54	-33.12; -0.92
20	8.97	-2.05	-33.12; -0.92
25	11.08	-0.55	-36.72; -1.02
30	14.16	2.32	-39.60; -1.10
35	18.50	5.95	-47.52; -1.32

[a] Largest error between the maximum angle values of the reference signal wave and the output signal, for equivalent signal sections. [b] Obtained through time stamps associated to the maximum angle values of both the reference and output signals.

was 0.05 Hz; the multilevel random, stair-shaped and triangle-shaped signals changed values every 20 s; and the sawtooth's frequency was 0.02 Hz, since sharp angle variations are harder to follow. Figure 4.11 shows the tracking results, and Table 4.16 the associated performances. Table 4.17 gathers other works' results obtained from experimental measurements, instead of simulations, as in this work.

The results validated the methods used, since the output followed, reasonably, several angle references (Figure 4.11). The only downside was the output lag resulting from the actuator's heating process. So, Table 4.16 showed slightly worse results than desired: the square wave performance was not as high as expected - reducing the frequency (0.025 Hz) can improve it (RMSE = 14.51, MAE = 6.53); and the sawtooth's maximum error was excessively high, even with lower frequencies, due to its sharp variations. Although the literature presents different control strategies and metrics, the range of values exhibited by the works that tracked the angle, was similar. The experimental results in [37] showed small errors for a sinusoidal wave with 9 °(only covers 18 °of angle variation); whereas [39] displayed a close performance to this work, since experimental control results showed that could track a signal with $\approx$ 45 °of variation.

Table 4.16: Verification simulations: dissertation's angle tracking performance.

Reference signal	RMSE	MAE	Maximum error (°) [a]
Sinusoidal wave	5.77	5.16	1.34
Square wave	22.68	14.36	1.61
Multilevel random[b]	6.29	2.58	2.29
Sawtooth[b]	9.87	3.61	6.16
Stair-shaped[b]	3.97	1.51	1.64
Triangle-shaped[b]	3.41	1.32	1.80

[a] Largest absolute error between angle values of the reference and the output signals, for equivalent signal sections. [b] Did not consider the first 5 s to compute the "maximum error" since the output had not reached the reference yet.

AAA vs. singe actuator

The following experiment compared the response between the AAA and a single actuator (agonist) to a step difference signal. The PID parameters were the same as used before. The control scheme employed only one controller, and the obtained results are in Figure 4.12. As expected, the response

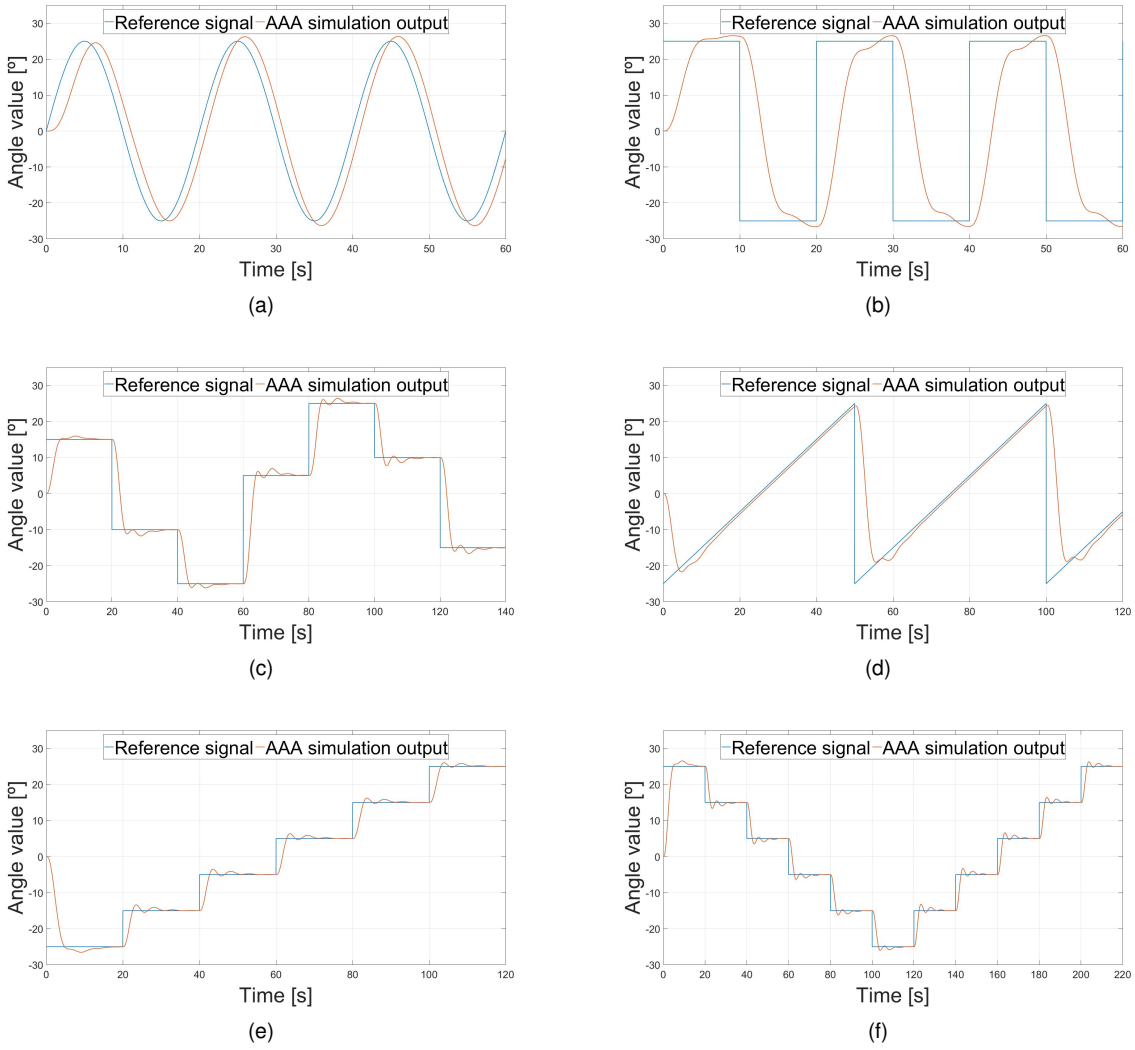

Figure 4.11: Verification simulations: angle tracking performance for different references. (a) Sinusoidal wave, (b) Square wave, (c) Multilevel random signal, (d) Sawtooth, (e) Stair-shaped, (f) Triangle-shaped.

Table 4.17: Verification simulations: control methodologies and tracking results from other works.

Control tracking variable	**Control methodology**	**Reference signal**	**Performance metric**	**Results**
Displacement (%) [32]	Feedforward + PID	Sinusoidal wave	Maximum tracking error	0.0949 %
Force (mN) [35]	Fuzzy controller (TSK) + PI	Arbitrary signal	Maximum absolute error	8.74 mN
			Mean absolute error	2.05 mN
Displacement (mm) [30] [a]	Feedforward (inverse models of displacement and temperature)	Step	RMSE [b]	≈ [0.25, 0.8] mm
Temperature (°C) [30] [a]				≈ [0.5, 1.5] °C
Angle (°) [39] [c]	Feedforward (to capture hysteresis)	Sinusoidal wave	Average error	3.4 °
		Random signal		4.2 °
Temperature (°C) [36]	PID	Step	Steady state error	< 1.15 %
Displacement (mm) [36]	2 PID (dual closed-loop)			1 %
Angle (°) [37] [d]	PI-type iterative learning	Sinusoidal wave	Absolute error	0.6817 °

[a] For the "Shieldex thread" (auto coiled) and for the proposed nonlinear model. [b] The RMSE interval is an approximation for the results of the three step references. [c] Captures the displacement/voltage hysteresis for a SMA actuator. Results for the linear model. [d] Obtained for the sinusoidal wave with 9 °of amplitude using 3 pairs of SCP actuators.

was faster for the AAA, since it reached 0 °after ≈ 3 s, because of the antagonist's action, whereas the single actuator took ≈ 20 s to reach the same state, due to a slow cooling process. This validates, once again, the use of an antagonist actuator to enhance the contraction/expansion motion.

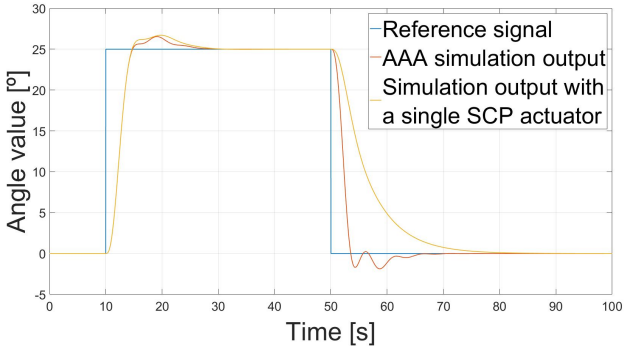

Figure 4.12: Verification simulations: AAA and single actuator performance comparison.

Disturbance introduction

This test studied how the control scheme would react to external disturbances that the system did not model. The test used a sine wave (same specs as in Table 4.16) as reference. The disturbances were 2 steps with -10 °and 10 °of amplitude, introduced at 15 and 45 s, as in Figure 4.13 (a). The time values aimed the maximum and minimum points of the reference, since they would drive the simulation to limiting conditions, as the request of higher voltages, in those points, would possibly lead to a smaller operation window to correct the disturbances (Figure 4.13 (b)). The experiments also verify how the system would behave with noisy angle readings introduced by the potentiometer (Figure 4.14 (a)).

Figure 4.13 (a) shows that the system recovers from the disturbances after ≈ 2.5 s. Considering the disturbances' magnitude and the dynamics without an antagonist, the response was relatively fast. The applied voltages held the maximum value (3.7 V/13.69 V^2) for a small period of time in Figure 4.13 (b), which is undesirable energetically and safety wise; but,it shows that the strategy works during harsher conditions to correct the disturbances. Plus, Figure 4.14 (a) shows that the control strategy can handle noisy measurements, together with external disturbances - at the expense of an extra effort from the voltage source, due to the requirement of faster voltage transitions (Figure 4.14 (b)).

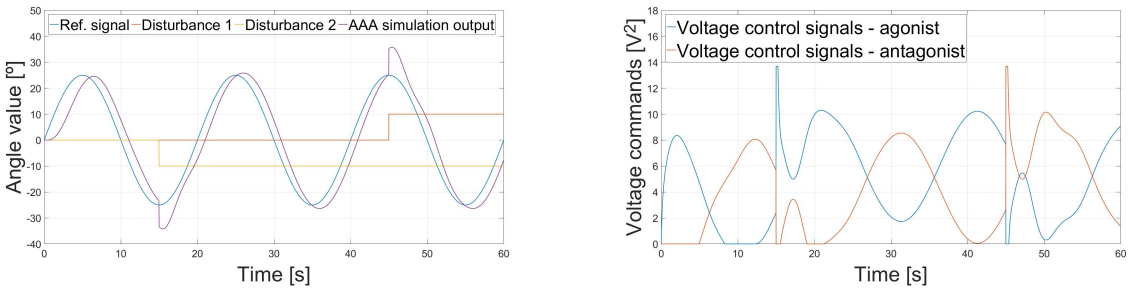

Figure 4.13: Verification simulations: inclusion of external disturbances. (a) Disturbances applied to a sine wave, (b) Required voltages to apply in both actuators to correct the disturbances.

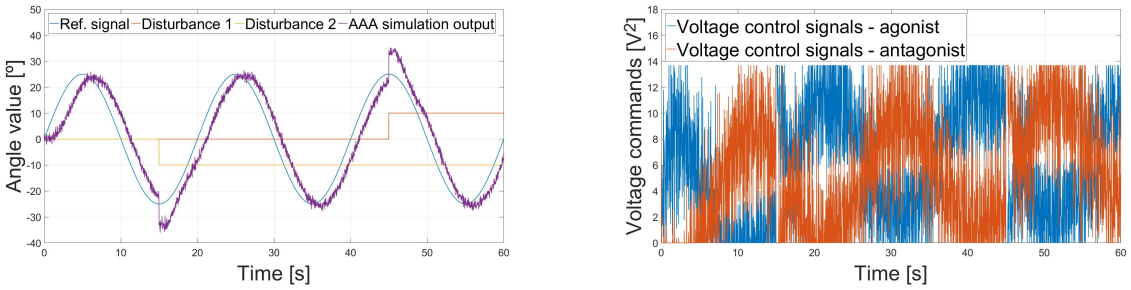

Figure 4.14: Verification simulations: inclusion of external disturbances and noisy measurements. (a) Reference tracking, (b) Required voltages to apply in both actuators.

Parameter variation

This test's goal was to verify how the pulley's radius change, from 15 to 7.5 mm, would affect the results. As expected, to follow the same reference, the AAA would need smaller displacements, since it would achieve larger angle variations with smaller contractions. Thus, after re-tuning the PID gains for the new radius (as in 3.4.1), one recreated the first two experiments of this subsection: the first found the new frequency and amplitude that a sine wave could track; and the second assessed the performance of the control method with the same references. The results revealed $\approx$ 0.10 Hz as the highest frequency to operate in; Tables 4.18 and 4.19 list the remaining results (Appendix D.6 has the associated figures).

Table 4.18 shows that the RMSE and phase difference were slightly smaller, for the same amplitudes in Table 4.15, and that the error between maximum points was somewhat higher. The maximum amplitude was 50 °, since was the value before the sign change - which indicates inability to supply higher voltages to reach the reference. The tests with 50 °(left-half of Table 4.19) led to poorer results than Table 4.16, as expected, due to the significant angle variation (100 °in contrast to 50 °). However, as shown in Appendix D.6, it is possible to follow, reasonably, higher amplitude signals. To improve the results, one can re-tune the PID gains for higher amplitudes. For the signals with 25 °of the previous tests (right-half of Table 4.19), the overall tracking performance (RMSE and MAE values) slightly increased, but the maximum error was higher - which suggests that the control was not as smooth as before.

Overall, the results express the validity of the adopted method to control the AAA's angle, but also, the potential to improve its design. Providing the angle requirements from the beginning (to adapt the pulley's radius, accordingly), together with accurate displacement specifications (to estimate the necessary actuators' length), can lead to a more efficient design to build a better AAA.

4.4.4 Verification: real system

This test attempts to display the validity of the AAA's working principle (model, controller and design) and showcase its applicability and operation, even without implementing a feedback strategy.

To use open-loop control in the AAA, the acquisition of voltages fed by both PID controllers to each actuator's model, in the simulations, followed a square root computation - the voltages were squared as seen in 3.3.1. The result was two data-sets (for each actuator) for a sinusoidal wave (same specs as

Table 4.18: Verification simulations: performance of 0.10 Hz sine waves with a pulley's radius of 7.5 mm.

Amplitude (°)	RMSE	Error between maximum points (°)[a]	Phase difference (°); time difference (s)[b]
15	6.63	-1.66	-32.40; -0.90
25	11.05	-2.76	-32.40; -0.90
35	15.47	-3.87	-32.40; -0.90
45	19.68	-3.19	-33.12; -0.92
50	21.79	-0.96	-36.0; -1.0
55	24.41	1.80	-38.88; -1.08
60	27.86	4.62	-39.60; -1.10

[a] Largest error between the maximum angle values of the reference signal wave and the output signal, for equivalent signal sections. [b] Obtained through time stamps associated to the maximum angle values of both the reference and output signals.

Table 4.19: Verification simulations: angle tracking performance with a pulley's radius of 7.5 mm.

Reference signal	50 °signals[a]			25 °signals		
	RMSE	MAE	Maximum error (°)[b]	RMSE	MAE	Maximum error (°)[b]
Sinusoidal wave	10.91	9.75	2.79	5.45	4.87	1.39
Square wave	45.77	28.59	5.03	20.33	11.69	5.11
Multilevel random[c]	13.57	5.80	8.62	6.21	2.80	5.53
Sawtooth[c]	20.04	7.20	10.03	9.09	3.37	2.59
Stair-shaped[c]	8.23	3.45	5.35	4.07	1.71	2.99
Triangle-shaped[c]	7.17	3.13	5.81	3.55	1.55	2.99

[a] The multilevel random, stair-shaped and triangle-shaped signals were redesigned to keep the same shape, within the same time interval. [b] Largest absolute error between angle values of the reference and the output signals, for equivalent signal sections. [c] Did not consider the first 5 s to compute the "maximum error" since the output had not reached the reference yet.

in Table 4.16), since it was a periodic signal easy to monitor with the naked eye. The next step was to load the data-sets to the Arduino, so each actuator could use them as lookup tables - both data-sets undergone decimation, since there was not enough memory to save all the data points. Figure 4.15 shows the open-loop control scheme; and Appendix D.5 contains a video validating the results.

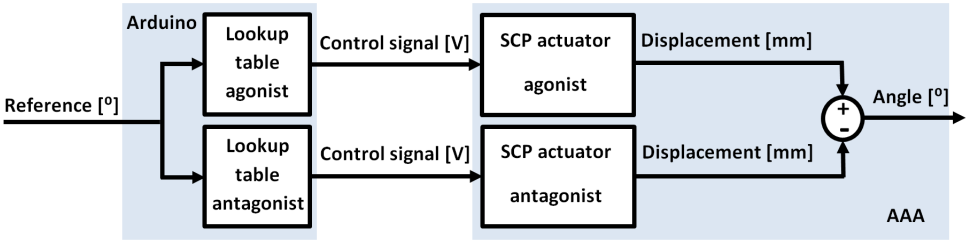

Figure 4.15: Verification real system: block diagram of the control strategy for the tests on the AAA.

The video shows that the angle variations did not follow closely the reference over time, neither for $\approx$ 82.7 g nor for $\approx$ 17.8 g loads hung in both actuators. The first set of weights choice was because subsection 3.3.3 used the same value to identify the single actuator model; and the second set choice was an attempt to attain a better performance. The maximum angle variations were small: $\approx$ 6 °(first experiment) and $\approx$ 9 °(second experiment). The results' quality was predictable: the model did not cover the AAA's dynamics, but one expected a closer performance with the simulations. Dismissing the antagonist's pulling opposing force, when the agonist contracts, was probably the main cause of such errors.

Additionally, the reference (25 °sine wave) has the maximum trackable amplitude found by simulations in 4.4.3 with the simpler model, which is not necessarily replicable by the AAA, for the aforementioned reasons. Moreover, the maximum amplitude of 20 °in Table 4.9 entails different conditions: the use of 0.23 mm fiber actuators, and the supply of higher voltage values for 10 seconds, continuously (unlike the current test). In short, the angle variations were small, even with a pulley that has small friction.

Force influence on the displacement

To approximate the opposing force influence of the actuators on the AAA's angle variation, the work performed an extra simulation. To do that, it used the data in Figure 4.8. The simulations used the voltages from the previous lookup tables, applied on each actuator for a sine wave, to illustrate the proximity of the new simulations results, with the ones in the real system, presented above.

First, note that the force values introduced in this test have the effect of extending the actuators (as seen in Figure 4.8 while hanging different weights). As a result, this force, which extends the actuator, will act against the contraction values already in place, generated via the lookup tables voltages. This means that the contraction difference between the two AAA's actuators will intuitively be smaller (see Figure 4.16 (a)). By assuming that the opposing force has a fixed value in each simulation that slightly extends the actuator, and by identifying the relation between the extension, and the AAA's actuators contraction difference, created by the lookup tables voltages, one can approximate the opposing force influence in the output (angle). From the results in Figure 4.16 (b), one can see that the bigger the opposing force is, the smaller the angle variation is. Note that, if the force is too low, there is a point that stops its influence on the final contraction difference - the simulation output becomes equal to the simplified model used along the work. If the opposing force is high, the AAA, using the same voltage values to contract, will have smaller output angles, since the contractions in place cannot counter-actuate, strongly, the force. The dead zone in the results is because the voltages need to reach a specific value to surpass the opposing force, to make the actuator contract (as one can see at 0 s, when the system is at rest). The other dead zones occur when the actuators resume to the rest position, and the active actuator needs, once again, to overcome the antagonist's opposing influence. Re-tunid the PID gains, to set proper voltages, can remove the dead zones. The dead zone was not clearly visible in the experiments with the real system (as the videos show), but one could notice the lag in the beginning, before a contraction. This may be due to the actuators' and pulley coupling and interaction across the experiment.

4.4.5 Verification: AAA's dynamics model

Since one could not use the AAA's model (3.11), these simulations will showcase its performance, and set a comparison with the results obtained for the tests upon the real system (i.e., the AAA).

First, note that the stiffness (k), mass (m), resistance (R), absolute conductivity (λ) and thermal mass (Cth) keep their estimated value for this analysis, since they represent intrinsic properties of the actuator. Still, bear in mind that λ and Cth change with temperature, which is not ideal. The values for the damping coefficient (β) and for the proportional coefficient (C) are invalid for this analysis because

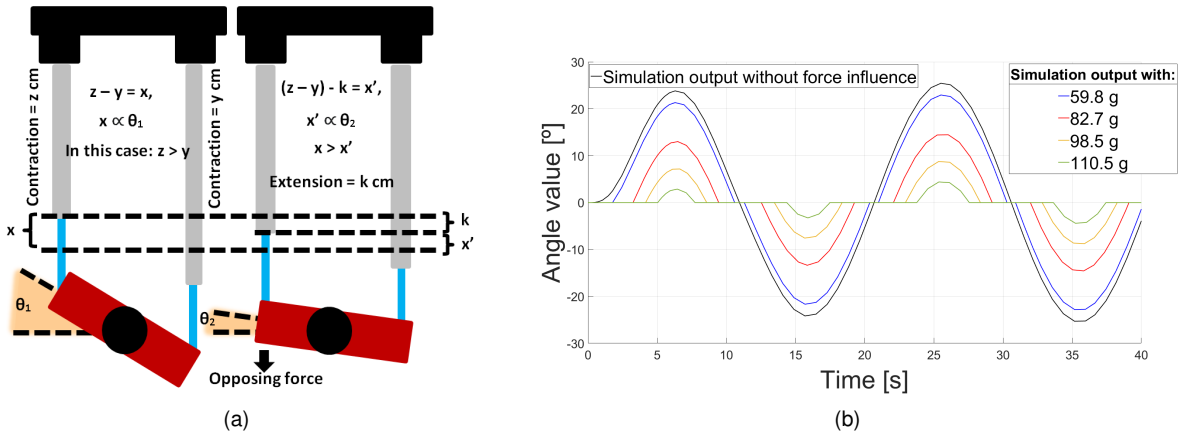

Figure 4.16: Verification real system: Influence of the actuators' opposing force in the AAA's displacement/angle variation. (a) Illustrative diagram of the adopted method, (b) Simulations results.

their derivation was from the identification coefficients of a single SCP actuator's behavior (instead of the AAA). The solution was to raise these parameters' values in the simulations, since β represents friction and C converts the change in temperature to change in force (and both are intuitively larger in an AAA).

Figure 4.17 shows the simulations results for the experiments in 4.2.2 (Table 4.9) and 4.4.4, which used actuators equal to the ones with nr. 1 and 2 (same parameters as in Table 4.14). In Figure 4.17 (a), the simulation reaches a similar value to the experiment after 10 s ($\approx$ 17 °across the 20 and 30 s marks) using a C and β 6 times bigger (which supports the thought process). The simulation in Figure 4.17 (b) used the same voltages fed to the actuators in the real system, and reached a similar angle variation ($\approx$ 6 °, instead of 50 °) with a C and β 3 times bigger. The results sustain the AAA's model since they display a closer performance to the AAA's behavior than the simpler model used along the work.

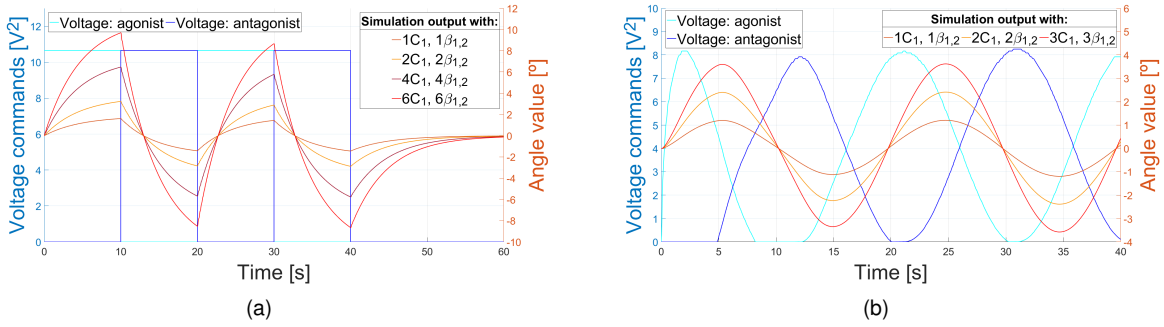

Figure 4.17: Verification of the AAA's model: simulations with the model (3.11). (a) Review of the experiment in Table 4.9 with 40/40.4 g and 10 s, (b) Review of the experiment in 4.4.4 for 82.7 g weights.

4.5 Review analysis

This section presents some of the most important features derived from the acquired data and sets a comparison with other works. The work reviews Table 2.1 to collect the biological muscles parameters to fill Table 4.20, and also adds extra parameters from the literature to set a detailed comparison with the AAA and the single actuator. The AAA's parameters computation considered the results in Table

4.9, for the maximum and minimum angle variations; and the single actuator's parameters computation followed the maximum and minimum results in Table 4.5. Appendix C.4 contains all the parameters' calculations. This section also sets relations between parameters to create metrics to allow extrapolation of the data, for different actuators (Table 4.21). The goal is to make the information clearer to allow future improvements, upon this work's findings, and to ease the research process. Note that, the average values in Table 4.21 comprised the data from all the functional manufactured SCP actuators (employed, or not) in this dissertation. The analysis with other works in Table 4.22 assesses their final structures (dismissing the overall quality, price and safety). The table lists eventual problems of applying those solutions in prostheses/orthoses regarding portability, performance and resemblance to muscles.

Table 4.20: Review analysis: comparison of biological muscles, the AAA and single SCP actuators.

Parameter	**Mammalian skeletal muscle**	**AAA structure**[a]	**Single SCP actuator**[c]
Typical (Max.) strain (%)	20 ($>$40) [1, 4]	2.1 (7.3)	15.7 (17.7)
Typical (Max.) work density (kJ.m^{-3})	8 ($<$40) [1, 4]	0.00153 (0.00255)	9.2 (13.1)
Typical (Max.) efficiency (%)	(40) [1]	0.0045 (0.0054)	0.027 (0.031)
Typical density (kg.m^{-3})	1037 [1]	103.6	3461.5[d]
Typical (Max.) specific power (W.kg^{-1})	50 (284) [1]	0.0025 (0.0030)	0.53 (0.76)
Stiffness (N/m)	Adaptable [1]	108.98	54.49
Typical (Max.) stress (MPa)	0.1 (0.35) [1, 4]	3.40 (6.15)	3.68 (4.63)
Cycle life (Nr. of cycles)	$>10^9$ [1, 4]	NA	NA
Typical (Max.) bandwidth (Hz)	(20) [1]	(0.28)[b]	(0.18)[e]
Cost (€)	–	$\approx$ 35	$\approx$ 0.2
Stimulus	Chemical	Heat (Joule heating)	Heat (Joule heating)
Amplitude of stimulus	–	$\leq$ 3.7 V, $<$4 A	$\leq$ 3.7 V, $<$4 A
Relative speed (full cycle)	Medium [7]	Slow	Slow

NA stands for "not available", meaning that the parameter could not be estimated. [a] Results for the actuators nr. 16 and 17. [b] Obtained following the method in 4.4.2, but for actuators made from 0.23 mm fiber. [c] Results for the actuator nr. 16. [d] Mass is 4.5 g. [e] Obtained following the method in 4.4.2, but it used only one controller and an actuator made from 0.23 mm fiber.

Table 4.21: Review analysis: average manufacturing parameters and metrics of SCP actuators.

Diam. (mm) - initial length (cm) - final length (cm)	**Average revs. to start coiling [min; max]**	**Average of total revs. [min; max]**	**Av. practical length after twisted & coiled w\weight (cm)**	**Average theoretical copper wire's resist. (Ω)**	**Average of copper wire turns around the actuator**	**Init. length/ av. nr. revs to start coiling (mm/revs.)**	**Init. length/ av. nr of total revs. (mm/revs.)**	**Av. practical length/ initial length (cm/cm)**
0.23 - 40 - 7.5	397 [385; 405]	621 [610; 634]	8.0	0.96	182	1.01	0.64	0.20
0.23 - 55 - 10.5	561 [545; 585]	869 [851; 888]	11.4	1.13	204	0.98	0.63	0.21
0.23 - 100 - 7.5	971 [955; 990]	1523 [1458; 1565]	20.4	0.97	98	1.03	0.66	0.20
0.33 - 40 - 7.5	310 [305; 320]	518 [500; 532]	8.7	1.05	165	1.29	0.77	0.22
0.33 - 55 - 10.5	424 [415; 440]	681 [673; 689]	11.8	1.27	195	1.30	0.81	0.21
0.33 - 100 - 7.5	770 [745; 790]	1201 [1155; 1241]	21.5	1.07	95	1.30	0.83	0.22
0.45 - 40 - 7.5	223 [215; 230]	368 [356; 378]	8.7	1.29	153	1.79	1.09	0.22
0.45 - 55 - 10.5	314 [310; 325]	510 [504; 519]	12.0	1.49	178	1.75	1.08	0.22
0.45 - 100 - 7.5	543 [525; 560]	896 [857; 948]	22.0	1.31	90	1.84	1.12	0.22

The AAA and biological muscles parameters in Table 4.20 revealed that the AAA has low efficiency (common feature of SCP-type actuators [4]), and also low output work. The friction between materials (not accounted), poor coupling between the pulley and actuators, and the opposing force imposed by the antagonist, every time the agonist contracts, help justifying these results. It was also clear that the

Table 4.22: Review analysis: drawbacks of different structures built in other works.

Applications	[ref]	Contraction tasks only	1 actuator to >1 joint	Long actrs.	Does not use antagonist	Rubber bands	Slow extension	Power supply	DAQ, PC	CPU fans	Track device
Prost.	[10]	X	X	X	X		X	X		X	
	[8]	X	X	X		X	NA	X			
Orthoses	[26]	X	X	X		X	NA	X	X		X
	[42]	X	X		X		X	X	X		X
	[28]	X		X	X		X	X	X		X
	[22]	X	X		X		NA	X			
Antagonistic	[37]	Does not link force with angle variations: actuators only contract if stretched; Setup: power supply, PC, AD/DA board.									
	[32]	Does not work as natural muscles: the structure contracts and expands; Displacement (and future angle relation) acquisition is difficult; Setup: power supply, PC, laser sensor, AD/DA board.									
	[23]	Does not work as natural muscles: the origin and insertion points have different locations; Setup: power supply.									

"X" means it checks. "NA" means "not available" in the referenced work. "Track device" means it uses unsuitable tracking devices.

displacement, associated to the AAA's maximum angle variation, did not match the maximum possible (attained by a single actuator). The AAA's volume led to poor results too, since it was an approximation of a rectangular cuboid (the real volume was smaller). In contrast, the single actuator's results followed closer the biological muscles' parameters, i.e., there is a drop of performance when placing the actuators in the AAA. Clever designs (lighter components in less space) can help solving the problems; but, finding the optimal tension that both actuators must have in the AAA must be the focus. This would help setting optimal displacement/angle variations for the actuators, despite the opposing pulling force.

Table 4.21 shows that it is possible to estimate the revolutions that will start the actuator's coiling process, according to its diameter and length. This is useful to manufacture mandrel coiled actuators. The results also predict the total number of revolutions that each fiber would need to produce an auto coiled actuator. The table also provides the average number of copper wire turns around the actuator, together with the average electric resistance that the work found to be the most effective for the working conditions. One can also confirm, as expected, that the initial actuator length has a direct relation with the number of revolutions - there is a constant value for each diameter. Thus, these results can contribute to the complete automation of the manufacturing process.

Moreover, the AAA overcomes some of the problems in Table 4.22: with angle requirements it is possible to adapt the pulley's radius and estimate the actuators length (as seen before), to develop custom joint-type structures (e.g. to use in prostheses). The AAA enhances the expansion speed, uses a small battery, and can still employ a feedback strategy (only [28, 32, 37] use feedback), as discussed next in the conclusions. Long actuators may lead to large displacements, but there are ways to use smaller actuators to obtain good motion ranges (an AAA, for instance). Plus, they have large resistances, which entails longer actuation times to contract (with small voltages), unlike the AAA's actuators.

Chapter 5

Conclusions

5.1 Achievements

This dissertation's purpose arose from the need of developing artificial muscles that were able to match the biological muscles' main properties, and from the possibility to implement them to obtain cheaper and better prostheses. For that reason, the work adopted a promising new technology, with desirable features to reproduce biological muscles. This technology uses standard fishing line as the raw material to produce SCP actuators, i.e., artificial muscles. The work accomplished, for the most part, the objectives: justified and provided detailed steps to perform each stage of the manufacturing process; assessed the performance of two types of actuators and analyzed their properties with experiments; implemented both control and modeling strategies and estimated the model parameters; employed a technique to achieve quicker expansion actuation times; and built a demonstrative application (AAA). In the end, Table 4.20 expressed the resemblance to biological muscles: single SCP actuators parameters were closer to natural muscles than the AAA's parameters (but neither one matched the muscles).

The AAA with two actuators was the most suited method to deal with the expansion issue. However, setup limitations (with the potentiometer) did not allow the direct measurement of the AAA's angle variation, which prevented the use of an accurate AAA's model. The model followed the individual behavior of each actuator, since only the displacement was possible to acquire for the identification (the angle values corresponded to a transformation from linear to angular motion). The simulations showed good enough performance with the AAA's simplified model. However, the real system results were not satisfactory because of the AAA's dynamics approximation. Still, the overall results met most of the expectations, and the comparison analyses with other works' findings, also sustained them.

The work verified that single SCP actuators are easy to model, since the heat influence on the displacement describes its dynamics properly. Nevertheless, different associations between actuators (AAA) entail different dynamics, and the inclusion of hysteresis (if required) in the model may overcomplicate it. The possibility of using simple models makes the control straightforward. SCP actuators are cheap and easy to manufacture, even with widely available materials (the process takes time, but can be automated). Their lightweight and flexibility promote the use in artificial muscles. Also, the stress and the

work density display comparable values to natural muscles. Plus, their weight lifting ability is attractive: a test showed that an actuator could lift a weight 167 times heavier than its weight 11 % of its length. The downside of SCP actuators is the low output work in contrast to the input energy, which leads to an inefficient process, probably due to a poor heat transfer rate from the copper wire to the fiber; the AAA also loses efficiency due to the antagonist opposing force. The employment in prostheses, besides an alternative and efficient heating process, requires superior batteries to increase the autonomy and to excite several actuators simultaneously.

5.2 Future Work

In the future, besides using a compliant sensor with its dynamics to acquire the angle and enable the use of the derived AAA's model (3.11), reducing the AAA's weight and volume (with a PCB) is essential. A new potentiometer, a rotary encoder, or a strain gauge are valid sensor options. A review of the pulley and actuators coupling is necessary to allow smoother rotations too. The performance with a set (array) of actuators in the AAA (to replicate the recruitment process of the muscle fibers), and the impact of conductive fibers to speed up the manufacturing process, must be part of future studies as well. Assessing black-box modeling strategies performance is something to experiment, as well as measuring all the current model's parameters directly with instruments.

It is also relevant to increase the AAA's DOF, for example, as in a human finger (Appendix D.7), and to study techniques used in active prostheses (electromyography - EMG - or mechanomyography - MMG) to set a relation between user intent and movement. The path to develop artificial muscles close to skeletal muscles must be arrays of SCP actuators and its control as a whole. As in Appendix D.7, a compliant fabric wrapped around the actuators set that is able to heat (slightly affecting the displacement), would avoid using one controller for each actuator. Searching for compliant conductive fabrics that heat fast without large currents, to wrap the actuators; or integrate directly SCP actuators in these fabrics' internal structure is, therefore, a must. Thus, the ideal solution should have low electric resistance, following the same method for mono-filament fibers with a resistive wire (multi-filament fibers have high resistances), or following a new design with a suitable conductive fabric.

In short, and despite the low TRL (technology readiness level), some projects (of prostheses and orthoses) using SCP actuators were already able to display their potential; therefore, in a long-term period, these actuators can become a recurrent option for artificial muscles in medical devices applications.

Bibliography

[1] J. D. W. Madden, N. A. Vandesteeg, P. A. Anquetil, P. G. A. Madden, A. Takshi, R. Z. Pytel, S. R. Lafontaine, P. A. Wieringa, and I. W. Hunter. Artificial muscle technology: physical principles and naval prospects. *IEEE Journal of Oceanic Engineering*, 29(3):706–728, 2004. ISSN 0364-9059 VO - 29. doi: 10.1109/JOE.2004.833135. URL https://ieeexplore.ieee.org/document/1353424. viewed on April 2019.

[2] M. C. Yip and G. Niemeyer. On the Control and Properties of Supercoiled Polymer Artificial Muscles. *IEEE Transactions on Robotics*, 33(3):689–699, 2017. ISSN 1941-0468. doi: 10.1109/TRO.2017.2664885. URL https://ieeexplore.ieee.org/document/7864464. viewed on April 2019.

[3] C. S. Haines, M. D. Lima, N. Li, G. M. Spinks, J. Foroughi, J. D. W. Madden, S. H. Kim, S. Fang, M. J. de Andrade, F. Goktepe, O. Goktepe, S. M. Mirvakili, S. Naficy, X. Lepro, J. Oh, M. E. Kozlov, S. J. Kim, X. Xu, B. J. Swedlove, G. G. Wallace, and R. H. Baughman. Artificial Muscles from Fishing Line and Sewing Thread. *SCIENCE*, 343(6173):868–872, 2014. ISSN 0036-8075. doi: 10.1126/science.1246906. URL https://science.sciencemag.org/content/343/6173/868. viewed on April 2019.

[4] S. M. Mirvakili and I. W. Hunter. Artificial Muscles: Mechanisms, Applications, and Challenges. *Advanced Materials*, 30(6):1–28, 2018. ISSN 0935-9648. doi: 10.1002/adma.201704407. URL https://onlinelibrary.wiley.com/doi/full/10.1002/adma.201704407. viewed on April 2019.

[5] M. Suzuki and N. Kamamichi. Control of twisted and coiled polymer actuator with anti-windup compensator. *SMART MATERIALS AND STRUCTURES*, 27(7):1–9, 2018. ISSN 0964-1726. doi: 10.1088/1361-665X/aabcb0. URL https://iopscience.iop.org/article/10.1088/1361-665X/aabcb0. viewed on April 2019.

[6] P. Zhang and G. Li. Healing-on-demand composites based on polymer artificial muscle. *Polymer*, 64:29–38, 2015. ISSN 0032-3861. doi: 10.1016/j.polymer.2015.03.022. URL https://www.sciencedirect.com/science/article/pii/S0032386115002505?via%3Dihub. viewed on April 2019.

[7] H. M. Herr and R. D. Kornbluh. New horizons for orthotic and prosthetic technology: artificial muscle for ambulation. In *Smart Structures and Materials 2004: Electroactive Polymer Actuators and Devices (EAPAD)*, San Diego CA USA, 2004. doi: 10.1117/12.544510.

URL https://www.spiedigitallibrary.org/conference-proceedings-of-spie/5385/1/New-horizons-for-orthotic-and-prosthetic-technology--artificial-muscle/10.1117/12.544510.full. viewed on April 2019.

[8] A. Arjun, L. Saharan, and Y. Tadesse. Design of a 3D printed hand prosthesis actuated by nylon 6-6 polymer based artificial muscles. In *IEEE International Conference on Automation Science and Engineering (CASE)*, pages 910–915, Fort Worth TX USA, 2016. ISBN 9781509024094. doi: 10.1109/COASE.2016.7743499. URL https://ieeexplore.ieee.org/document/7743499. viewed on April 2019.

[9] N. A. Atikah, L. Y. Weng, A. Anuar, C. C. Fat, I. Z. Abidin, and K. S. M. Sahari. Development of Nylon-Based Artificial Muscles for the Usage in Robotic Prosthetic Limb. *AIP Conference Proceedings*, 1883(1):1–8, 2017. ISSN 0094-243X. doi: 10.1063/1.5002060. URL https://aip.scitation.org/doi/abs/10.1063/1.5002060. viewed on April 2019.

[10] M. C. Yip and G. Niemeyer. High-performance robotic muscles from conductive nylon sewing thread. In *IEEE International Conference on Robotics and Automation (ICRA)*, pages 2313–2318, Seattle Washington, 2015. doi: 10.1109/ICRA.2015.7139506. URL https://ieeexplore.ieee.org/document/7139506. viewed on April 2019.

[11] R. R. Seeley, T. D. Stephens, and P. Tate. *Anatomia e Fisiologia, 8.ªEdição*. Lusociência, Loures, 8^{th} edition, 2011. ISBN: 978-972-8930-62-2.

[12] J. E. Muscolino. *Cinesiologia, o sistema esquelético e a função muscular*. Lusodidacta, Loures, 1^{st} edition, 2008. ISBN: 978-989-8075-12-3.

[13] T. Hassan, M. Cianchetti, M. Moatamedi, B. Mazzolai, C. Laschi, and P. Dario. Finite-Element Modeling and Design of a Pneumatic Braided Muscle Actuator With Multifunctional Capabilities. *IEEE/ASME Transactions on Mechatronics*, 24(1):109–119, 2019. ISSN 1083-4435. doi: 10.1109/TMECH.2018.2877125. URL https://ieeexplore.ieee.org/document/8501574/. viewed on April 2019.

[14] L. Klouda. Review Article: Thermoresponsive hydrogels in biomedical applications. A seven-year update. *European Journal of Pharmaceutics and Biopharmaceutics*, 97(Part B):338–349, 2015. ISSN 0939-6411. doi: 10.1016/j.ejpb.2015.05.017. URL https://www.sciencedirect.com/science/article/pii/S0939641115002490?via%3Dihub. viewed on April 2019.

[15] S. Horton and P. Dumond. Consistent Manufacturing Device for Coiled Polymer Actuators. In *40th Annual International Conference of the IEEE Engineering in Medicine and Biology Society (EMBC)*, pages 1849–1852, Honolulu HI USA, 2018. ISBN 9781538636466. doi: 10.1109/EMBC.2018.8512640. URL https://ieeexplore.ieee.org/document/8512640. viewed on April 2019.

[16] A. N. Semochkin. A device for producing artificial muscles from nylon fishing line with a heater wire. In *IEEE International Symposium on Assembly and Manufacturing (ISAM)*, pages 26–30,

Fort Worth TX USA, 2016. ISBN 9781509024124. doi: 10.1109/ISAM.2016.7750715. URL https://ieeexplore.ieee.org/document/7750715. viewed on April 2019.

[17] S. Aziz, S. Naficy, J. Foroughi, H. R. Brown, and G. M. Spinks. Twist-coil coupling fibres for high stroke tensile artificial muscles. *Sensors & Actuators: A. Physical*, 283:98–106, 2018. ISSN 0924-4247. doi: 10.1016/j.sna.2018.09.057. URL https://www.sciencedirect.com/science/article/pii/S0924424718308203?via%3Dihub. viewed on April 2019.

[18] D. L. Chandler. Nylon fibers made to flex like muscles. MIT News Office, November 2016. URL http://news.mit.edu/2016/nylon-muscle-fibers-1123. viewed on April 2019.

[19] C. S. Haines and G. Niemeyer. Closed-Loop Temperature Control of Nylon Artificial Muscles. In *IEEE/RSJ International Conference on Intelligent Robots and Systems (IROS)*, pages 6980–6985, Madrid Spain, 2018. ISBN 9781538680940. doi: 10.1109/IROS.2018.8593599. URL https://ieeexplore.ieee.org/document/8593599. viewed on April 2019.

[20] A. Simeonov, T. Henderson, Z. Lan, G. Sundar, A. Factor, J. Zhang, and M. Yip. Bundled Super-Coiled Polymer Artificial Muscles: Design, Characterization, and Modeling. *IEEE Robotics and Automation Letters*, 3(3):1671–1678, 2018. ISSN 2377-3766 VO - 3. doi: 10.1109/LRA.2018.2801469. URL https://ieeexplore.ieee.org/document/8279396. viewed on April 2019.

[21] P. Boyraz, G. Runge, and A. Raatz. An Overview of Novel Actuators for Soft Robotics. *Actuators*, 7(3):48, 2018. ISSN 2076-0825. doi: 10.3390/act7030048. URL https://www.mdpi.com/2076-0825/7/3/48. viewed on April 2019.

[22] S. Bahrami and P. Dumond. Testing of Coiled Nylon Actuators for Use in Spastic Hand Exoskeletons. In *40th Annual International Conference of the IEEE Engineering in Medicine and Biology Society (EMBC)*, pages 1853–1856, Honolulu HI USA, 2018. ISBN 9781538636466. doi: 10.1109/EMBC.2018.8512596. URL https://ieeexplore.ieee.org/document/8512596. viewed on April 2019.

[23] L. Li, J. Shen, J. Ma, H. Li, Y. Tian, W. Wang, X. Jia, and F. Xi. Artificial Muscles as Actuators in Symmetrical Structure. In *IEEE International Conference on Robotics and Biomimetics (ROBIO)*, pages 624–629, Kuala Lumpur Malaysia, 2018. doi: 10.1109/ROBIO.2018.8664746. URL https://ieeexplore.ieee.org/document/8664746. viewed on April 2019.

[24] L. Wu, M. Andrade, R. Rome, C. Haines, M. Lima, R. Baughman, and Y. Tadesse. Nylon-muscle-actuated robotic finger. In *SPIE Smart Structures and Materials + Nondestructive Evaluation and Health Monitoring*, San Diego CA USA, 2015. doi: 10.1117/12.2084902. URL https://www.researchgate.net/publication/277137306_Nylon-muscle-actuated_robotic_finger. viewed on April 2019.

[25] S. Aziz, S. Naficy, J. Foroughi, H. R. Brown, and G. M. Spinks. Thermomechanical effects in the torsional actuation of twisted nylon 6 fiber. *JOURNAL OF APPLIED POLYMER SCIENCE*, 134(47),

2017. ISSN 0021-8995. doi: 10.1002/app.45529. URL https://onlinelibrary.wiley.com/doi/full/10.1002/app.45529. viewed on April 2019.

[26] L. Saharan, M. J. de Andrade, W. Saleem, R. H. Baughman, and Y. Tadesse. iGrab: hand orthosis powered by twisted and coiled polymer muscles. *Smart Materials & Structures*, 26(10):1–14, 2017. ISSN 0964-1726. doi: 10.1088/1361-665X/aa8929. URL https://iopscience.iop.org/article/10.1088/1361-665X/aa8929. viewed on April 2019.

[27] K. H. Cho, M.-G. Song, H. Jung, S. Y. Yang, H. Moon, J. C. Koo, J.-d. Nam, and H. R. Choi. Fabrication and modeling of temperature-controllable artificial muscle actuator. In *6th IEEE International Conference on Biomedical Robotics and Biomechatronics (BioRob)*, pages 94–98, UTown Singapore, 2016. ISBN 9781509032877. doi: 10.1109/BIOROB.2016.7523604. URL https://ieeexplore.ieee.org/document/7523604. viewed on April 2019.

[28] L. Sutton, H. Moein, A. Rafiee, J. D. W. Madden, and C. Menon. Design of an assistive wrist orthosis using conductive nylon actuators. In *6th IEEE International Conference on Biomedical Robotics and Biomechatronics (BioRob)*, pages 1074–1079, UTown Singapore, 2016. ISBN 9781509032877. doi: 10.1109/BIOROB.2016.7523774. URL https://ieeexplore.ieee.org/document/7523774. viewed on April 2019.

[29] F. Karami and Y. Tadesse. Modeling of twisted and coiled polymer (TCP) muscle based on phenomenological approach. *Smart Materials & Structures*, 26(12):1–12, 2017. ISSN 0964-1726. doi: 10.1088/1361-665X/aa8d7d. URL https://iopscience.iop.org/article/10.1088/1361-665X/aa8d7d. viewed on April 2019.

[30] K. Masuya, S. Ono, K. Takagi, and K. Tahara. Feedforward Control of Twisted and Coiled Polymer Actuator Based on a Macroscopic Nonlinear Model Focusing on Energy. *IEEE Robotics and Automation Letters*, 3(3):1824–1831, 2018. ISSN 2377-3766 VO - 3. doi: 10.1109/LRA.2018.2801884. URL https://ieeexplore.ieee.org/document/8280995. viewed on April 2019.

[31] K. Masuya, S. Ono, K. Takagi, and K. Tahara. Nonlinear dynamics of twisted and coiled polymer actuator made of conductive nylon based on the energy balance. In *IEEE International Conference on Advanced Intelligent Mechatronics (AIM)*, pages 779–784, Munich Germany, 2017. ISBN 9781509059980. doi: 10.1109/AIM.2017.8014112. URL https://ieeexplore.ieee.org/document/8014112. viewed on April 2019.

[32] M. Suzuki and N. Kamamichi. Displacement control of an antagonistic-type twisted and coiled polymer actuator. *SMART MATERIALS AND STRUCTURES*, 27(3):1–10, 2018. ISSN 0964-1726. doi: 10.1088/1361-665X/aaa587. URL https://iopscience.iop.org/article/10.1088/1361-665X/aaa587. viewed on April 2019.

[33] M. Suzuki and N. Kamamichi. Simple controller design based on internal model control for twisted and coiled polymer actuator. *Actuators*, 7(3):1–13, 2018. ISSN 2076-0825. doi: 10.3390/act7030033. URL https://www.mdpi.com/2076-0825/7/3/33. viewed on April 2019.

[34] M. Suzuki and N. Kamamichi. Robust control with disturbance observer for twisted and coiled polymer actuator. *SMART MATERIALS AND STRUCTURES*, 27(8):1–9, 2018. ISSN 0964-1726. doi: 10.1088/1361-665X/aacf6d. URL https://iopscience.iop.org/article/10.1088/1361-665X/aacf6d. viewed on April 2019.

[35] M. Jafarzadeh, N. Gans, and Y. Tadesse. Control of TCP muscles using Takagi-Sugeno-Kang fuzzy inference system. *Mechatronics*, 53:124–139, 2018. ISSN 0957-4158. doi: 10.1016/j.mechatronics.2018.06.007. URL https://www.sciencedirect.com/science/article/pii/S0957415818300965?via%3Dihub. viewed on April 2019.

[36] X. Tang, K. Li, W. Chen, D. Zhou, S. Liu, J. Zhao, and Y. Liu. Temperature self-sensing and closed-loop position control of twisted and coiled actuator. *Sensors & Actuators: A. Physical*, 285:319–328, 2019. ISSN 0924-4247. doi: 10.1016/j.sna.2018.11.040. URL https://www.sciencedirect.com/science/article/pii/S0924424718313268?via%3Dihub. viewed on April 2019.

[37] S. Ono, K. Masuya, K. Takagi, and K. Tahara. Trajectory tracking of a one-DOF manipulator using multiple fishing line actuators by iterative learning control. In *IEEE International Conference on Soft Robotics (RoboSoft)*, pages 467–472, Livorno Italy, 2018. doi: 10.1109/ROBOSOFT.2018.8405370. URL https://ieeexplore.ieee.org/document/8405370. viewed on April 2019.

[38] J. Zhang, K. Iyer, A. Simeonov, and M. C. Yip. Modeling and Inverse Compensation of Hysteresis in Supercoiled Polymer Artificial Muscles. *IEEE Robotics and Automation Letters*, 2(2):773–780, 2017. ISSN 2377-3766 VO - 2. doi: 10.1109/LRA.2017.2651401. URL https://ieeexplore.ieee.org/document/7814286. viewed on April 2019.

[39] J. Zhang, A. Simeonov, and M. C. Yip. Three-dimensional hysteresis compensation enhances accuracy of robotic artificial muscles. *Smart Materials & Structures*, 27(3):1–17, 2018. ISSN 0964-1726. doi: 10.1088/1361-665X/aaa690. URL https://iopscience.iop.org/article/10.1088/1361-665X/aaa690. viewed on April 2019.

[40] T. A. Luong, S. Seo, J. C. Koo, H. R. Choi, and H. Moon. Differential hysteresis modeling with adaptive parameter estimation of a super-coiled polymer actuator. In *14th International Conference on Ubiquitous Robots and Ambient Intelligence (URAI)*, pages 607–612, Jeju South Korea, 2017. doi: 10.1109/URAI.2017.7992683. URL https://ieeexplore.ieee.org/document/7992683. viewed on April 2019.

[41] L. Saharan and Y. Tadesse. Robotic hand with locking mechanism using TCP muscles for applications in prosthetic hand and humanoids. In *SPIE Smart Structures and Materials + Nondestructive Evaluation and Health Monitoring*, Las Vegas NV USA, 2016. doi: 10.1117/12.2219535. URL https://www.researchgate.net/publication/301336391_Robotic_hand_with_locking_mechanism_using_TCP_muscles_for_applications_in_prosthetic_hand_and_humanoids. viewed on April 2019.

[42] A. G. Patino, A. Ferrone, C. G. D. Gastelum, and C. Menon. A Novel Biomedical Technology Based on the Use of Artificial Muscles to Assist with Hand Functions. In *IEEE 9th Annual Information Technology, Electronics and Mobile Communication Conference (IEMCON)*, pages 620–625, Vancouver BC Canada, 2018. ISBN 9781538672662. doi: 10.1109/IEMCON.2018.8615033. URL https://ieeexplore.ieee.org/document/8615033. viewed on April 2019.

[43] S. Kianzad, M. Pandit, J. D. Lewis, A. R. Berlingeri, K. J. Haebler, and J. Madden. Variable stiffness and recruitment using nylon actuators arranged in a pennate configuration. In *SPIE Smart Structures and Materials + Nondestructive Evaluation and Health Monitoring*, San Diego CA USA, 2015. doi: 10.1117/12.2086799. URL https://www.researchgate.net/publication/282686846_Variable_stiffness_and_recruitment_using_nylon_actuators_arranged_in_a_pennate_configuration. viewed on April 2019.

[44] S. Estrada-Flores, I. Merts, B. De Ketelaere, and J. Lammertyn. Development and validation of "grey-box" models for refrigeration applications: A review of key concepts. *International Journal of Refrigeration*, 29(6):931–946, 2006. ISSN 01407007. doi: 10.1016/j.ijrefrig.2006.03.018. URL https://www.sciencedirect.com/science/article/pii/S0140700706000983?via%3Dihub. viewed on July 2019.

[45] J. M. Lemos. Linear state feedback. IST-DEEC- AC Sistemas, Decisão e Controlo, 2018. URL https://fenix.tecnico.ulisboa.pt/downloadFile/1407993358872211/CEE-2-eng.pdf. Theoretical slides for the Controlo em Espaço de Estados course held in IST during 2018 2^{nd} semester.

Appendix A

Circuit diagrams

The current appendix contains all the components and circuits employed during the work's different stages. The codes loaded to the Arduino board and a general MATLAB program (to adapt according the situation) to read and process simultaneously the data directly from the serial port (which the Arduino connects) are available in the following GitHub link: `https://github.com/GabrielSilva96/Dissertation-s-codes.git`

A.1 Circuit diagrams: list of components

Table A.1: Manufacturing: components used in the experimental setup to produce SCP actuators.

Components	Stage	Task
Arduino Uno R3 (4)	All the stages	Processes the information obtained by the sensors, provides reliable data according to the embedded code, and acts as a power source.
Geared motor (1)	Twisting and coiling	Twists and coils the nylon fibers.
Manual switch (2)		Manually stops or starts the motor's rotation.
Reflectance sensor array (3)		Counts the number of revolutions of the motor.
Oven	Annealing	Set the polymer structure, preventing involuntary untwisting.
PWM drive circuit	Training, modeling and control	Controls the voltage applied to the SCP actuator (automatically) through the PWM pins of the Arduino.
Li-ion rechargeable battery (1000 mAh 3.7 V)		Provides electric current to perform the Joule heating effect through the copper wire.
Ultrasonic ranging module (5)	Modeling	Measures the displacement of the SCP actuator.
Thermistor (6)		Measures the temperature introduced by the Joule effect.

The numbers next to the components name correspond to their location in Figure 3.1.

A.2 Circuit diagrams: manufacturing process

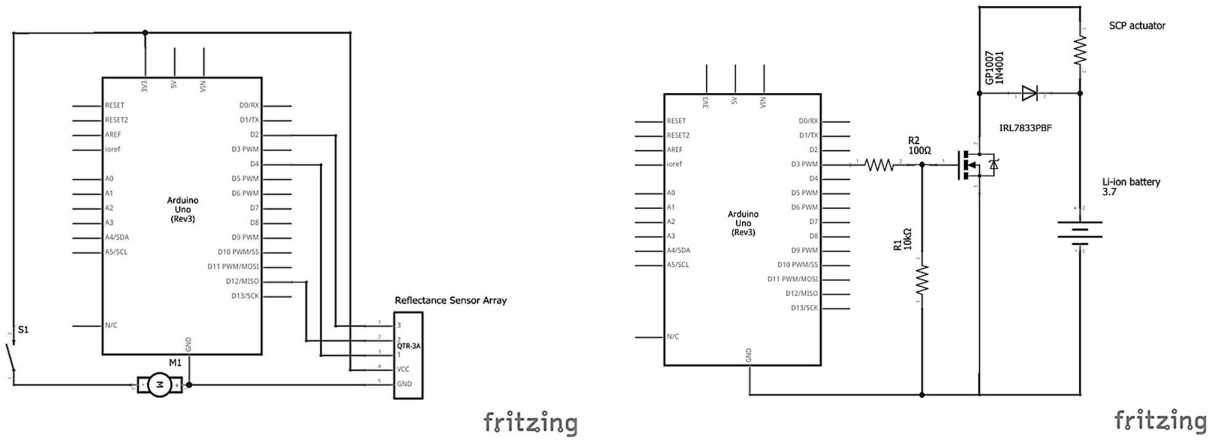

(a) Twisting and coiling stages

(b) Training stage

Figure A.1: Circuit diagrams employed during the manufacturing process (designed with Fritzing app).

A.3 Circuit diagrams: data acquisition

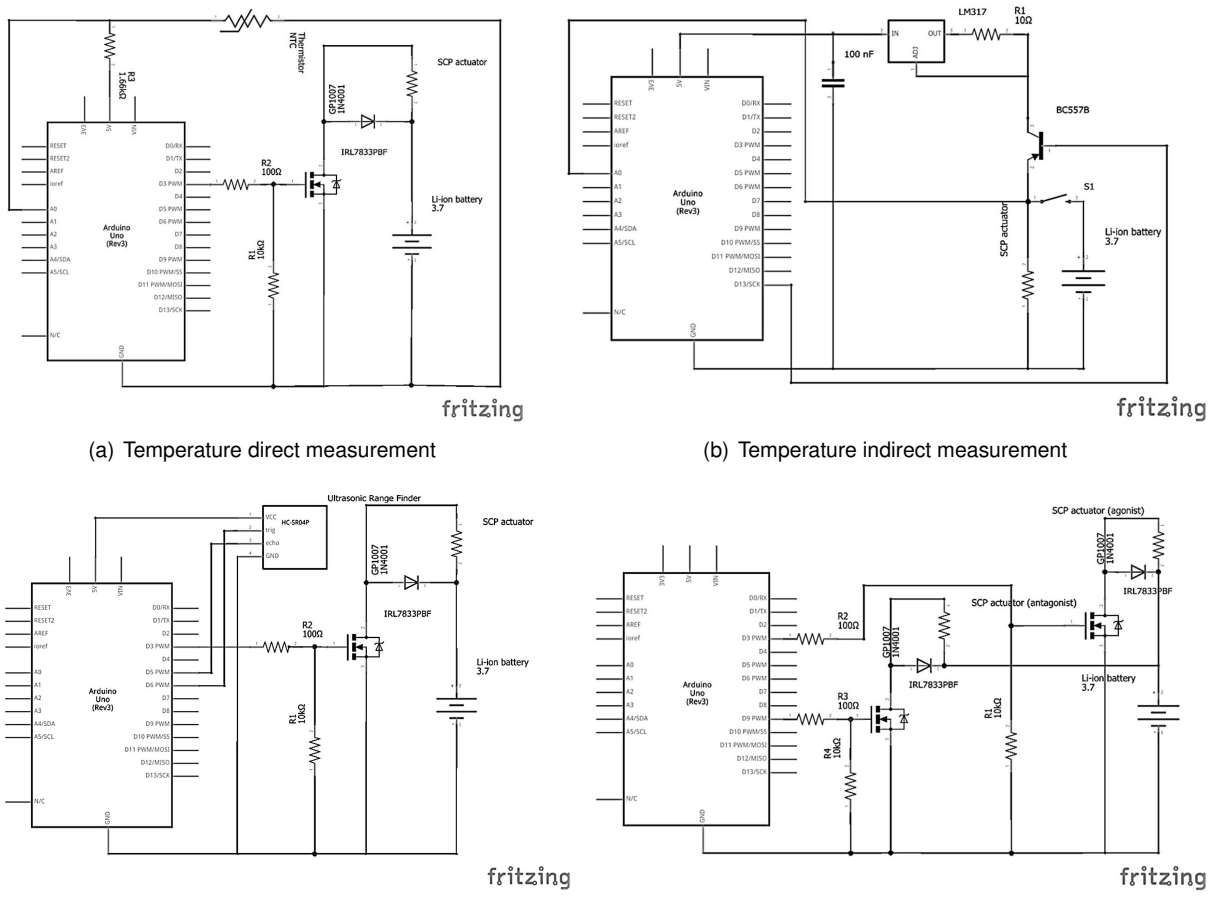

(a) Temperature direct measurement

(b) Temperature indirect measurement

(c) Displacement measurement

(d) Angle variation measurement (with 2 SCP actuators)

Figure A.2: Circuit diagrams employed during data acquisition (designed with Fritzing app).

Appendix B

Manufacturing

The current appendix contains the manufacturing parameters of all the remaining actuators used during this dissertation (apart from the ones presented in 3.1), and a list of different material options.

B.1 SCP actuators: manufacturing

Table B.1: Manufacturing: twisting and coiling parameters.

Parameter	**SCP actuator code**									
	10	**11**	**12**	**13**	**14**	**15**	**16**	**17**	**18**	**19**
Chapter/section[a]	4.1.1	4.1.1	4.1.1	4.1.1	4.1.1	4.1.1	4.1.2; 3.2	3.2	4.4.4	4.4.4
Fishing line diameter (mm)	0.23	0.33	0.45	0.23	0.33	0.45	0.23	0.23	0.33	0.33
Fishing line length after tied (cm)	40	40	40	100	100	100	40	40	40	40
Weight (g)[b]	40.4	82.7	150.9	40.4	82.7	150.9	40.4	40.4	82.7	82.7
Stress (MPa)	9.53	9.48	9.30	9.53	9.48	9.30	9.53	9.53	9.48	9.48
Nr. of revolutions to start coiling	395	310	215	990	790	560	400	395	310	305
Nr. of total revolutions	618	523	363	1565	1223	907	621	618	526	511
Revolutions per minute without any weight hung	145									
Actuator length after twist & coiling w\weight hung (cm)	8.0	8.7	8.7	20.0	20.5	21.5	8.0	8.0	8.8	8.6

[a] Chapters/sections that used the SCP actuators of this table. [b] Measured with the KERN EMB 500-1 precision electronic balance.

Table B.2: Manufacturing: annealing stage parameters.

Parameter	SCP actuator code									
	10	**11**	**12**	**13**	**14**	**15**	**16**	**17**	**18**	**19**
Length after framing (cm)	9.1	9.7	9.6	Not			9.1	9.0	9.9	9.7
- elongation (%)	- 113.8	- 111.5	- 110.3	applicable			- 113.8	- 112.5	-112.5	-112.8
Annealing type	Oven (warm hair)			2 ply configuration			Oven (warm hair)			
Annealing specs	135 °C 12 min (preheat oven for 5 min)			Not applicable			135 °C 12 min (preheat oven for 5 min)			
Length after annealing (cm)[a]	9.1	9.7	9.6	8.7	8.8	9.2	9.1	9.0	9.9	9.7
- with new structure (cm)	- 7.5	- 7.5	- 7.5	- 7.5	- 7.5	- 7.5	- 7.5	- 7.5	- 7.5	- 7.5

[a] Length after removing the actuator from the frame without any weight hung, for the 1 ply case, and length after folding the SCP actuator onto itself for the 2 ply case, also without any weight hung.

Table B.3: Manufacturing: training stage parameters.

SCP actuator code	Copper wire length (cm)	Theoretical resistance of the copper wire (Ω)[a]	Nr. of copper wire turns around the SCP actuator[b]	Training type	Training specs	Length after training (cm) - elongation (%)
10	43	0.92	190	Not applicable	Not applicable	Not applicable
11	48	1.03	160	Not applicable	Not applicable	Not applicable
12	62	1.33	160	Not applicable	Not applicable	Not applicable
13	46	0.98	100	Joule heating (electrothermally)	3.26 V (10.88 W) 5 s ON & 20 s OFF w\200.8 g hung (10x)	9.0 –120.0
14	49	1.05	90	Joule heating (electrothermally)	3.41 V (11.07 W) 8 s ON & 25 s OFF w\412.9 g hung (10x)	8.6 –114.7
15	61	1.30	85	Joule heating (electrothermally)	3.55 V (9.72 W) 15 s ON & 40 s OFF w\754.6 g hung (10x)	8.2 –109.3
16	45	0.96	170	Joule heating (electrothermally)	3.26 V (11.10 W) 5 s ON & 20 s OFF w\82.7 g hung (10x)	9.1 –121.3
17	45	0.96	185	Joule heating (electrothermally)	3.26 V (11.10 W) 5 s ON & 20 s OFF w\82.7 g hung (10x)	8.7 –116.0
18	52	1.11	170	Joule heating (electrothermally)	3.41 V (10.48 W) 8 s ON & 25 s OFF w\160.4 g hung (10x)	9.1 –121.33
19	52	1.11	170	Joule heating (electrothermally)	3.41 V (10.48 W) 8 s ON & 25 s OFF w\160.4 g hung (10x)	9.0 –120.0

[a] Considering the copper resistivity equal to $1.68 \times 10^{-8} \Omega \cdot m$ at 20 °C. [b] The actuator is fixed in a structure to create enough tension to wind the copper wire (as shown in Figure 3.2 (h)).

Table B.4: Manufacturing: materials used to produce SCP actuators in the literature.

Fiber material designation	Fiber diameter (mm)	Resistive wire	Wire diameter (mm)
Silver-coated nylon 6.6 (multi-filament)	0.38/0.76 [2]; 0.72 [10]; 0.294 [43]; 0.234/0.468 [22]; 0.20 [26, 35];	-	-
Nylon 6/6.6, "fishing line" [37], **"nylon"** [30, 36] **(mono-filament)**	0.77 [15]; 0.50/0.80 [16]; 0.34 [23]; 0.175 [19]; 0.50 [36]; 0.91 [30]; 0.33 [37]	Copper [16, 19, 23, 37]; nichrome [15, 30]; nickel [36]	0.127 [15]; 0.14 [16]; 0.0447 [19]; 0.20 [30, 36]; 0.10 [23, 37]

Appendix C

Auxiliary calculations

The current appendix contains the formulas and calculations (which the work's main body did not present) done to obtain important values and to assess different stages of the work.

C.1 Rewritten TE and TM models' transfer functions

$$C_{th}\Delta Ts = \frac{V^2}{R} - \lambda\Delta T \tag{C.1}$$

$$\Delta T = \frac{m}{C}s^2X + \frac{\beta}{C}sX + \frac{k}{C}X, \tag{C.2}$$

C.2 Intermediate calculations to compute the AAA's TM model

The system's description is as a difference of torques, between the agonist and antagonist, depending on which is starting the movement

$$\sum \mathcal{T} = \mathcal{T}_1 - \mathcal{T}_2, \tag{C.3}$$

and the sum of all torques is the inertia of the pulley (J_p) multiplied by the angular acceleration

$$J_p = \frac{1}{2}m_p r_p^2, \tag{C.4}$$

$$J_p\frac{\mathrm{d}^2\theta(t)}{\mathrm{d}t^2} = \mathcal{T}_1 - \mathcal{T}_2. \tag{C.5}$$

One can write the torque as the multiplication between tension force, applied to each muscle, and the pulley's radius (r_p).

$$J_p\frac{\mathrm{d}^2\theta(t)}{\mathrm{d}t^2} = T_1r_p - T_2r_p. \tag{C.6}$$

Replacing J_p in (C.6) by (C.4) and canceling the r_p terms, leads to

$$\frac{1}{2}m_p r_p\frac{\mathrm{d}^2\theta(t)}{\mathrm{d}t^2} = T_1 - T_2, \tag{C.7}$$

where m_p is the pulley's mass. The work computed the tensions of each muscle separately, considering Figure 3.6 (c). Index nr.1 will describe the active muscle (agonist) and nr.2 the one at rest (antagonist).

$$\sum \mathcal{F} = -T_1 + C_1 \Delta t(t) - \beta_1 \frac{\mathrm{d}x(t)}{\mathrm{d}t} - k_1 x(t) = m_1 \frac{\mathrm{d}^2 x(t)}{\mathrm{d}t^2}, \tag{C.8}$$

$$\sum \mathcal{F} = -T_2 + \beta_2 \frac{\mathrm{d}x(t)}{\mathrm{d}t} + k_2 x(t) = -m_2 \frac{\mathrm{d}^2 x(t)}{\mathrm{d}t^2}. \tag{C.9}$$

Rewriting these equations in order of the applied tensions and in terms of angular motion, results in

$$T_1 = C_1 \Delta t(t) - m_1 \frac{\mathrm{d}^2 \theta(t)}{\mathrm{d}t^2} r_p - \beta_1 \frac{\mathrm{d}\theta(t)}{\mathrm{d}t} r_p - k_1 \theta(t) r_p, \tag{C.10}$$

$$T_2 = m_2 \frac{\mathrm{d}^2 \theta(t)}{\mathrm{d}t^2} r_p + \beta_2 \frac{\mathrm{d}\theta(t)}{\mathrm{d}t} r_p + k_2 \theta(t) r_p, \tag{C.11}$$

then, replacing (C.10) and (C.11) in (C.7), leads to

$$\frac{1}{2} m_p r_p \frac{\mathrm{d}^2 \theta(t)}{\mathrm{d}t^2} = C_1 \Delta t(t) - m_1 \frac{\mathrm{d}^2 \theta(t)}{\mathrm{d}t^2} r_p - \beta_1 \frac{\mathrm{d}\theta(t)}{\mathrm{d}t} r_p - k_1 \theta(t) r_p - m_2 \frac{\mathrm{d}^2 \theta(t)}{\mathrm{d}t^2} r_p - \beta_2 \frac{\mathrm{d}\theta(t)}{\mathrm{d}t} r_p - k_2 \theta(t) r_p \tag{C.12}$$

Finally, one can rearrange equation (C.12) to obtain

$$\left(\frac{1}{2} m_p + m_1 + m_2\right) \frac{\mathrm{d}^2 \theta(t)}{\mathrm{d}t^2} r_p + (\beta_1 + \beta_2) \frac{\mathrm{d}\theta(t)}{\mathrm{d}t} r_p + (k_1 + k_2) \theta(t) r_p = C_1 \Delta t(t). \tag{C.13}$$

C.3 Performance metrics formulas

$$RMSE = \sqrt{\frac{\sum_{i=1}^{n} (Predicted_i - Actual_i)^2}{n}} \tag{C.14}$$

$$NRMSE = \left(1 - \frac{\sqrt{\frac{1}{n} \sum_{i=1}^{n} (Actual_i - Predicted_i)^2}}{\sqrt{\frac{1}{n} \sum_{i=1}^{n} (Actual_i - Actual_{average})^2}}\right) \times 100 \tag{C.15}$$

$$MAE = \frac{1}{n} \sum_{i=1}^{n} \mid Actual_i - Predicted_i \mid \tag{C.16}$$

C.4 Parameters calculations

Parameters of the AAA structure from Table 4.20

The displacement x computation used trigonometric functions, knowing the pulley's radius and angle:

$$x_{max} = tan(20\ ^\circ) \times 15\ mm = 5.5\ mm, \quad \text{and} \quad x_{min} = tan(6\ ^\circ) \times 15\ mm = 1.6\ mm, \tag{C.17}$$

therefore the strains are

$$strain_{x_{max}} = \frac{5.5\ mm}{75\ mm} \times 100 = 7.3\ \% \quad \text{and} \quad strain_{x_{min}} = \frac{1.6\ mm}{75\ mm} \times 100 = 2.1\ \%. \tag{C.18}$$

If one rewrites (3.7) in terms of linear motion comes

$$C_1\Delta t(t) = \left(\frac{1}{2}m_p + m_1 + m_2\right)\frac{\mathrm{d}^2x(t)}{\mathrm{d}t^2} + (\beta_1+\beta_2)\frac{\mathrm{d}x(t)}{\mathrm{d}t} + (k_1+k_2)x(t). \tag{C.19}$$

where $\beta_1 = \beta_2$ and $k_1 = k_2$, if the actuators are equal, and $C_1\Delta t(t)$ is the applied force $\mathcal{F}$ in the AAA:

$$\mathcal{F}_{x_{max}} = \left(\frac{1}{2}2\ g + 18.3\ g + 17.8\ g\right)9.8\ m.s^{-2} + (0.0303\times 2)\frac{5.5\ mm}{10\ s} + (54.49\times 2)5.5\ mm = 0.96\ N, \tag{C.20}$$

$$\mathcal{F}_{x_{min}} = \left(\frac{1}{2}2\ g + 75.9\ g + 82.7\ g\right)9.8\ m.s^{-2} + (0.0303\times 2)\frac{1.6\ mm}{5\ s} + (54.49\times 2)1.6\ mm = 1.74\ N. \tag{C.21}$$

Note that using the estimated parameters, obtained in Table 4.14 via simulation (C and β), represents just an approximation to compute $\mathcal{F}$, since they did not match the conditions in place in this analysis. Nevertheless, one expects them to describe the dynamics of the AAA to a certain degree.

To compute the work W performed by the AAA one used the following formula

$$W = \mathcal{F}.x.cos(\theta), \tag{C.22}$$

where $\mathcal{F}$ is the force (N), x is the displacement (m) and θ (°) is the angle between force and displacement:

$$W_{x_{max}} = 0.96\ N \times 5.5\ mm \times cos(0^\circ) = 0.005\ J, \quad \text{and} \tag{C.23}$$

$$W_{x_{min}} = 1.74\ N \times 1.6\ mm \times cos(0^\circ) = 0.003\ J. \tag{C.24}$$

To get the efficiency η, one computed the input energy E_{in} accounting the use of 3.26 V and considering both actuators' (16 and 17) resistances 0.96 Ω. The calculation considered the output energy equal to the work.

$$E_{inx_{max}} = \left(\frac{3.26}{0.96}\right)^2 0.96 \times 10\ s = 110.7\ J, \tag{C.25}$$

$$E_{inx_{min}} = \left(\frac{3.26}{0.96}\right)^2 0.96 \times 5\ s = 55.4\ J, \tag{C.26}$$

$$\eta_{x_{max}} = \left(\frac{0.005\ J}{110.7\ J}\right) \times 100 = 0.0045\ \%, \tag{C.27}$$

$$\eta_{x_{min}} = \left(\frac{0.003\ J}{55.4\ J}\right) \times 100 = 0.0054\ \%. \tag{C.28}$$

The output power P_{out} computation was via the work done by the system, as follows:

$$P_{outx_{max}} = \frac{0.005\ J}{10\ s} = 0.5\ mW, \tag{C.29}$$

$$P_{outx_{min}} = \frac{0.003\ J}{5\ s} = 0.6\ mW. \tag{C.30}$$

The stress computation assumed that the actuator's final diameter was equal to 0.6 mm and that the displacements were equal to 5.5 and 1.6 mm, as before, hence:

$$Stress_{x_{max}} = \frac{\mathcal{F}}{A_b} = \frac{0.96\ N}{\pi 0.3\ mm^2} = 3.40\ MPa, \tag{C.31}$$

$$Stress_{x_{min}} = \frac{\mathcal{F}}{A_b} = \frac{1.74\ N}{\pi 0.3\ mm^2} = 6.15\ MPa. \tag{C.32}$$

Parameters of a single SCP actuator from Table 4.20

The methods employed for the single SCP actuator are equivalent to the ones above. Formula (3.4) leads to (C.33); (C.34) and (C.35) express the force $\mathcal{F}$ applied to the actuator; and (C.36) and (C.37) describe the work W performed by the actuator. Note that, in this case, it is accurate to use the estimated parameters (C and β), since they entail equivalent conditions to this analysis.

$$C\Delta t(t) = m\frac{\mathrm{d}x^2(t)}{\mathrm{d}t^2} + \beta\frac{\mathrm{d}x(t)}{\mathrm{d}t} + kx(t), \tag{C.33}$$

$$\mathcal{F}_{x_{max}} = 59.8\ g \times 9.8\ m.s^{-2} + 0.0303 \times \frac{13.3\ mm}{5\ s} + 54.49 \times 13.3\ mm = 1.31\ N, \tag{C.34}$$

$$\mathcal{F}_{x_{min}} = 40.4\ g \times 9.8\ m.s^{-2} + 0.0303 \times \frac{11.8\ mm}{5\ s} + 54.49 \times 11.8\ mm = 1.04\ N, \tag{C.35}$$

$$W_{x_{max}} = 1.31\ N \times 13.3\ mm \times cos(0^\circ) = 0.017\ J, \tag{C.36}$$

$$W_{x_{min}} = 1.04\ N \times 11.8\ mm \times cos(0^\circ) = 0.012\ J. \tag{C.37}$$

The volume of the actuator $V_{actuator}$ considered a cylindrical shape with 0.6 mm diameter and 7.5 cm long, plus an extra volume to include the two terminal blocks.

$$V_{actuator} = \pi \times 0.3^2\ mm \times 7.5\ cm + 2 \times (7\ mm \times 7\ mm \times 13\ mm) = 1.3 \times 10^{-6}\ m^3. \tag{C.38}$$

The energy supplied to the actuator in both cases was 55.4 J (0.96 Ω, 3.26 V, 5 s), hence the efficiency η comes

$$\eta_{x_{max}} = \left(\frac{0.017\ J}{55.4\ J}\right) \times 100 = 0.031\ \%, \tag{C.39}$$

$$\eta_{x_{min}} = \left(\frac{0.012\ J}{55.4\ J}\right) \times 100 = 0.027\ \%. \tag{C.40}$$

The output power P_{out} computation was via the work done by the system, as follows:

$$P_{outx_{max}} = \frac{0.017\ J}{5\ s} = 3.4\ mW, \tag{C.41}$$

$$P_{outx_{min}} = \frac{0.012\ J}{5\ s} = 2.4\ mW. \tag{C.42}$$

The actuator stress computation was as follows:

$$Stress_{x_{max}} = \frac{\mathcal{F}}{A_b} = \frac{1.31\ N}{\pi 0.3^2\ mm} = 4.63\ MPa, \tag{C.43}$$

$$Stress_{x_{min}} = \frac{\mathcal{F}}{A_b} = \frac{1.04\ N}{\pi 0.3^2\ mm} = 3.68\ MPa. \tag{C.44}$$

Appendix D

Data and results acquired

The current appendix contains additional results to validate and complement the ones shown, and also results from all the remaining studied actuators that did not feature in the work's main body.

D.1 Elasticity results

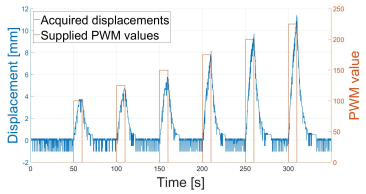

(a) Actuator nr. 16 with 82.7 g hung

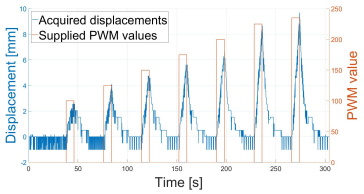

(b) Actuator nr. 2 with 160.4 g hung

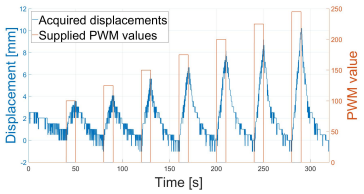

(c) Actuator nr. 3 with 299.7 g hung

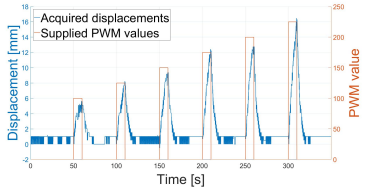

(d) Actuator nr. 7 with 82.7 g hung

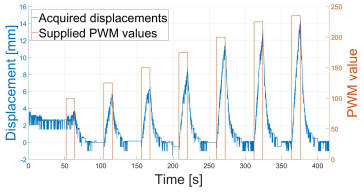

(e) Actuator nr. 8 with 160.4 g hung

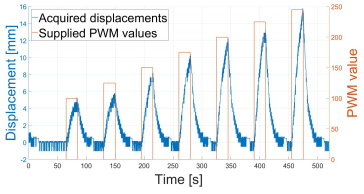

(f) Actuator nr. 9 with 299.7 g hung

Figure D.1: Elasticity tests: raw displacement data, obtained for varying voltages over different 1 ply actuators, with a constant weight hung.

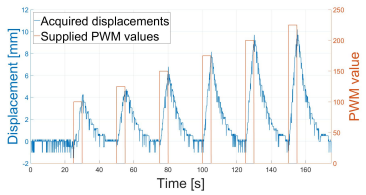

(a) Actuator nr. 4 with 200.8 g hung

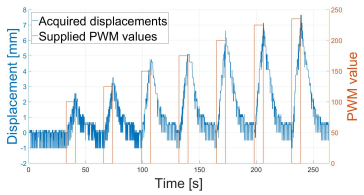

(b) Actuator nr. 5 with 412.9 g hung

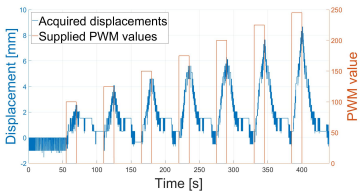

(c) Actuator nr. 6 with 754.6 g hung

Figure D.2: Elasticity tests: raw displacement data, obtained for varying voltages over different 2 ply actuators, with a constant weight hung.

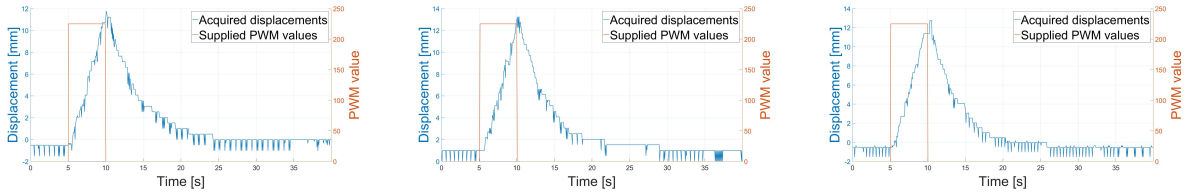

(a) Actuator nr. 16 with 40.4 g hung (b) Actuator nr. 16 with 59.8 g hung (c) Actuator nr. 16 with 82.7 g hung

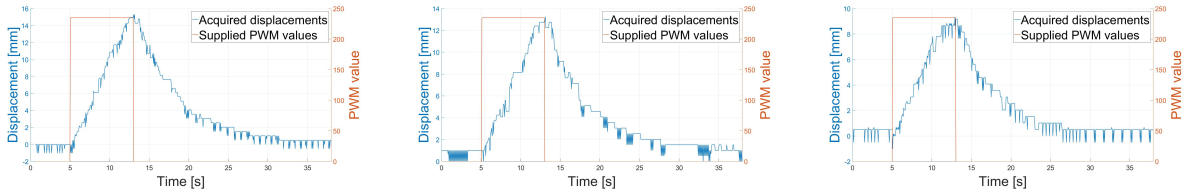

(d) Actuator nr. 2 with 82.7 g hung (e) Actuator nr. 2 with 129.4 g hung (f) Actuator nr. 2 with 160.4 g hung

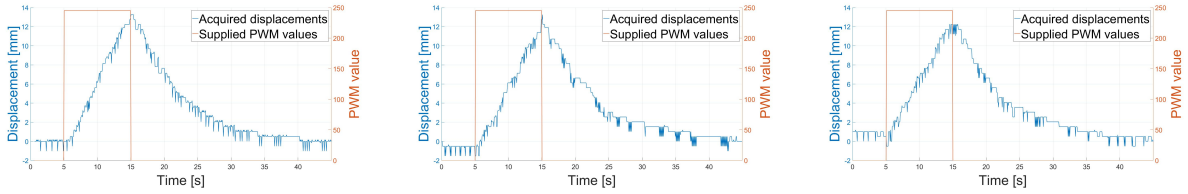

(g) Actuator nr. 3 with 150.9 g hung (h) Actuator nr. 3 with 223.8 g hung (i) Actuator nr. 3 with 299.7 g hung

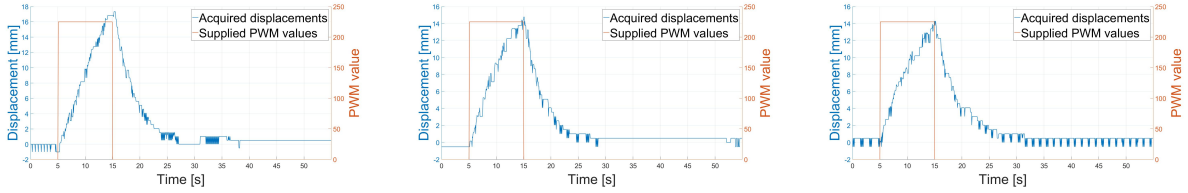

(j) Actuator nr. 7 with 40.4 g hung (k) Actuator nr. 7 with 59.8 g hung (l) Actuator nr. 7 with 82.7 g hung

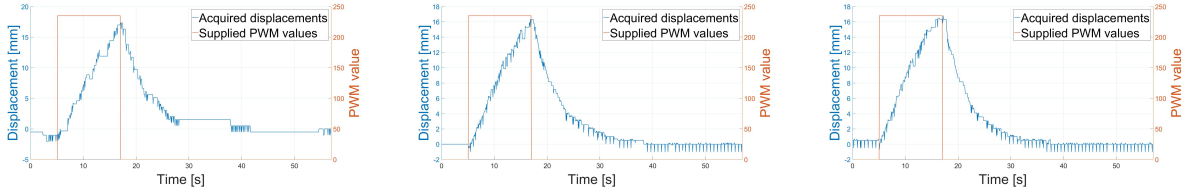

(m) Actuator nr. 8 with 82.7 g hung (n) Actuator nr. 8 with 129.4 g hung (o) Actuator nr. 8 with 160.4 g hung

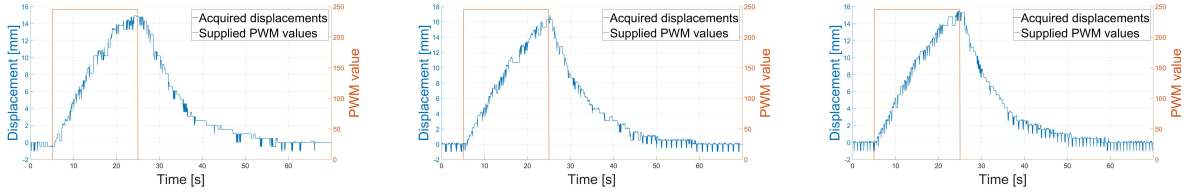

(p) Actuator nr. 9 with 150.9 g hung (q) Actuator nr. 9 with 223.8 g hung (r) Actuator nr. 9 with 299.7 g hung

Figure D.3: Elasticity tests: raw displacement data, obtained for varying weights over different 1 ply actuators, supplying a constant voltage.

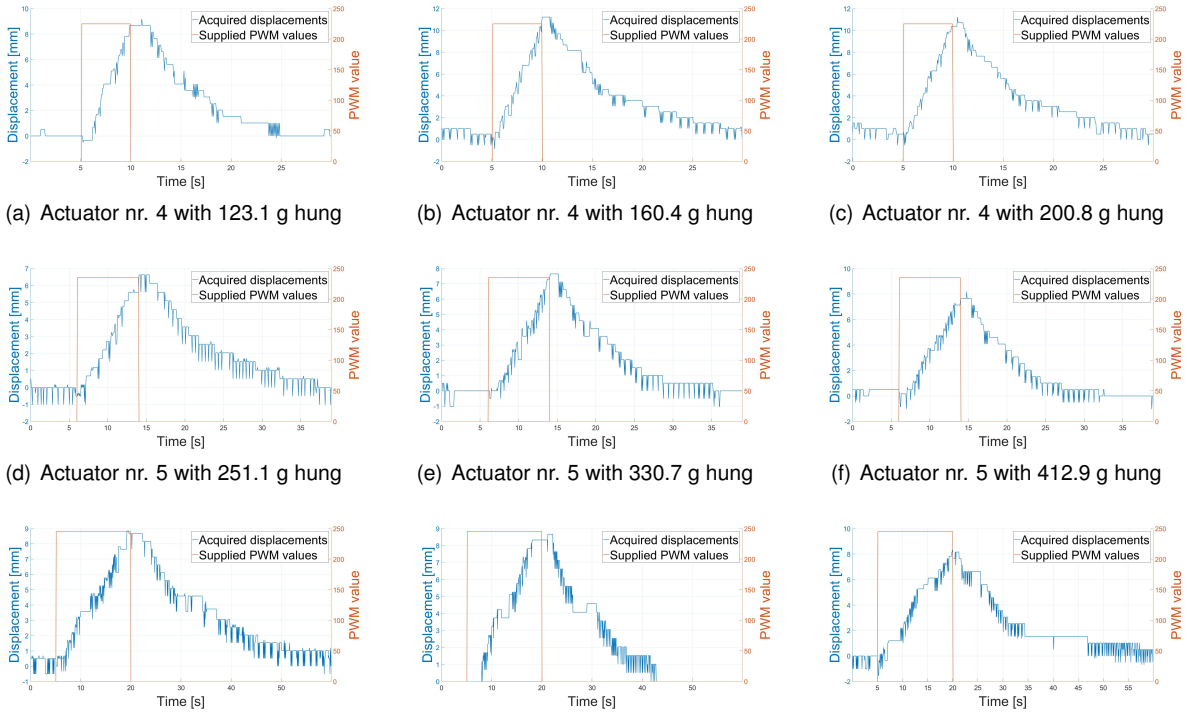

(a) Actuator nr. 4 with 123.1 g hung (b) Actuator nr. 4 with 160.4 g hung (c) Actuator nr. 4 with 200.8 g hung

(d) Actuator nr. 5 with 251.1 g hung (e) Actuator nr. 5 with 330.7 g hung (f) Actuator nr. 5 with 412.9 g hung

(g) Actuator nr. 6 with 456.5 hung (h) Actuator nr. 6 with 599.0 g hung (i) Actuator nr. 6 with 754.6 g hung

Figure D.4: Elasticity tests: raw displacement data, obtained for varying weights over different 2 ply actuators, supplying a constant voltage.

D.2 Absolute thermal conductivity (λ) computation results

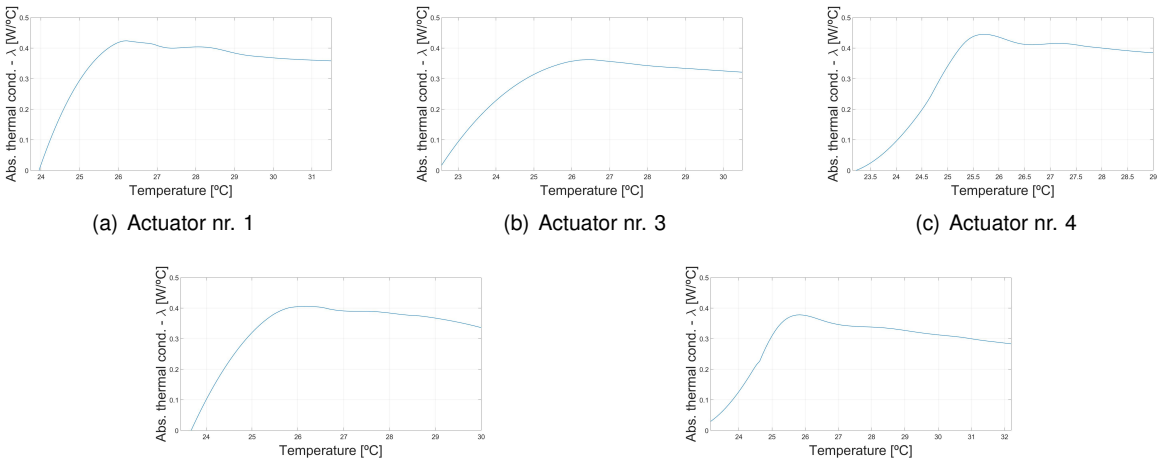

(a) Actuator nr. 1 (b) Actuator nr. 3 (c) Actuator nr. 4

(d) Actuator nr. 5 (e) Actuator nr. 6

Figure D.5: Parameters estimation: absolute thermal conductivity (λ) computed from each actuator's data-set.

D.3 Thermal mass (C_{th}) computation results

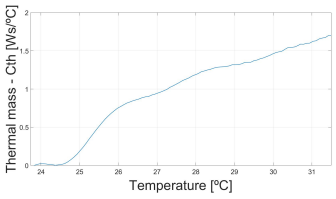

(a) Actuator nr. 1

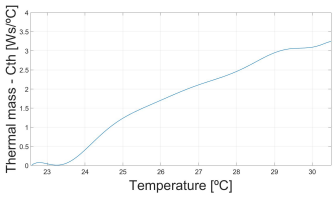

(b) Actuator nr. 3

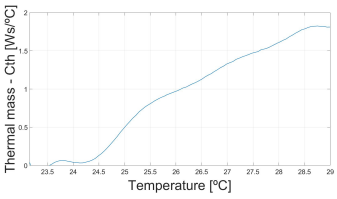

(c) Actuator nr. 4

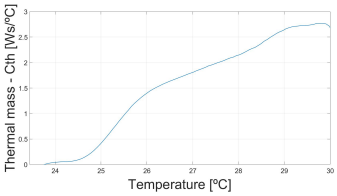

(d) Actuator nr. 5

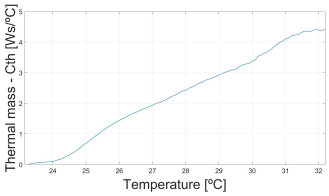

(e) Actuator nr. 6

Figure D.6: Parameters estimation: thermal mass (C_{th}) computed from each actuator's data-set.

D.4 Stiffness (k) computation

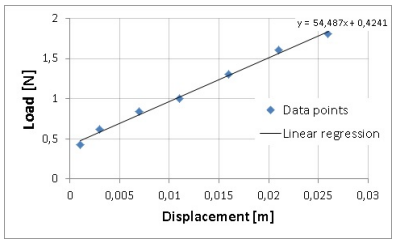

(a) Actuator nr. 1

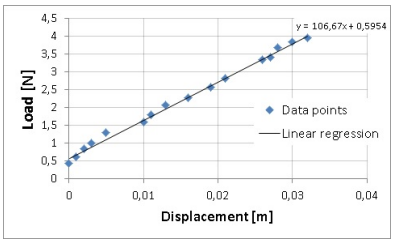

(b) Actuator nr. 3

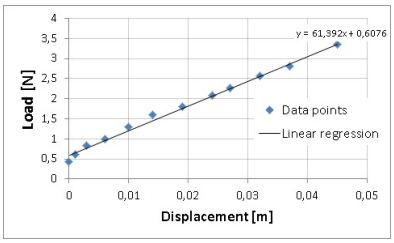

(c) Actuator nr. 4

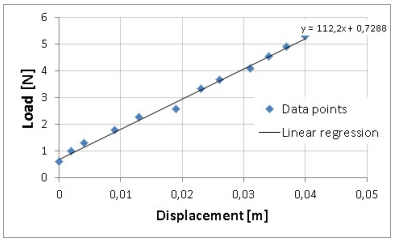

(d) Actuator nr. 5

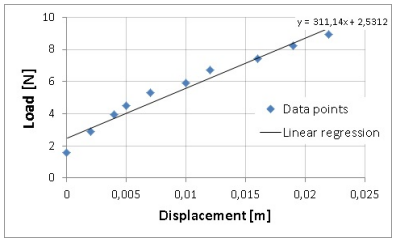

(e) Actuator nr. 6

Figure D.7: Parameters estimation: data acquired to compute each actuator's stiffness (k).

D.5 Demonstrative videos

SCP actuators' working process: Link 1;

SCP actuators' manufacturing process: Link 2; **AAA's working process:** Link 3;

AAA's angle variation with 2 SCP actuators (Table 4.9): Link 4;

AAA's angle variation with a spring and 1 SCP actuator (Table 4.11): Link 5;

AAA's angle variation with a rubber band and 1 SCP actuator (Table 4.12): Link 6;

Real system's results for a sine wave (from 4.4.4): Link 7.

D.6 Angle tracking performance for a smaller radius (r_p)

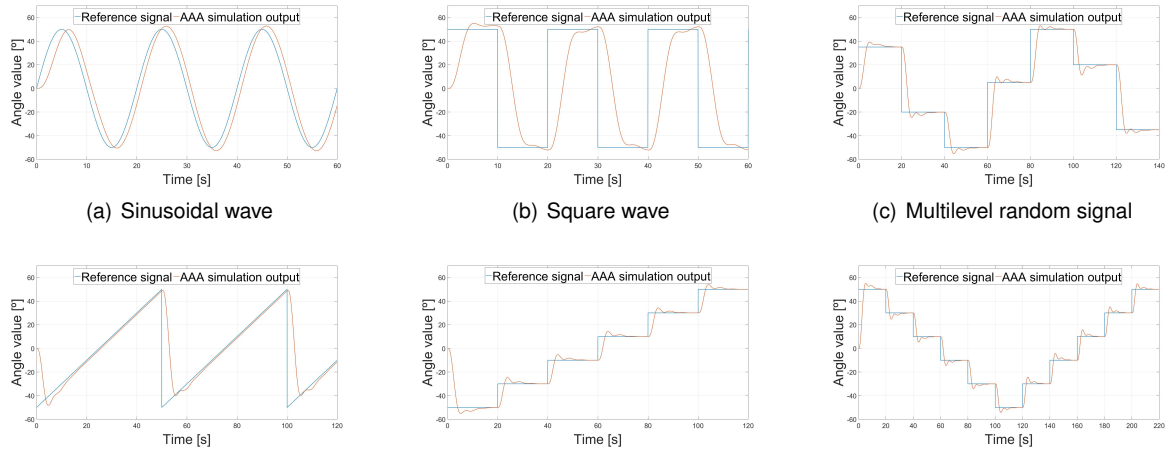

(a) Sinusoidal wave (b) Square wave (c) Multilevel random signal

(d) Sawtooth (e) Stair-shaped (f) Triangle-shaped

Figure D.8: Verification simulations: angle tracking results for different references with a new radius.

D.7 Future work

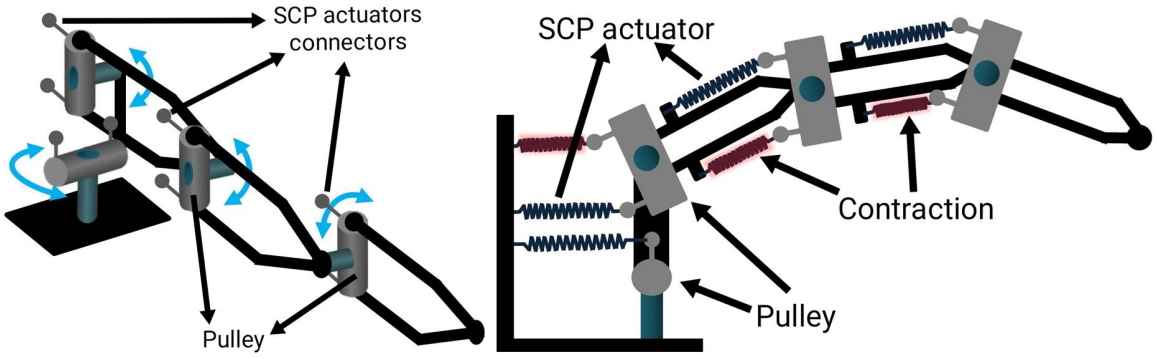

(a) Human finger-type structure. Perspective view and side view.

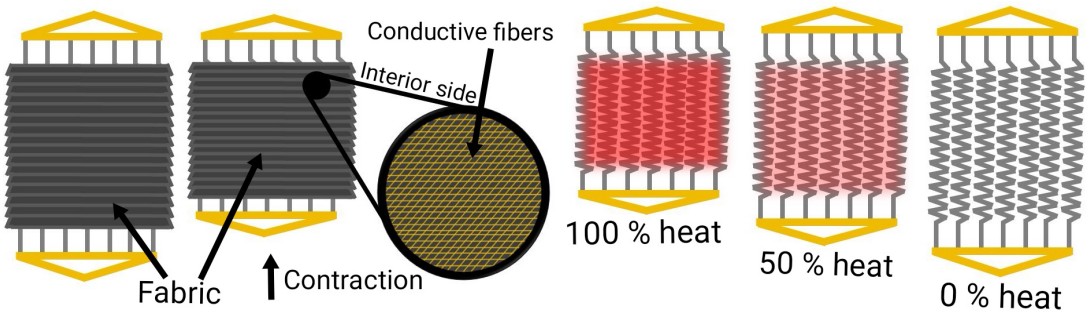

(b) Array of SCP actuators. Interior and exterior view while contracting.

Figure D.9: Future work: new solutions to explore.